ROMA TRE
UNIVERSITÀ DEGLI STUDI

Dipartimento di Fisica
"Edoardo Amaldi"

Università degli Studi Roma TRE

Scuola Dottorale in Scienze Matematiche e Fisiche - Sezione di Fisica
XXII ciclo

Pressure-induced metallization process in Strongly Correlated Electron Systems.

Relatore interno
prof. Giovanni Stefani

Coordinatore
prof. Guido Altarelli

Relatore esterno
prof. Paolo Postorino

Dr. Carlo Marini

A. A.
2009-2010

Contents

Introduction

Understanding the physics of strongly correlated systems is one of the most challenging tasks of condensed matter research. Transition metal and transition metal compounds typically show a large variety of phases different for transport, structural, and magnetic properties on varying internal (e.g. chemical composition, doping ...) and external (e.g. temperature, pressure, electric or magnetic field, ...) parameters. Such a rich phenomenology is the result of a complex and often delicate balance among several different microscopic interactions simultaneously at work in these systems. Very often indeed it is only through a combined theoretical-experimental investigation of the the effects of magnetic interactions, electron-electron and electron-phonon correlation that a real knowledge of the system can be achieved. These systems thus represent an intriguing scientific problem but their intrinsic sensitivity to small changes of internal/external parameters and the resulting good possibility of a focused material engineering make this class of systems highly appealing for a wide range of technological applications. The study of the microscopic mechanisms driving the system towards the different regions of the phase diagram and the close analysis of the physics underlaying the phase boundary crossover is the main route to develop reliable models to reproduce or possibly to predict the physical behavior of these strongly electron correlated systems.

Among all the possible phase transitions, the metal insulator transition (MIT) in these systems is a particularly interesting phenomenon to which the lattice, the electronic, and the spin degrees of freedom of the system often contribute in conjuction. The extent of charge localization/delocalization can be directly affected by charge-lattice coupling triggered by local lattice distortions activated via spontaneous symmetry breaking (e.g. Peierls and Jahn-Teller effect) or structural transition which profoundly modify the band structure. On the other side the MIT can originate from pure electronic mechanisms such as electron-electron correlation (e.g. Mott-Hubbard transition) or charge tranfer phenomena. The physical scenario underlying the MIT can be made further complicated when more then one of the above

mentioned microscopic mechanisms can cooperate in modifying the electronic state of the system.

In recent years high pressure demonstrated to be a useful technique for investigating the physics of strongly correlated electron systems. Applying high pressure can be a suitable tool for studying the role of lattice and electronic degree of freedom in driving the MIT and in disentangling the effects of the different interactions on the macroscopic properties. Indeed, in some cases, structural symmetrization can be forced by pressure and local lattice distortion can be reduced or definitely removed. However, even in the case in which applying pressure does not succeed in modifying lattice distortion or symmetry, it can provides useful information. A simple isotropic lattice compression indeed has the effect of increasing the orbital overlap and allows, in principle, to disentangle pure electronic effects from those lattice-mediated. Finally, as observed in the case of some manganite families, reducing the volume can have the effect of enhancing hidden magnetic interactions too weak to be detected at ambient pressure condition.

The present work focuses on three systems where different mechanisms are expected to give rise pressure-induced MITs: the Peierls distorted solid Tellurium, the Mott-Hubbard pyrite $NiS_{2-x}Se_x$, and the $V_{1-x}Cr_xO_2$ where both Peierls lattice distortion and electron correlation are expected to contribute to the spectacular temperure driven MIT (five order of magnitude jump in the conductivity). All the systems have been investigated by means of Raman and Infrared spectroscopy fully exploiting the simplicity and the versatility of diamond anvil cells (DAC) to pressurize the samples. As to the the Infrared measurements we take full advantage of the state-of-the-art performances of the Infrared beamline SISSI at the Synchrotron Elettra (Trieste). The very small sample dimensions in the DAC (typically 100x100x10 μm) require indeed a source with the very high brilliance of a synchrotron infrared source. An about equal effort has been devoted in investigating the three systems.

We have at first investigated the MIT in Peierls distorted systems. Representative of this class of systems is solid Te, an elemental system which shows a complex sequence of high pressure structural and electronic phases, which, as well as for the other elements of the VI group, are still object of debate. At ambient conditions, solid Te has a trigonal structure with helical chains running parallel to the c axes. The unit cell contains three atoms, each having two nearest neighbors within chain with covalent-like bonds, and four second neighbors on the adjacent chains linked by means of Van der Waals interaction. This chain framework may be considered as arising from a Peierls distortion of the six-coordinated simple cubic structure. On increasing the pressure a reduction of the inter-chains distances occurs lead-

ing to a structure symmetrization, accompanied by a charge delocalization process which sets in at 4 GPa.

High pressure Raman and Infrared measurements (0-15 GPa) have been carried out to probe lattice and electron dynamics properties of solid Te around the MIT and in the high pressure metallic phase. From the analysis of the pressure dependence of the Raman-active phonon modes we have found evidences of the structural transition at $\sim$ 4 GPa and, on further increasing the pressure, the existence of an incommensurate phase at $\sim$ 8 GPa recently proposed in the literature. Moreover a careful study of the pressure dependence of the measured phonon peak intensities allowed us to suggest the possibility that an inter-chain charge transfer process may be responsible of the MIT through the removal of the chain distortion. Ab initio Density Functional Theory (DFT) calculation, carried out on trigonal Te and in full agreement with the experimental observations, confirm the above hypothesis of pressure induced inter-chain charge transfer by the observation of a sensible reduction of the electron density among the nearest neighbouring Te atoms in-chain in favor of an increase of the electron density toward the second neighbouring Te atom in the adjacent chain. Finally high pressure Infrared measurements, quite recently carried out, give direct evidence of a pronounced dichroism of the system showing different values of the band edge, depending on the polarisation of the incident beam. In this case, on applying pressure, the MIT has been directly observed through the pressure induced band gap closure. It is worth to notice that on approaching the transition at 4 GPa a progressive reduction of band edge anisotropy has been observed in agreement with the idea of pressure induced symmetrization.

The second system investigated has been the Nickel pyrite. Cubic pyrite NiS_2 is a charge transfer insulator and has attracted interest as it easily forms a solid solution with $NiSe_2$ ($NiS_{2-x}Se_x$), which, while being iso-electronic and iso-structural to NiS_2, is nevertheless a good metal. The $NiS_{2-x}Se_x$ pyrite is considered together with vanadium sesquioxide V_2O_3, a text-book example of strong correlated electron systems. Since the Se^{2-} p orbitals have larger spatial extension with respect to the S^{2-} ones, the substitution of S with Se in $NiS_{2-x}Se_x$ drives the system at room temperature to a bandwidth-controlled MIT for $x \approx 0.6$. An alternative way to induce a metallic state in NiS_2 is applying a hydrostatic pressure. Following Mott's original idea, this technically challenging procedure offers the unique opportunity to continuously tune the bandwidth, without introducing impurities or disorder.

We have carried out both Infrared and Raman measurements as a function of x (0-1.2) and pressure (0-12 GPa) on several samples of the $NiS_{2-x}Se_x$ pyrite family. Bearing in mind that the lattice volume is expanded by Se-substitution and compressed by pressure an extended volume dependence

of the optical properties can be obtained by combining the two series of measurements. The comparative analysis of the volume dependence of the spectral weight (Infrared) and of the phonon frequencies (Raman) allowed us to demonstrates that the two metallic state obtained on applying pressure and on increasing the Se alloying have different origin as also supported by electronic band structure calculations. On applying external pressure on NiS_2, the closure of the charge transfer gap is responsible for the insulator to metal transition; in contrast upon Se alloying, the increase of electronic bandwidth drives the system towards the metallic state.

The last system investigated is the $V_{1-x}Cr_xO_2$ where the spectacular and abtrupt temperature driven MIT in VO_2 has attracted a considerable interest in the last decades. On decreasing the temperature, VO_2 shows a MIT accompanied by a simultaneous rutile (R) to monoclinic (M1) structural transition thus masking the real electronic or structural nature of the MIT. The low temperature M1 phase is a distorted R structure characterized by the formation of V-V pairs. On doping this system with small amounts of Cr, two additional monoclinic structures can be stabilized (M2 and M3), characterized by different distortion patterns of the V-V chains. Due to the V-V dimerization, the MIT in VO_2 has been originally ascribed to a Peierls instability, even if several experimental evidences pointed out the important role of the electronic correlation. Up to the present, the debate on whether VO_2 is a Peierls or a Mott insulator is still open.

Raman and Infrared spectroscopy together with preliminary X-ray diffraction high pressure measurements have been carried out on $Cr_xV_{1-x}O_2$. The result which emerge more consistently is the onset of a novel phase in the high pressure regime ($P > 10$ GPa) for vanadium dioxide: differently from ambient pressure, where the metallic phase is found only in conjunction with the rutile symmetry, at high pressure the conductive and the structural transition are decoupled and a metallic phase can be achieved within the monoclinic framework. This is an important finding which opens new experimental quests and represent a severe benchmark for theoretical models aimed at addressing the role of electron-electron correlations and lattice structure in driving the system toward the metallic phase.

The results of the present work have been the subject of the following publications:

1. *Evidence of a pressure-induced metallization process in monoclinic VO_2*
   E. Arcangeletti, L. Baldassarre, D. Di Castro, S. Lupi, L. Malavasi, C. Marini, A. Perucchi, P.Postorino,
   Phys. Rev. Lett. **98**, 196406 (2007).

2. *Optical properties of $V_{1-x}Cr_xO_2$ compounds under high pressure*

C. Marini, E. Arcangeletti, L. Baldassarre, D. Di Castro, S. Lupi, L. Malavasi, A. Perucchi, P.Postorino,
Phys. Rev. B **77**, 235111 (2008).

3. *Evidence for a monoclinic metallic phase in high-pressure VO_2*
C. Marini, L. Baldassarre, M. Baldini A. Perucchi, D. Di Castro, L. Malavasi, S Lupi, and P. Postorino
submitted to *High Pres. Res.* (2009).

4. *Pressure vs. alloying controlled metal to insulator transition in $NiS_{2-x}Se_x$ studied by infrared spectroscopy*
A. Perucchi, C. Marini, M. Valentini, P. Postorino, R. Sopracase, P. Dore, G. Sangiovanni, A. Toschi, K. Held, D. Topwal, D.D. Sarma, and S. Lupi,
Phys. Rev. B **80**, 073101 (2009).

5. *High pressure Raman scattering on Tellurium*
C. Marini, D. Chermisi, M. Lavagnini, D. Di Castro, S. Scandolo, L. Degiorgi and P. Postorino
to be submitted to *Phys. Rev. Lett.* (2009).

In the framework a more extensive study focused on the role of electron phonon coupling in leading the physical properties of strongly correlated electron systems, also SmFeAsO, which is the parent compound of one of the new Fe-As based superconductor family, has been object of spectroscopic investigations. The result of this works has been subject of the following publication:

6. *The optical phonon spectrum of SmFeAsO*
C. Marini, C. Mirri, P. Dore, S. Lupi, D. Di Castro, R. Sopracase, P. Postorino, P. Calvani, A. Perucchi, S. Massidda, G. Profeta, M. Tropeano, M. Putti, A. Martinelli, A. Palenzona
Europhys. Lett. **84**, 67013 (2008).

An Infrared study of the superconducting properties of V_3Si has been carried out and reported in the following paper:

7. *Multi-band conductivity and multi-gap superconductivity in V_3Si from optical measurements on films at terahertz frequencies*
A. Perucchi, D. Nicoletti, M. Ortolani, C. Marini, S. Lupi, U. Schade, M. Putti, I. Pallecchi, C. Tarantini, M. Ferretti, C. Ferdeghini, M. Monni, F. Bernardini, S. Massidda, and P. Dore
submitted to *Phys. Rev. Lett.* (2009)

Moreover, an optical study of low dimensional charge density waves tritellurides have been object of the following paper:

8. *Pressure dependence of the single particle excitation in the charge-density-wave $CeTe_3$ system*
   M. Lavagnini, A. Sacchetti, C. Marini, M. Valentini, A. Perucchi, P. Postorino, S. Lupi, K.Y. Shin, N. Ru, I.R. Fisher, and L. Degiorgi,
   Physics Review B, **79**, 075117 (2009).

Finally a Raman investigates of effects of accelerated carbonation on the characteristics of bottom ash from Refuse Derived Fuel (RDF) incineration has been object of the following paper:

9. *Accelerated carbonation of RDF incineration bottom ash: Co_2 storage potential and environmental behaviour*
   R. Baciocchi, G. Costa, C. Marini, A. Polettini, R. Pomi, P. Postorino, S. Rocca
   accepted for pubblication on *Waste Managment*(2009).

This Ph.D. thesis is organized in the following structure:

Physical background and state of the art

- In Chapter 1, the theoretical concepts necessary to describe the various phenomena occurring in the examined compounds are discussed. A short introduction to 3d metal compound and metal insulator transitions is given, focusing attention to Mott-Hubbard and Peierls instability transition mechanisms as responsible for the charge delocalization process occurring in these systems.

- In Chapter 2, the state of the art of solid Te, Ni pyrites, and pure and Cr-doped Vanadium dioxides is presented. In particular the structural and electronic phase diagram of the three systems will be described and the theoretical models developed for the description of the physical properties of these materials will be reviewed. The effects of external and/or chemical pressure on the physical properties of these systems will be discussed.

Results of the present work

- In Chapter 3, the experimental techniques employed throughout the measurements performed in this Ph.D. thesis are described.

- In Chapter 4, the most relevant Raman and infrared measurements on solid Te existing in the literature are presented, focusing attention on high pressure data. High-pressure Raman and Infrared measurements performed on Te samples are then reported.

- In Chapter 5, a brief review of Raman and infrared data on Nickel pyrites is first presented, focusing attention on high pressure data. High-pressure Raman and Infrared measurements performed on $NiS_{2-x}Se_x$ samples are then reported, compared and discussed.

- In Chapter 6, literature Raman and infrared studies on VO_2 will be presented, focusing the attention on high-pressure measurements. High-pressure Raman and Infrared measurements on pure and Cr-doped VO_2 samples are discussed and compared.

- In last Chapter, conclusion and comparison of the high pressure Raman and Infrared measurements on the three systems will be presented.

Chapter 1

Basic properties of transition metal compounds

In this chapter a brief overview of the main physical properties of transition metal compounds will be presented, focusing the attention on electronic band and crystal lattice structures. In the following section, the band structure and the transport properties of solid systems will be sketched. Particular attention will be devoted to the Mott-Hubbard transition mechanism and to the Peierls instability.

1.1 Electron band structure and transport properties

In solid state physics the electrical conductivity of a material is based on the transport of electrons. From the quantum mechanical point of view, electrons in crystalline materials are arranged in states which are quite closely spaced in energy, forming an almost continuous distribution of energies, called energy band. An intuitive explanation is that as atoms are brought together, the bands begin to emerge from the starting atomic states, the lower-energy states are occupied, lowering the energy and further pulling the system together. Energy bands may be often separated by regions in energy for which no wavelike electron orbitals exist. Such forbidden regions are called energy gaps, or band gaps, and result from the interaction of the conduction electron waves with the ion cores of the crystal. In this band picture, the insulator and metallic states of a systems can be understood in term of the filling of the electron bands: the systems behaves as an insulator if the energy bands are either filled or empty, which means that no electrons can move in an electric field, or as a metal if one or more bands are partly filled. In other words,

the Fermi level, which is highest occupied electron state at T = 0 K, lies in a band gap in insulators while the level is inside a band for metals. Metals are characterized by a low resistivity of order of $10^{-2} \div 10^{-6}\Omega$cm at room temperature, i.e. high charge mobility, and a linear increase in resistivity as the temperature is raised. On the other hand, insulators have resistivity of order $10^{3} \div 10^{17}\Omega$cm at room temperature, i.e. low charge mobility, and the resistivity decreases exponentially with increasing temperature.

The distinction between metals and insulator strictly yields only at absolute zero. At finite temperature the distinction becomes more qualitative and the family of semiconductor materials with bands slightly filled, may be introduced. Semiconductors are generally classified by their electrical resistivity at room temperature, with values in the range of 10^{-2} to 10^{9} Ωcm, and strongly depend on temperature.

Electrons in a solid are mainly influenced by two different causes: the ions potential and the electron-electron interaction. Thereby the electronic band structure of a given system is determined by the strength and the extent of coupling of these interactions. On this basis a preliminary analysis can be done and two main categories of insulators can be indicated.

The first category we find are band, Peierls and Anderson insulators, which can be described in terms of single electrons that interact with the crystal electrostatic field. While in a band insulator, a vanishing electrical conductivity is achieved by electron interaction with the periodical potential of ions, in a Peierls insulator a static lattice deformation occurs leading to the charge localization.

Mott and Charge Transfer insulators constitute the second category, where the insulating behavior arises as a cooperative many electrons phenomenon. In a Mott insulator the on-site Coulomb repulsion is larger than the band width, leading to the conduction band splitting into a lower and an upper Hubbard bands and providing lowest energy electron excitations scale.

Transition metals and transition metal compounds are ideal subjects for an investigation of insulating and metallic state because of the wide diversity of electrical properties observed in apparently similar materials (see the next paragraph). Having an energy similar to that of the s states, but with two units of angular momentum, 3d electron states are much more strongly localized near the nuclei and much more weakly coupled to states on the neighbouring atoms forming much narrower energy bands. Moreover the extent of Coulomb repulsion between d electrons is quite large with respect to the electron-electron interaction of s or p electrons. These findings determine quite anomalous transport properties. Many transition-metal systems with a partially filled d electron band, which are reported to be metals according to band picture scenario, behaves nonetheless as poor conductors and indeed

often as insulators at room temperature. Moreover on varying an external parameter (such as temperature, pressure, electric or magnetic field), a metal to insulator transition may occur.

Strong experimental and theoretical efforts have been devoted to the systematic exploration of this class of systems, often aimed at understanding how a metal could become an insulator as controllable parameters were changed. Different models of MIT have been proposed.

The simplest mechanism for the MIT is ordinary band overlap, without accompanying crystalline symmetry changes. Following the Mott's original idea [1], a MIT of this kind will occurs when one of these parameter changes in such a way that two bands cease to overlap, leading to a full valence and an empty conduction bands with an energy gap between them.

A MIT may be also triggered by a lattice distortion, which can lower the total energy of the system mainly in two ways: leading to an increase in the number of atoms per unit cell which introduces an extra energy gap at the surfaces of reduced Brillouin zone (as discussed below) or leading to a simple reduction of lattice symmetry, as, for example, the cubic-tetragonal distortion, which can result in additional splitting due to higher-order terms in crystalline field [2].

Analogous to the symmetry change induced MIT, long range magnetic order can produce the same effects by doubling the number of atoms for magnetic cell, introducing a band splitting due to the formation of antiferromagnetic sublattice [3].

All previous models can be purely treated within the band approximation. However fluctuations of spin, charge, and orbital correlations are usually strong in 3d electron systems and sometimes critically enhanced toward the MIT.

As first discussed by Mott and Hubbard (see 1.3 section), an electronic transition may results from the competition between the electrons kinetic energy or band term and the interaction term. The relative strength of the two terms is parameterized by the transfer integral t and by the local Coulomb repulsion U, respectively. While the kinetic part promotes the mobility of electrons, the interaction energy is minimized by suppressing charge fluctuations involving a double occupancy of sites. Hubbard obtained quantitative results only for the case of an s band, due to the immense complexity involved in applying this model to a d band. However from this simple model it can be already concluded that a critical ratio U/t exists, where the system undergoes a transition from metallic to insulating behavior. Since the gap decreases slowly to zero, conductivity will increase only gradually as the critical ratio is passed, unless a first order transition occurs. The complete neglect of all interatomic Coulomb terms in Hubbard's model eliminate the screening

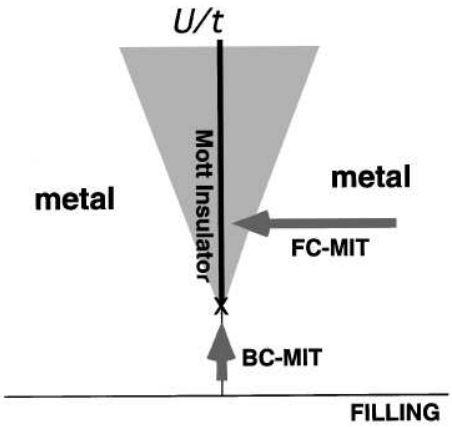

FIGURE 1.1: Metal-insulator phase diagram based on the Hubbard model in the plane of U/t and filling n. The shaded area is in principle metallic but under the strong influence of the MIT, in which carriers are easily localized by extrinsic forces such as randomness and electron-lattice coupling. [4]

effects invoked by Mott in making a sharp transition plausible. Since there is not a particular reason why such a large number of 3d crystalline systems should happen to be Mott insulator with a lattice constant very close the critical value, the Mott-Hubbard mechanism should be more effective on applying external pressure, rather than on raising the temperature.

In the Mott-Hubbard scheme, a MIT can be achieved upon modifying the key parameters (U and t) previously defined, or acting on the filling level n of the band [4]. A simple but helpful sketch of the two possible ways of inducing MIT is shown in figure 1.1. In the case of non-degenerate band, the n = 0 and n = 2 filling levels correspond to a band insulator. At half filling (n = 1, central thick line in the sketch of figure 1.1) the transition is obtained at some critical value of U/t. Therefore we will refer to this transition as a bandwidth-control MIT (BC-MIT). On the other hand, a non integer value of n leads to a metallic state. Therefore a continuous filling-control MIT (FC MIT) can be performed upon doping a Mott insulator parent compound. Usually in a doped system metallic behavior is achieved; however at some fractional, but commensurate, doping levels (such as n = 1/2, 1/3, 1/4), the compound may undergo a charge-ordering phase transition, that may lead also to an insulating state. At small doping levels (represented in figure 1.1 by the grey shaded area), due to the proximity to the Mott insulator, the carriers may easily localize due to extrinsic forces as electron-lattice interaction.

1.2 The Zaanen Sawatzky Allen scheme

A common characteristic of many strongly electron-correlated compounds is the essential contribution of 3d orbitals to the electronic properties. Let us consider the atomic wave functions of the 3d shell in a 3d transition metal atom. Since there are no atomic wave functions with the same angular momentum quantum number (l), the 3d wave functions are orthogonal to all those with lower principal quantum number (i.e. n = 1,2), just because of their angular dependence, and the radial part needs not have nodes or extend far away from the nucleus. As a result, the 3d-orbital wave functions are confined more closely to the nucleus than for s or p states of comparable energy. As a consequence, the degree of overlap between orbitals on neighbouring atomic sites is comparable with the screened Coulomb repulsion U between electrons sitting in the most localized orbitals. Oversimplified as it may be, this qualitative argument suggests in this class of materials a competition between localized electrons and itinerant electron aspects, which make these systems promising materials for technological applications.

In 1985 J. Zaanen et al. developed a model which separates correlated systems into two main classes of materials [5] : Mott-Hubbard and charge transfer insulator. The Mott-Hubbard theory [6] is based upon the assumption that d-d like Coulomb exchange interactions (U) are strongly suppressed because of the high energies involved ($5 - 10$ eV). This model implies that the band gap of transition metal compounds is a d-d gap. This is correct for light transition metal compounds like Ti or V based oxides, whereas for late transition metal oxides like NiO the band gap has been found to be directly related to the electronegativity of the oxygen ligand [7]. In particular the latter show a charge fluctuation which does not involve U but is very relevant in the understanding of the properties of these materials, namely the charge transfer Δ. The charge transfer can be explained as a transfer of a ligand electron into the metal d band. By considering both, U and Δ for transition metal compounds, within the scheme of the Anderson impurity model [8], it is possible to describe the dependence of the band gap on U and Δ qualitatively [5].

A given transition metal compound can be associated with a particular class of material, showing properties closely related to the values of U and Δ, respectively:

- *Mott-Hubbard insulators*: The band gap E_{gap} is proportional to U. That is the case if $U << \Delta$. The lowest energy excitations are obtained by transferring one electron from one transition metal ion to another one. Examples are light transition metal oxides like TiO_2 , V_2O_3 and related

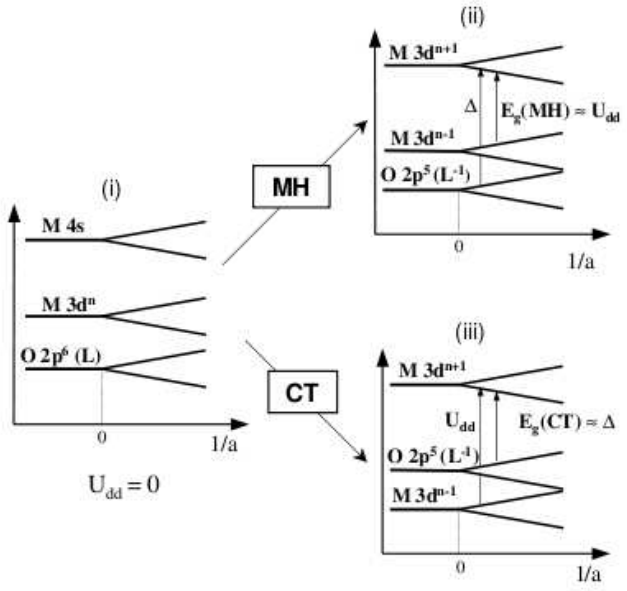

FIGURE 1.2: One electron (i), Mott Hubbard (ii) and charge transfer (iii) diagrams of a transition metal compound.

compounds.

- *Charge transfer insulators*: E_{gap} is proportional to Δ. That is the case if $\Delta >> U$. The lowest energy excitations are obtained by transferring one electron from the ligand atom to the transition metal ion. Examples are late transition metal oxides like CuO and related compounds.

Further classifications are the following:

- *Intermediate compounds*: If $\Delta \sim U$ the Coulomb potential U and the charge transfer Δ have significant influence to the properties of the compound. A fine balanced competition between Coulomb and charge transfer interactions takes place.

- *d band metals*: Both holes and electrons are heavy. Examples are the high temperature phases of V_2O_3, Ti_2O_3, TiO and CrO_2.

- *"p"-type metals*: Holes in the anion valence band (ligh holes). Examples are CuS e CuSe and NiSe. The pyrites (NiS_2, etc.) would belong to this class but holes in the anion valence bands are accommodated in antibonding orbitals of sulfur pairs, forming a band gap.

1.3 Electron correlation and lattice distortion in transition metal compounds

In strong correlated systems the electronic Coulomb repulsion and lattice degrees of freedom (and their interplays) have typically a key role in determining the physical properties. The main effects of electron-electron correlation are summarized in the following. First of all, the electronic repulsion leads to a strong Hund's rule regulating the electronic orbitals filling which is at the basis of magnetism in many systems. Moreover the electronic Coulomb repulsion promotes electronic localization in spite of extended state, strongly inhibiting the charge transport and, in some cases, leading to an insulating state in system otherwise expected to show metallic behaviour [4]. Electron correlation strength can be controlled by modifying the lattice parameters and/or chemical composition within the same symmetry lattice. Coulomb interaction is kept almost unchanged and hence control of electron correlation strength is usually achieved by control of the transfer interaction or the one-electron bandwidth. This is the case of insulating NiS_2, which forms a solid solution with $NiSe_2$ which, while being iso-electronic and iso-structural to NiS_2, is a good metal. As a consequence of Se alloying, $NiS_{2-x}Se_x$ undergoes to a metal-insulator transition on increasing Se content.

Another possibility is that the metal to insulator transition can involve a structural transition which reduces the lattice symmetry on entering the insulating phase [9,10]. In these cases the lattice instabilities have to balance with other active different interactions between the electronic, lattice, and spin degrees of freedom. These interactions could promote or prevent the occurrence of a lattice distortion, as it occurs in solid Te. Even if the Coulomb repulsion is not actually so strong to open a gap at the Fermi level and leading to an insulating state, correlation effects could help to open up a real gap in the low temperature phase of crystals undergoing localized or extended lattice distortions, thus leading to a Mott-assisted structural transition. The latter scenario has been recently invoked as possible explanation of the metal-insulator transition occurring in VO_2 on varying the temperature.

In the following paragraphs Mott-Hubbard model and Peierls instability will be presented and discussed as possible theoretical frameworks for investigating the MIT in the three systems (Te, $NiS_{2-x}Se_x$, $V_{1-x}Cr_xO_2$) treated in this thesis work.

1.4 Hubbard model

Introduced in 1963, the Hubbard model [6] is the prototype model to describe strongly correlated electron systems. This lattice model, which considers only electrons in a single band, adds to a tight-binding Hamiltonian a repulsive term between electrons at the same lattice site i:

$$H = t \sum_{<ij>\sigma} (c^{\dagger}_{i\sigma} c_{j\sigma} + h.c.) + U \sum_{i} n_{i\uparrow} n_{i\downarrow} \tag{1.1}$$

where the creation (annihilation) operator of the single-band electron at site i with spin state σ is denoted by $c^{\dagger}_{i\sigma}$ ($c_{i\sigma}$) and $n_{i\sigma} = c^{\dagger}_{i\sigma} c_{i\sigma}$ is the number operator. The hopping integral t within a tight-binding model is supposed, for sake of clarity, isotropic and non-vanishing only for nearest-neighbor hopping:

$$t_{ij} = \int \phi^{*}_{i\sigma}(r) \frac{\hbar^2 \Delta^2}{2m} \phi_{j\sigma}(r) dr \tag{1.2}$$

Here m is the electron mass and $\phi_{j\sigma}(r)$ is the Wannier orbital. The repulsive Coulomb interaction felt by two electrons at the same atomic site is represented by U > 0:

$$U = \int \phi^{*}_{i\sigma}(r) \phi_{i\sigma}(r) \frac{e^2}{|rr|} \phi_{i-\sigma}(r') \phi^{*}_{i-\sigma}(r') dr dr' \tag{1.3}$$

This model is obviously oversimplified: it does not take into account any multi-band effect and, strictly speaking, is valid only for s-orbitals. When dealing with d-orbitals it is implicitly assumed that orbital degeneracy is lifted due to the crystal field, in order to describe the low-energy excitations in terms of a single band lying at the Fermi level. A further hypothesis is that either the ligand-band (p) energy is far from the relevant d-band or it is so strongly hybridized that a single band can be considered. The Hamiltonian in eq. 1.1 also neglects the inter-site Coulomb repulsion and often the electron hopping is restricted to the sum over pairs of nearest-neighbor sites $< ij >$. This can be justified by the screening effect that makes the long-range part of the Coulomb force to decrease exponentially with r. These assumptions makes the model unable to describe important features such as charge ordering or magnetic effects that can arise from geometrical frustration. In spite of those simplifications, the Hubbard model well captures the features of the Mott insulating phase (also with basically correct spin correlations) and the transition between Mott insulators and metals, rising up from the competition of the kinetic energy, which promotes the mobility of electrons, and the electron repulsion, which can be minimized only by suppressing double

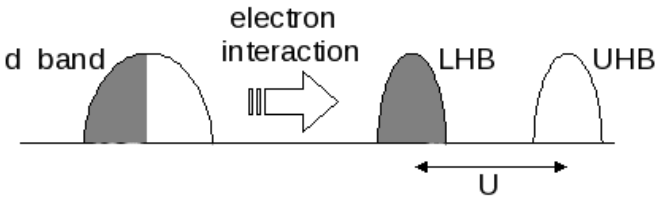

FIGURE 1.3: Splitting of the half-filled band as the on-site Coulomb repulsion U is turned on

occupancy of each sites (electron localization). The insulating state occurs at half-filling where the average electron number $< n_{i\sigma}$ is controlled at 1/2. Considering a nearest-neighbor Hubbard model on a cubic lattice, the band structure of the non-interacting part is described as:

$$H_t = \sum_{k\sigma} \epsilon_0(k) c^\dagger_{k\sigma} c_{k\sigma} \tag{1.4}$$

$$\epsilon_0(k) = 2t(cosk_x a + cosk_y a + cosk_z a) \tag{1.5}$$

where a is the lattice constant and the Fourier transform of the electron creation operator is defined as:

$$c^\dagger_{k\sigma} = \sum_j e^{ikr_j} c^\dagger_{j\sigma} \tag{1.6}$$

At half-filling, under electron-hole symmetry, the Fermi level lies at $\epsilon_F = 0$ and the appearance of the insulating phase is clearly due to the correlation effect, arising from the second term of Eq. 1.1. The resulting band splitting is sketched in figure 1.3.

The Hubbard model can be exactly solved only in one dimension (1D) [11], while for $D > 1$ only the limits $U/t \to 0$ and $U/t \to \infty$ can be analytically discussed. In the former case the bands of non-interacting system are recovered, and a metallic phase occurs. Within the limit of strong correlation (large U/t), carrier hopping is unfavorable with respect to antiparallel alignment of two neighboring spins. Hubbard model provides, therefore, an excellent description of the system in the insulating phase, as it becomes an Heisenberg model (with $J = \frac{4t^2}{U} > 0$), where in the absence of magnetic frustration due to the lattice symmetry, an antiferromagnetic phase is attained. For intermediate values of U/t, the band of the non-interacting system splits into two bands: the lower Hubbard band (LHB) and the upper Hubbard band (UHB), divided by a gap of the order of U (see figure 1.3).

Let us now focus on charge transfer insulator systems. In this case, the Hubbard model must be reformulated to take into account the effective band

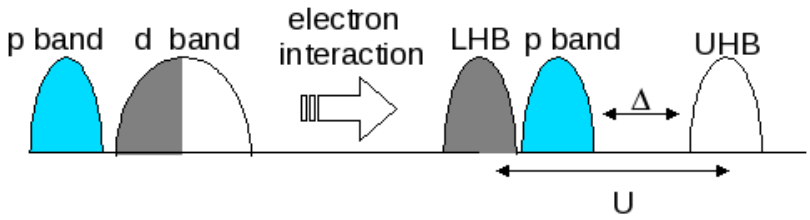

FIGURE 1.4: Schematic illustration of energy levels for a charge-transfer insulator generated by the d-d and p-d site interactions.

structure, characterized by the energy proximity between the p ligand and 3d metal transition orbitals which clearly affects charge excitations in the insulating state. Neglecting p electron Coulomb repulsion, Hubbard Hamiltonian can be rewritten into:

$$H = -\sum_{<i,j>\sigma} t(d^{\dagger}_{i,\sigma}p_{j,\sigma} + p^{\dagger}_{i,\sigma}d_{j,\sigma}) + (\epsilon_d - \mu)\sum_{i\sigma} n^d_{j,\sigma} + (\epsilon_p - \mu)\sum_{i\sigma} n^p_{i,\sigma} + U\sum_{i} n^d_{i,\uparrow}n^d_{i,\downarrow} \tag{1.7}$$

where $d^{\dagger}_{i,\sigma}$ ($p^{\dagger}_{i,\sigma}$) is the creation operator of a d (p) electron with spin σ at site i while $n^d_{i,\sigma}$ ($n^p_{i,\sigma}$) is a number operator of d (p) electrons with spin σ at site i [12]. The electron hopping is considered only between the nearest-neighbor d and p sites and electron-electron correlation, providing the excitations of the charge transfer insulator [5], as schematically illustrated in figure 1.4. The energy parameters are chosen to be $\epsilon_p < \epsilon_d < \mu < \epsilon_d + U$. A charge-transfer gap is defined as $\Delta = \epsilon_d + U - \epsilon_p$. Note that in this two-band Hubbard model at finite U, there is an extra degree of freedom as the effective bandwidth of the hybridized d band is given by $W = t^2/\Delta$ that corresponds to the virtual hopping of electrons between the nearest-neighbor d and p sites. The Hamiltonian 1.8 contains the necessary ingredients to drive the Mott mechanism, providing the metal-insulator parameter given by the ratio W/Δ. In this scenario, close to zero temperature, a sufficiently large charge-transfer gap W $<$ Δ suppresses quantum fluctuations of both charge and spin driving the system into the antiferromagnetic insulating phase. On decreasing the charge-transfer gap, the onset of the Fermi-liquid phase sets in through quantum charge fluctuations.

1.4.1 Approximate solutions of the Hubbard model

The early work of Hubbard [6] described the transition in terms close to Mott's original view. Starting from the insulating phase, upon reducing U

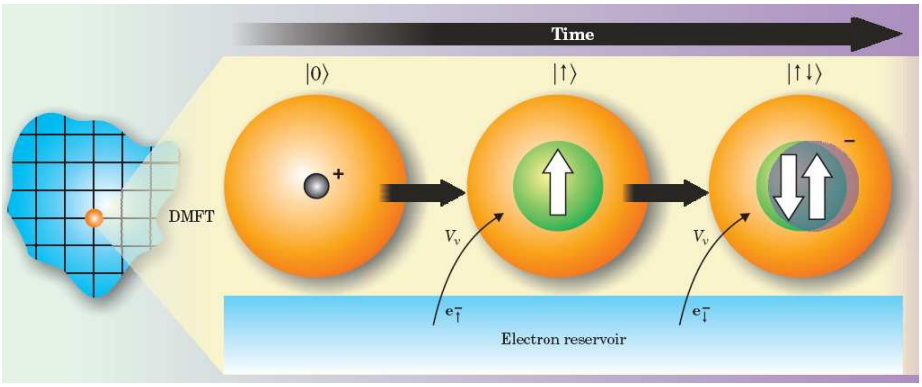

FIGURE 1.5: DMFT of correlated electron solid replace the full lattice of atoms and electrons with a single impurity atom imagined to exist in a bath of electrons [17]

there is a critical value U_C where the LHB and the UHB merge with each other and a metal is recovered. The so-called Hubbard approximations, however, fail in reproducing the discontinuous character of the MIT due to the gap closure. Moreover, also they do not provide a description of the metal consistent with the Fermi-liquid properties. Therein, no quasi-particle peak shows up as the metallic phase is established. On the other hand Brinkman and Rice [13], developing a previous work of Gutzwiller [14], started from the metallic phase, described through a strongly renormalized Fermi liquid with a reduced low-energy scale (or effective Fermi energy) of order ZD. Z is the quasiparticle residue and D is the half-bandwidth (hereafter considered as equivalent to t in the U/t ratio). As the interaction strength increases, this energy scale vanishes at a critical value U_{BR}, with $Z \propto (U_{BR} - U)$. This approach is a consistent low-energy description of the strongly correlated metal, but does not account for the high-energy excitations forming the Hubbard bands, which should be present already in the metallic state. Furthermore, it gives an oversimplified picture of the insulating state, which is described as a collection of local moments with no residual antiferromagnetic exchange. The Brinkman-Rice approach can be justified formally with the slave boson technique [15] that allows one to extract the behavior with temperature of the correlated electron system.

It is clear that classical mean field theories are not appropriate to describe simultaneously coherent low-energy excitations (as for the Gutzwiller approach) and incoherent, of high-energy (Hubbard approximations). The Dynamical Mean Field Theory (DMFT) can instead describe, within the Hubbard model, both the insulating and the metallic phase [16, 17]. In essence, DMFT reduces (or maps) a many-body lattice problem to a single-

site problem with effective parameters, in analogy to the classical theory of magnetism (where the one site spin is represented in interaction with an effective magnetic field). In the electron case, the degrees of freedom at a single site are the quantum states of the atom inside a selected central unit cell of the crystal; the rest of the crystal is described as a reservoir of noninteracting electrons that can be emitted or absorbed in the atom (see figure 1.5 [17]).

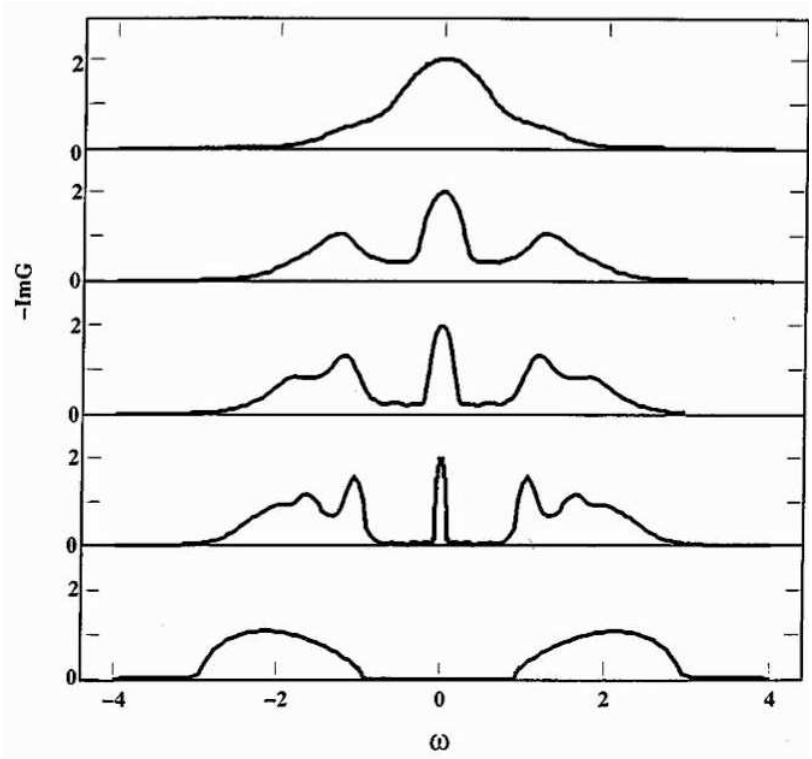

FIGURE 1.6: Evolution of the density of states at T = 0 obtained with DMFT. The first four curves (from top to bottom, U/t = 1, 2, 2.5, 3) correspond to an increasingly correlated metal, while the bottom one (U/t = 4) represents the insulating state [16]

Unlike the classical case, in which a number (the effective magnetic field)describes the effect of the medium on the central site, the quantum case requires an energy-dependent Weiss effective field to capture the ability of an electron to enter or leave an atom. At half filling, the evolution of the density of states (DOS, defined as $\pi D\rho(\omega)$= - Im[G] [16], where G is the Green function and D the half-bandwidth) is shown for T = 0 in figure 1.6, for increasing U/D ratio. Therein it is possible to follow the progressive separation of the central quasi-particle (QP) peak (that corresponds to low-energy coherent excitations) in the LHB and UHB for increasing U/t. At a critical value of

$U = U_{c1}$ the Hubbard bands separate one from the other while the QP peak is still retained at the Fermi energy $\omega = \epsilon - \epsilon_F = 0$ (see the fourth panel of figure 1.6). For higher values of U the peak increasingly narrows until it disappears for $U = U_{c2}$ and the two Hubbard bands only are left in the DOS. The vanishing of the QP peak is associated with a vanishing renormalization factor Z, and hence with a diverging value of $m^\star$ as previously described by Brinkman and Rice. The insulating phase ($U > U_{c2}$) described by DMFT is in agreement with the results of the Hubbard approximations. The fact that DMFT provides correct results for both the cases of small and high interactions (i.e. small or large values of U) and that it becomes exact in the limit of infinite dimensions, suggests that also the results at intermediate values of U/t are probably correct.

1.5 Peierls Instability

In the previous paragraph we have considered the effect of electron Coulomb repulsion setting in almost localized electronic levels. Let us now focus our attention on the effect of lattice distortion in modifying the electronic transport properties of simple systems, such as broad band metal, with an electronic band $E(k)$ not completely filled. A slight displacement of the atoms reducing the lattice symmetry gives rise to a perturbation of the periodic potential viewed by the electrons which modify the $E(k)$ dispersion, opening a band gap. This class of systems is referred as *Peierls* insulator [2].

Let us consider, for sake of simplicity, a one-dimensional half filled metal (metallic linear chain) [18]. Let be a the atom spacing parameter and β the hopping integral. Let also rescale the energy so that the on-site energy term is zero. The band structure is $E(k) = 2\beta \cos(ka)$ over the first Brillouin zone $(-\pi/a, -\pi/a)$. Suppose we now move one atom every two ones so that there are now two hopping integrals β_1 and β_2 and two atom spacings in the unit cell, as shown in figure 1.7.

The period of the chain is doubled, and therefore the Brillouin zone now extends from $-\pi/2a$ to $\pi/2a$. Let $|m,1>$ and $|m,2>$ denote the atomic states on atoms 1 and 2, in the m-th cell. The eingenstates of the chain are now expressed, using the Bloch's theorem, as follows:

$$\Psi_k^n = \sum_{m=-\infty}^{\infty} e^{ik2ma}(c_1^n(k)|m,1> + c_2^n(k)|m,2>) \tag{1.8}$$

where $c_1^n(k)e^{ik2ma}$ and $c_2^n(k)e^{ik2ma}$ are the coefficients of atomic states $|m,1>$ and $|m,2>$. Inserting this eigenstate into the Schroedinger equation $H\Psi_k^n =$

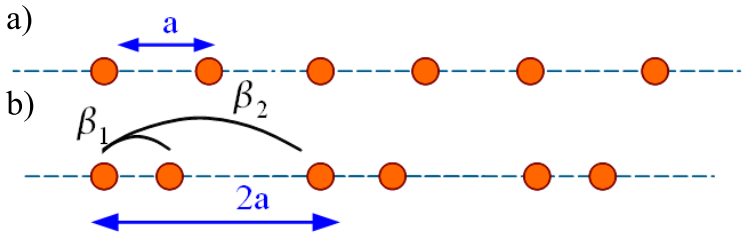

FIGURE 1.7: a) A perfect infinite chain in which all nearest neighbour bound lengths and hopping integrals are the same. b) A distorted infinite chain in which one atom every two atoms is moved to the right so that there are now two hopping integrals β_1 and β_2, and the period of the chain is doubled.

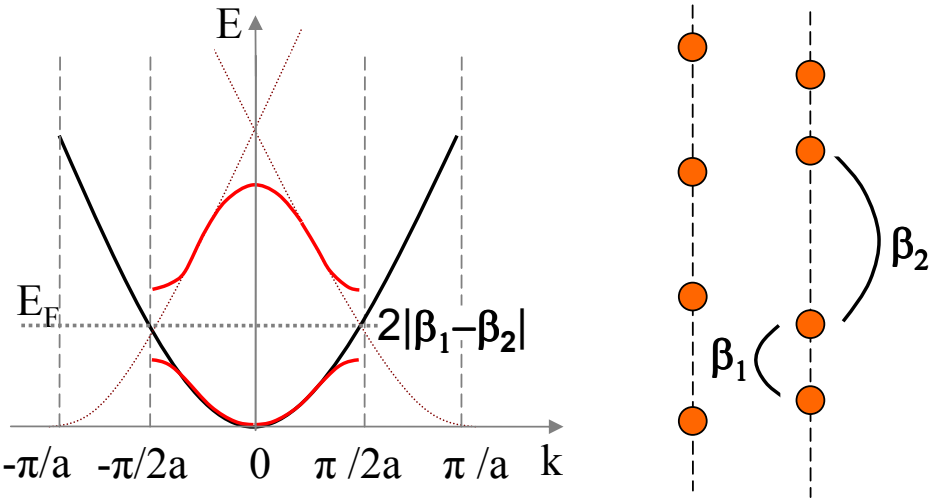

FIGURE 1.8: The energy bands for the undistorted (back curve) and distorted (red curve) infinite chain

$E_k^n \Psi_k^n$, we obtain the following secular equations:

$$\begin{aligned}(\beta_1 e^{-ik2ma} + \beta_2)c_2^n(k) &= E_k^n c_1^n(k) \\ (\beta_2 + \beta_1 e^{ik2ma})c_1^n(k) &= E_k^n c_2^n(k)\end{aligned} \tag{1.9}$$

which lead to the following energy bands

$$E_k^n = \pm\sqrt{(\beta_1 + \beta_2)^2 + 4\beta_1\beta_2 cos^2(ka)} \tag{1.10}$$

These bands are sketched in figure 1.8, and it is seen that a gap is opened up at the Brillouin zone boundaries k = $\pm\ \pi/2a$ of magnitude $2(|\beta_1 - \beta_2|)$. If there is one electron per atom the band of equispaced chain is half-filled

and Fermi wave vector is $k_f = \pm\pi/2a$. After the distortion the lower band shown in figure 1.8 is filled and the upper band is empty. This has two consequences. The first is that there is an energy gain for the system, i.e. the sum of the energies of the occupied electronic states is lower in the distorted chain because the gap depresses the energy of states near k_F. The second is that the linear chain is transformed from metal to an insulator.

Although the sum of the occupied electronic eigenvalues is lowered there is an energy cost associated with the distortion of the chain because there is now an elastic strain energy. The strain energy varies quadratically with the magnitude of the distortion of the bond lengths. On the other hand, $|\beta_1 - \beta_2|$ varies linearly in the distortion of the bond lengths, at least for small bond distortion. The energy gain of the occupied state is proportional to $|\beta_1 - \beta_2|$, at least near the Brillouin zone boundaries. Thus the electronic energy lowering is linear in the distortion of the bound lengths, and therefore there is always a net lowering in the total energy by distorting the bounds in this way for a half-filled band. Generalizing this result we see that for a Fermi wave vector, k_F, in the undistorted chain the total energy of the system can be reduced by a periodic distortion of wavelength $n\pi/k_F$, where n is an integer, due to the split into n sub-bands with gaps between them at the Brillouin zone boundaries.

In conclusion, there is always a gain in the energy if an ideal infinite linear chain of atoms undergoes a distortion with a wavelength π/k_F and the linear chain is then converted from a metal to an insulator. In three dimensions the wave vector of the periodic distortion lies at a point on the Fermi surface, and only those state near this point will be split by the distortion, with the rest of Fermi surface remaining unaffected. Whether a sufficient energy lowering can be achieved to make this distortion favorable depends on how flat the Fermi surface is near this wave vector. The original analysis of the Peierls instability of a metallic linear chain neglects temperature effects. In the next section the temperature dependence of the electronic state of a metallic system sensible to a Peierls distortion will be discussed.

1.5.1 Instability of the electron gas in presence of electron phonon coupling

The Peierls instability together with the Kohn anomaly are probably the most important phenomena predicted and only subsequently experimentally observed in the physics of low dimension conductors. As discussed above, Peierls argued that a one-dimension fermionic system living on a chain becomes unstable with respect to a lattice distortion which doubles periodicity,

creating a gap in the electron spectrum. This argument was for zero temperature and it did not take into account the cost of the lattice energy required to create the lattice distortion. Fröhlich showed that the Peierls instability persists if the (classical) lattice restoring forces are weak enough and the temperature is sufficiently low [19, 20].

Peierls instabilities, such as often spontaneous lattice symmetry breaking (e.g Jahn-Teller), can be discussed in term of a coupling between the electronic and lattice degree of freedom. In particular Peierls transition can be analysed by means of kinetic electron gas Hamiltonian plus electron-phonon coupling [21]. In the second quantization scheme, the electron gas Hamiltonian is given by:

$$H_{el} = \sum_k \varepsilon_k a_k^\dagger a_k \tag{1.11}$$

with $a_k^\dagger$ and a_k being the creation and annihilation operators for the electron states with energy $\varepsilon_k = (\hbar k)^2/2m$, while lattice vibrations are described by:

$$H_{ph} = \sum_q \hbar\omega_q (b_q^\dagger b_q + \frac{1}{2}) \tag{1.12}$$

with $b_q^\dagger$ and b_q being the creation and annihilation operators for phonons of wave-vector q, and ω_q being the normal mode frequencies. Let us introduce the electron-phonon coupling by means of the so-called Fröhlich term [19]:

$$H_{el-ph} = \sum_{kq} g_q (b_{-q}^\dagger b_q) a_{k+q}^\dagger a_k \tag{1.13}$$

where g_q is the coupling constant. The overall Hamiltonian:

$$H = H_{el} + H_{ph} + H_{el-ph} \tag{1.14}$$

describes a coupled fermion-boson system.

Since $\rho_q = \sum_k a_{k+q}^\dagger a_k$ is the q^{th} Fourier component of the electron density, Eq. 1.13 can be rewritten as:

$$H_{el-ph} = \sum_q g_q (b_{-q}^\dagger b_q) \rho_q \tag{1.15}$$

By introducing the normal coordinates, which can be expressed as $Q_q = (\hbar/2M\omega_q)^{1/2}(b_{-q}^\dagger b_q)$ and assuming the coupling constant g_q to be q-independent, Eq. 1.15 can be eventually re-expressed as:

$$H_{el-ph} = \sum_q \rho_q g Q_q (\frac{2M\omega_q}{\hbar})^{1/2} \tag{1.16}$$

The term

$$gQ_q[\frac{2M\omega_q}{\hbar}]^{1/2} = \phi_q \tag{1.17}$$

can be identified as an applied potential ϕ_q for the free electron gas. In the mean filed approximation this implies:

$$\rho_q = \chi(q,T)\phi_q \tag{1.18}$$

$\chi(q,T)$ is the Lindhard response function:

$$\chi(q) = \int \frac{f_k - f_{k+q}}{\varepsilon_k - \varepsilon_{k+q}} \frac{dk}{(2\pi)^d} \tag{1.19}$$

where $f_k = f(\varepsilon_k)$ is the Fermi function. The zero temperature q dependence of χ is plotted in figure 1.9 a for the one (1D), two (2D) and three dimensional (3D) electron gas. As shown in figure 1.9 b, χ is strongly dependent on the dimensionality of the system. A divergence occurs in the 1D case which is removed at finite temperature At $q = 2k_F$. The χ divergence in the 1D case is due to the peculiar topology of the Fermi surface (referred as *perfect nesting*) and has several important consequences, the main making the 1D electron gas unstable respect to the formation of a varying electron density of period π/k_F. A discontinuity in the first derivative occurs in the 2D case, while χ is continuous even in the first derivative in the 3D case.

Let us focus our attention on the phonon modes. By establishing the equation of motion for the normal state coordinates, it is possible to better understand the role of the electron-phonon interaction. The equation of motion can be obtained by commuting Q_q with the Hamiltonian 1.14:

$$\hbar^2\ddot{Q}_q = -[[Q_q, H], H] \tag{1.20}$$

Making use of the commutation rules and replacing ρ_q by means of Eq. 1.18, one finds:

$$\hbar^2\ddot{Q}_q = -[\omega_q^2 + \frac{2g^2\omega_q}{\hbar}\chi(q,T)]Q_q \tag{1.21}$$

thus, electron-phonon-coupling causes the renormalization of the frequency of the acoustic phonon coupled to the charge, with a new phonon frequency ω_{ren} given by:

$$\omega_{ren,q}^2 = \omega_q^2 + \frac{2g^2\omega_q}{\hbar}\chi(q,T) \tag{1.22}$$

The main result here is that on decreasing the temperature a softening of the phonon mode occurs for $q = 2k_F$ (see figure 1.10).

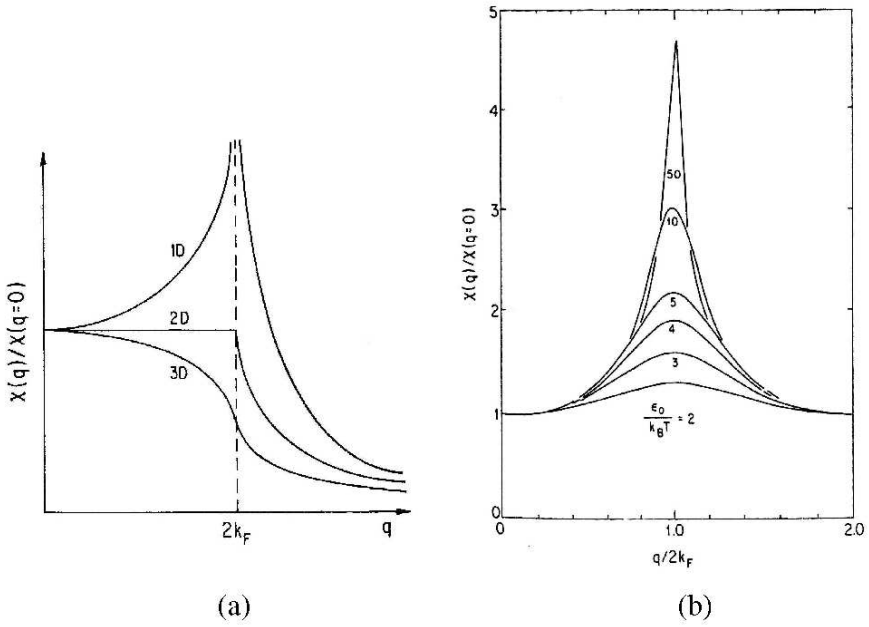

FIGURE 1.9: In a: zero temperature normalized Lindhard response function χ for a 1D, 2D, 3D electron gas as a function of q. In b: temperature dependence of $\chi(q)$ in the 1D case [21]. Arrow indicates increasing temperature.

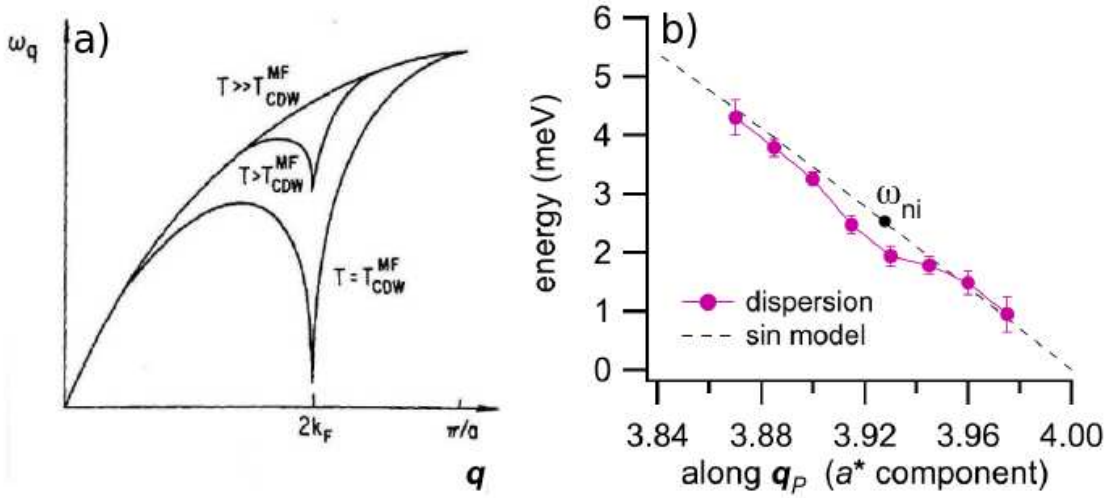

FIGURE 1.10: Theoretical [panel a)] and experimental [panel b)] Kohn anomaly phonon dispersion relation of a 1D metal after ref. [21] and [22] respetively; experimental data are collected on $ZrTe_3$ single crystal [22].

In 1D the phonon frequency drops to zero on decreasing temperature, indicating a lattice instability which implies the freezing of the lattice distortion and a back folding of the Brillouin zone (see figure 1.10). This effect is known as the Kohn anomaly. The periodic potential with $q = 2k_F$ opens up a gap at $k = 2k_F$ in the electronic bands and the ground state exhibits now a periodic spacial modulation of the charge density, called *charge density wave* [21]. For a given coupling g, the transition temperature at which the charge density wave arises can be defined as the T value at which $\omega_{ren} = 0$. For the higher dimensions the T dependence of χ is weak and a strong electron-phonon-coupling is required for obtaining a phase transition even at T=0.

The theory above summarized points out the role of the Fermi surface topology in leading the Peierls distortion. In real 3D systems the Fermi surface departs from that of an electron gas and in some cases can partially increase the instability conditions.

I want just to notice that during the research, I also studied the optical response under lattice compression of $CeTe_3$, which exhibits an almost perfect nesting of the Fermi Surface (FS) and an incommensurate charge-density wave (CDW), residing within the Te planes [23, 24]. The analysis of the Mid Infrared Reflectivity spectra allows to address both the pressure dependence of the CDW gap, as well as the behavior of the high frequency tail of optical conductivity σ_1 (see figure 1.11) which follows a power law behavior, rather consistent with a Tomonaga-Luttinger liquid scenario [25, 26].

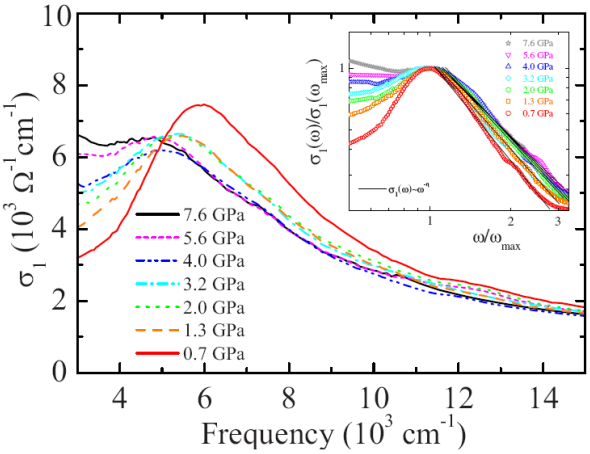

FIGURE 1.11: Optical conductivity $\sigma_1(\omega)$ of $CeTe_3$ at selected pressures. Inset high frequency tail of $\sigma_1(\omega)$ plotted on a bilogarithmic scale. The y-axis is scaled by the maximum of the midinfrared peak (around $\sim$ 6000 cm^{-1}), while the energy axis is scaled by the frequency ω_{max} where the maximum in $\sigma_1(\omega)$ occurs (see inset). The solid lines are power-law $\sigma_1(\omega)$-fits to the data.

Chapter 2

Insulator to metal transition

In the present chapter some example of MIT in several transition metal compounds will be presented and discussed. Making references to the microscopic mechanisms discussed in the previous Chapter, we will focus on the cases of Te, NiS_2, and VO_2, the principal systems considered in the present this work. As shown in figure 2.1, Te and NiS_2 show a pressure induced MIT about 4 GPa at room temperature, whereas VO_2 is characterized by a spectacular temperature driven MIT (5 orders of magnitude jump in conductivity): as discussed in details in the present Chapter, all of these materials are semiconductors at ambient conditions and the onset of the metallic phase can, at least in principle, be ascribed to different microscopic mechanism (Peierls, Mott, and charge transfer scenarios). In order to gain a deeper insight on the effect of the lattice compression, the research has been extended to families of doped compounds, like $NiS_{2-x}Se_x$ and $V_{1-x}Cr_xO_2$. A description of structural and electronic properties of all the same mentioned materials will be also schematically discussed.

2.1 Properties of Solid Tellurium

Recent developments in high-pressure techniques and advances in X-ray crystallography have led to a deeper inside of knowledge in structural phase transition of materials under pressure. Moreover recently discovered phenomena such incommensurately modulated structures [30, 31] have enriched the conventional phase diagram of the simple elemental system. Structural studies carried out under pressure on the group VI elements (Se, Te and S) have created a renewed interest in view of the fact that these elements undergo similar scheme of structural phase transitions, including incommensurate phases [32]. Among these, solid tellurium has attracted a great deal of interest for the

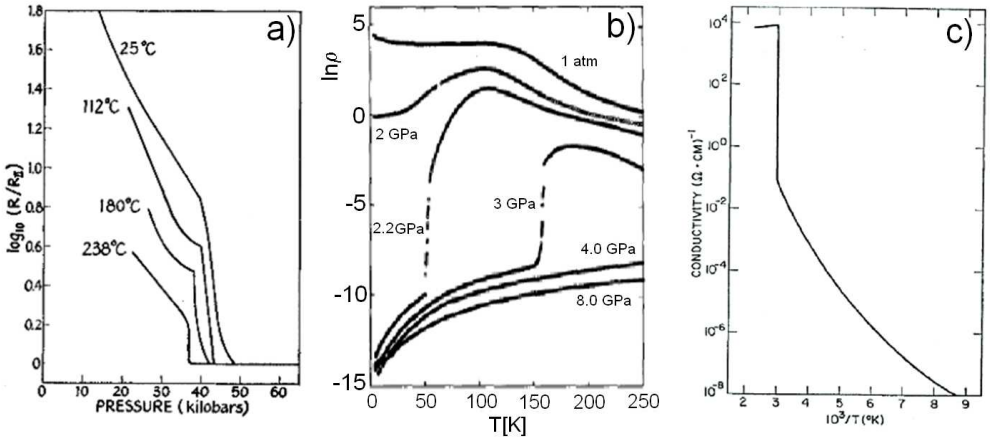

FIGURE 2.1: Resistivity of solid Te [panel a)], NiS_2 [panel b)] and VO_2 [panel c)] as function of pressure and temperature respectively, after ref. [27–29]

several fundamental theoretical issues it raises, such as the pressure-induced insulator to metal transition and the rich phase diagram with low-symmetry structures, which have prompted many experimental and theoretical studies. Despite the great experimental and theoretical efforts, the understanding of this system is still far from being complete. In particular the structural phase transitions scheme, recently revisited, and the electronic mechanism of MIT are still object of a large investigation. In the present thesis work Raman and Infrared spectroscopy coupled with high pressure techniques have been employed to gain a deep insight in both structural and electronic response to lattice compression.

2.1.1 Insulator to metal transition in solid Te

Elements belonging to the VI group exhibit very interesting properties. Among them, Se and Te are quite similar in the solid state: solid Te, as well as solid Se, are semiconductors, and their lattices consist of helical chains of atoms running along the c axis of the trigonal cell. According to resistivity measurements [27,33] shown in panel a) of figure 2.1, on increasing external pressure solid Te, which exhibits an anisotropic band gap of ~ 0.33 eV, evolves towards the metallic state achieved at the threshold pressure of ~ 4.0 GPa, where a simultaneous structural transformation from Te-I to Te-II is observed (see the next section). The first order insulator to metal transition can be explained by the fact that as the pressure increases, interatomic distances, and hence the volume per unit cell, are also decreased. The lattice compression is accompanied by a progressive structural symmetrization which leads

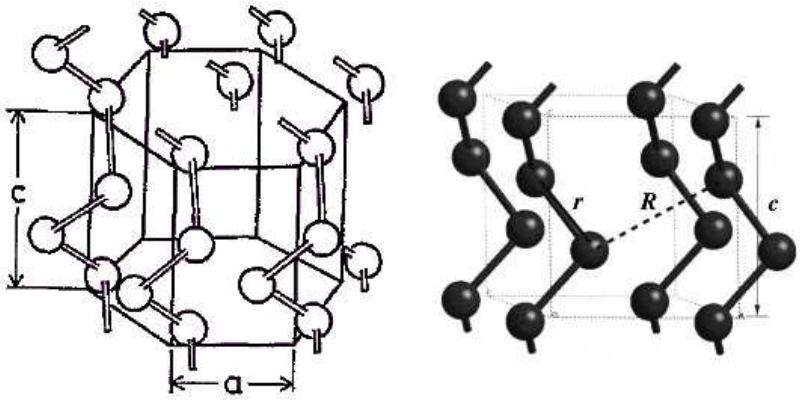

FIGURE 2.2: Crystal structure of Te-I at ambient condition.

to a gradual removal of the Peierls distortion (see the next section). Thus solid Te is transformed from a semiconductor system with an open chain-like hexagonal structure, characterized by covalent bonding and Van der Walls interactions, to a metallic system with a more closely packed structure and metallic bonds. Atoms approach closer to each other and as a result the conduction and valence bands overlap each other to form a single partially filled band, which gives rice to the metallic character of the high pressure phase.

2.1.2 Crystal structures of solid Te and phase diagrams

At ambient conditions, solid Te has a trigonal structure (Te-I) whose space group is D_3^4 or D_3^6, depending on screw axes direction. The unit cell contains three atoms, each having two nearest neighbours on the same chain with covalent-like bonds, and four second neighbours on the adjacent chains with Van der Waals interaction. The equilibrium lattice constants are $a = 0.4456$ nm and $c = 0.5927$ nm, the ratio of the helical radius to the interhelical spacing a is u = 0.2633, and each atom is spaced vertically by c/3 [34]. Te-I structure is sketched in figure 2.2. Nearest and second neighbours interatomic distances are 0.283 and 0.349 nm, respectively.

As well as for the other elements of the VI group, this crystal structure is usually discussed in term of a Peierls distortion of simple cubic lattice, identified by the three orthogonal 5p bands [35]. However, the p band is exactly half filled so that the lattice is unstable against a Peierls distortion which divides the six nearest neighbour bonds into three long (d_2) and three short bonds (d_1). The ratio of d_2/d_1 is equal to 1.23 for solid Te at ambient pressure and can be considered a measure for the strength of the Peierls

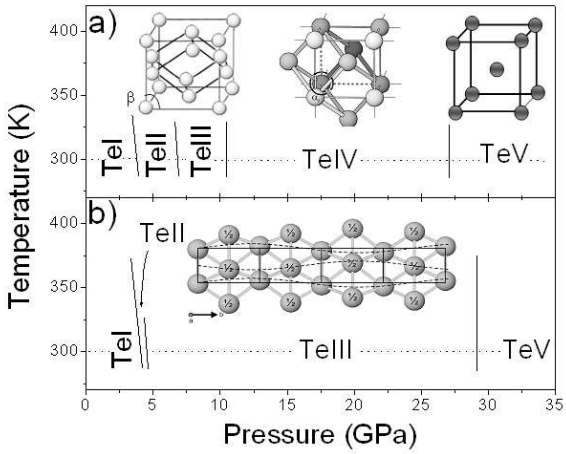

FIGURE 2.3: Schematic phase diagram of solid Te according to a) old and b) new phase transition sequences. Crystal structures are also sketched. After ref. [36–39]

distortion [35]. It is worth to notice that on applying pressure this ratio progressively approaches at 1, denoting a gradual reduction of the lattice distortion.

The main effect of pressure on the lattice structure is the reduction of the distances between neighbouring chains, leading to a progressive lattice symmetrization. Due to the similarity of the structures, x-ray-diffraction methods have not led to a decisive structure solution for the higher pressure phases.

For about two decades, starting from the early 80's, the generally accepted phase diagram predicts four phases as shown in panel a) of figure 2.3. On applying pressure Trigonal Te is transformed into a puckered layer monoclinic structure at 4.5 GPa [36] (Te-II, space group $P2_1$) with four atoms per unit cell and two bonds lengths (2.80 Å and 3.10 Å) stacked in the a-axis direction. On further increasing pressure up to 6.8 GPa, monoclinic Te-II is turned into orthorhombic Te-III (space group D_{3d}) with two atoms per unit cell [37]. Te-III consists of the same layer structure but with an unique bond length (3.04 Å). A phase transition from orthorhombic Te-III to β-Po-type Te-IV (space group $R\bar{3}m$), which can be reviewed as a rhombohedral distortion along [111] direction of a simple cubic lattice, takes place at 11 GPa [37]. In β-Po-type structure, the unit cell consists in 3 atoms and each atom has six first nearest neighbors and two second nearest neighbors. Finally a higher symmetry bcc structure with two atoms per unit cell and eight coordination number is reached at 27 GPa (Te-V). Te-V is found to be stable up to 40 GPa [38].

Recently new high pressure diffraction studies have suggested a different phase transition scenario [30, 39] (see panel b) of figure 2.3): trigonal Te-I undergoes a structural transition to triclinic Te-II at 4.0 GPa, followed at 4.5 GPa by a successive monoclinic Te-III phase, previously reported at 7 GPa. Te-II and Te-III coexist over a wide pressure range on pressure increase, and single-phase patterns of Te-III are observed only above 8.0 GPa. A close inspection of diffraction pattern from the single crystal of Te-III shows, in addition to the strong Bragg reflections, intense satellite reflections associated to an incommensurate lattice modulation, which is thought to be driven by a combination of sufficiently strong electron-phonon coupling and Fermi surface (FS) nesting [21], as also suggested by inelastic x-ray scattering measurements which have revealed a pronounced anomaly in LA phonon branch, which is shown to be dynamically unstable near wave vectors corresponding to the incommensurate modulation [40]. On further applying pressure Te-III structure is transformed into the bcc structure Te-V at 29.2 GPa [30, 39]. It

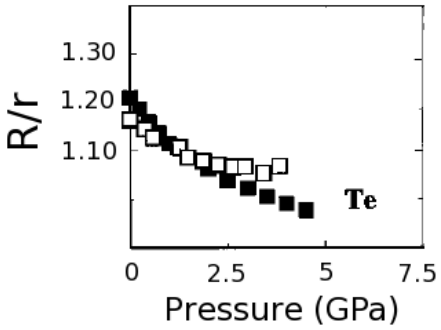

FIGURE 2.4: The ratio of the R (interchain) and r (intrachain) as a function of pressure. Open and filled symbols are experimental and theoretical R/r values respectively, after ref. [41]

.

is worth to notice that both sequences of the structural changes discussed are accompanied by a systematic increase of the coordination number. The trigonal structure of Te can be suitably represented in terms of the neighbor distance (intrachain) r and the nearest non-bonded (interchain) distance R, which can be determined from the structural parameters from the relations $r = \sqrt{3(ua)^2 + (c/3)^2}$ and $R = \sqrt{a^2(1-3u)^2 + r^2}$. It would be valuable to reexamine the high-pressure structural response of the system in term of R/r ratio shown in figure 2.4 [41]. Experimental results indicate that this ratio approaches a constant value (about 1.2), suggesting that lattice compression should reduce the structural anisotropy in the material and that the ratio should approach unity, increasing physical density so that more close-packed

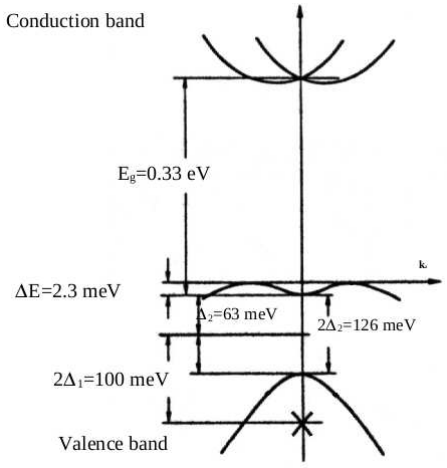

FIGURE 2.5: Schematic band structure of the top of the valence band of solid Te in the vicinity of the H points of Brillouin zone

.

structures such as body-centered monoclinic and cubic become energetically favorable.

Vibrational spectroscopy represents an alternative tool that can be used to investigate possible structural phase transitions and above all to understand the bonding properties. In Chapter 4, Raman spectroscopy will be employed to discriminate between different phase transition sequences.

2.1.3 Electronic structure of solid Te

Solid Te is one of the simplest examples of an anisotropic chain structure system. Reflecting the anisotropic nature of the crystal, the electronic structure of solid Te is peculiar. Since electrons up to 4d states constitute the atomic core, only 5s and 5p electrons are responsible for transport properties of the system. According to electrical measurements [27,33], at ambient conditions trigonal Te exhibits a semiconducting behavior with a narrow band gap of 0.33 eV between the highest valence band constituted by two of the four 5p electrons which are in non-bonding lone-pair (LP) orbitals, and the lower conduction band formed by anti-bonding orbitals (σ^*) between neighbouring chains. Charge transfer between the lone pair and σ^* orbitals and repulsive exchange interaction between lone pair orbitals seem to play an important role in stabilizing the spiral chain structure. Te-I band scheme structure is sketched in figure 2.5.

The top of the valence band is located in the vicinity of H point of the

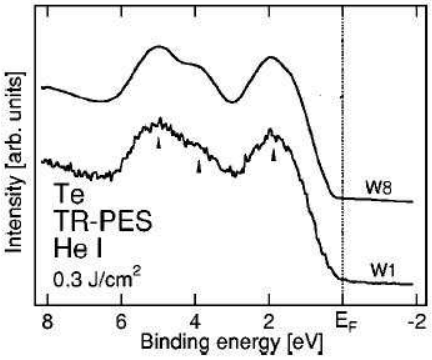

FIGURE 2.6: Photoemission spectra measured on solid Te. The small triangles point to the features described in the text. The spectra are normalized to acquisition time (W1 - W8). [42]

.

Brillouin zone and take the form of a characteristic camel-back shape. The height of the maxima from the saddle point H is 2 meV. The lower bands are mainly due to 4s electrons, while 5p electrons mainly contribute the upper bands. The bands which cross the E_f are mainly coming from 5p orbital. The major contribution to the density of states at Fermi level is, therefore, coming from 5p electrons, as also confirmed by photoemission spectroscopy studies [42]. The ultraviolet photoemission spectroscopy valence-band spectra are shown in figure 2.6.The spectra show two broad bands: one, at 2 eV binding energy, is the lone-pair p band, and the other, around 5 eV with a double-peak structure, is the bonding p band. There is no intensity at the Fermi energy E_F, as expected for a semiconductor with an energy gap of around 0.3 eV.

The band structure calculations in trigonal Te-I under pressure have been carried out using a self-consistent pseudopotential method [41,43] and a self-consistent Hartree-Fock-Slater method [44,45]. According to ref. [44,45], all bands progressively broaden with increasing pressure, leading to a band gap narrowing, which is a clear signature of the electronic instability of the semiconducting state. More recently the electronic structure and the structural instability of incommensurate monoclinic TeIII have been investigated by means of Density Functional Theory (DFT) calculations [46]. The *ab* initio calculations show that triclinic arrangement of the atoms or the incommensurate modulation along *b*-axis brings about a large dip in the density of states of 5p-band to lower the band structure energy.

At this stage, the analysis of the electron density as function of pressure would be very appealing at addressing the mechanism of the metallization

process occurring as consequence of the lattice compression. In the Chapter 4, DFT methods will be employed to study the pressure dependence of Te valence electron bands. Moreover electron density plot will be drawn at selected pressure.

2.1.4 Other measurements

The marked anisotropy of the trigonal structure is clearly reflected in the linear thermal expansion coefficient and principal Grüneisen parameter values measured parallel ($\alpha_{||}$) and perpendicular ($\alpha_{\perp}$) to the c axis, shown in figure 2.7 [47, 48]. Measurements have been made on the heat capacity in the temperature range 300 - 1.5 K. The results are shown in figure 2.7 inset a) as a plot of the apparent Debye temperature for the heat capacity C(T) against temperature [49]. For T $<$ 5 K the heat capacity may be described in terms of the usual low-temperature expansion and the limiting low-temperature value of the Debye temperature is $\Theta_D = 152$ K.

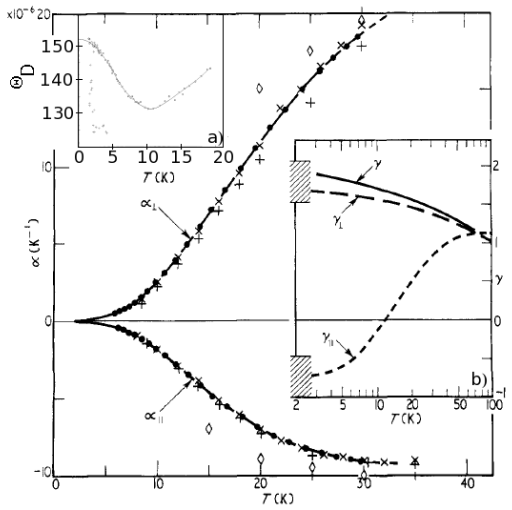

FIGURE 2.7: Principal linear coefficients $\alpha_{||}$ and $\alpha_{\perp}$ up to 30 K (close points from ref. [48], open diamonds from ref. [47]). Inset b) principal Grüneisen parameters. Inset a) Debye characteristic temperature Θ_D [49].

.

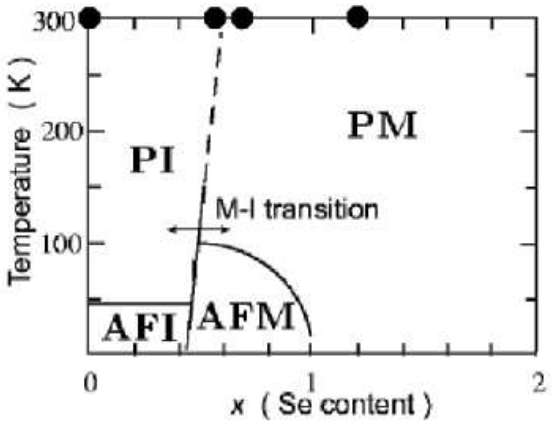

FIGURE 2.8: Schematic phase diagram of $NiS_{2-x}Se_x$ solid-solution (PI, paramagnetic insulator phase; AFI, antiferromagnetic insulator phase; PM, paramagnetic metal phase; AFM, antiferromagnetic metal phase) [50]. Filled circles (x= 0, 0.55, 0.6, 1.2) correspond to the compositions investigated in this study.

2.2 Properties of Nichel Selenium pyrites

A considerable number of experimental and theoretical studies have been carried out on MX_2 pyrites with M and X_2 (M = Mn, Fe, CO, Ni; X = Se, S, S-Se) forming a NaCl-type lattice. We will focus on the compounds belonging to the $NiS_{2-x}Se_x$ family. They are chalcogenides which exhibit MITs between magnetically ordered phases on varying the Se content (see figure 2.8), preserving the same cubic lattice structure [50]. The parent compounds NiS_2 and $NiSe_2$ differ significatively: whereas the former is a charge transfer insulator [51] the latter is a Pauli paramagnetic metal [52]. These two components can be mixed in all proportions, whereby a continuous changeover from one regime to the other is achieved.

2.2.1 Metal-insulator transition in $NiS_{2-x}Se_x$

Earlier work reported in the literature on $NiS_{2-x}Se_x$, were motivated by the fact that NiS_2 is a magnetic insulator, whereas $NiSe_2$ is a good metal: the isostructural solid solutions formed accurately obeys the Vegar's law [53, 54] (as discussed in the next paragraph) and displays intermediate anomalous electrical behaviour over the entire composition range $0 \leq x \leq 2$. A systematic investigation of electrical properties of $NiS_{2-x}Se_x$ has been reviewed [55]. Electrical resistivity ρ(T) for $NiS_{2-x}Se_x$ single crystals in the range $0 \leqslant x \leqslant 0.71$ as function of temperature is reported in figure 2.9.

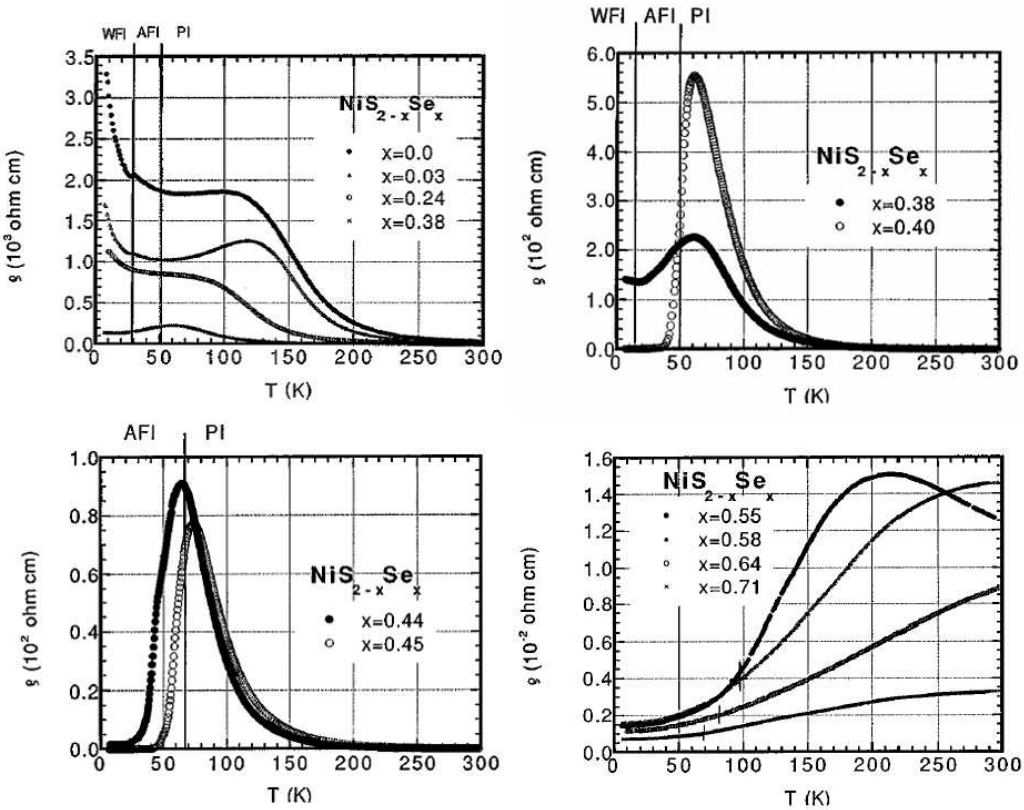

FIGURE 2.9: ρ vs T for single crystal $NiS_{2-x}Se_x$ in the range $0 \leqslant x \leqslant 0.71$. Increasing Se content, a metallization process occurs. [55]

A close inspection of Figure 2.9 reveals the general trend anticipated for the Se substitution process: in fact, the larger radial extension of the Se p orbitals as compared to those of S, suggests that $NiS_{2-x}Se_x$ solid solution moves, on increasing Se content, progressively towards metallicity. A similar trend is observed in the $(V_{1-x}Ti_x)_2O_3$ system [56] with increasing Ti content, although in the latter case the resistivity changes at the MIT are discontinuous. It should be also mentioned that electron-phonon coupling has been invoked to explain electrical transport properties for the insulating state of NiS_2 [57]. We will discuss this point in details in 5.1.1 section.

In the composition range $0 < x < 0.24$, $NiS_{2-x}Se_x$ is an insulator with lower and higher temperature activation energy of 330 and 110 meV respectively. At low temperature the alloys display a canted antiferromagnetic order with wider Slater energy gaps. ρ(T) exceeds 10^3 Ω cm as the temperature approaches to zero. Above 120 K, $NiS_{2-x}Se_x$ is paramagnetic with a charge gap that is roughly twice the activation energy. High and low temperature

gap sizes are almost independent of composition.

In the composition range $0.38 \leq x \leq 0.51$ $NiS_{2-x}Se_x$ is metallic at low temperatures in the sense that $\rho(T)$ is small and nearly temperature independent, except in the $30 - 50$ K temperature range, where $\rho(T)$ rises steeply, exhibiting a marked maximum at an intermediate temperature ($70 - 80$ K), enlightening the occurrence of a MIT. A possible interpretation of this feature in the resistivity curve is that a gap opens up in electron density of state. This signals the occurrence of a MIT. Beyond this maximum, $\rho(T)$ again drops exponentially on increasing the temperature, with a corresponding activation energy of 110 meV, the same value as for low substantial regime. In the range $0.51 \leq x \leq 0.58$ the features are rather like those of $0.38 \leq x \leq 0.51$ range except that the resistivities are much lower and the peaks in the resistivity curves decrease in magnitude and are broadened. Finally for $x > 0.6$ the alloy displays metallic characteristics, with ρ rising monotonically with T in the range below 10^{-3} Ω cm.

An alternative way to induce a MIT in NiS_2 is by applying hydrostatic pressure (as shown in panel b) of figure 2.1). While being experimentally challenging, the application of high pressures is the preferable way to tune the band width controlled MIT, since it does not introduce impurities and disorder. Resistivity measurements on pure NiS_2 and Se alloying compounds as function of pressure will be discussed the following 2.2.5 section.

2.2.2 Structural properties of $NiS_{2-x}Se_x$

The pyrites MX_2 contain interpenetrating face-centred-cubic (point group C_{31}) cation and anion arrays arranged in a NaCl-like structure obtained replacing the Na atoms by M and Cl atoms by anion pairs X as shown in figure 2.10. The unit cell contains four formula units. Crystal symmetry requires that the transition metal occupies a site in the lattice with octahedral coordination, and the chalcogenide atom occupies a site with tetrahedral coordination. A systematic x-ray diffraction investigation shows that all the compounds of the $NiS_{2-x}Se_x$ family are characterized by the same cubic structural phase with the a lattice parameter following the Vegar law, $a = (5.688 + 0.127x_{Se})$ $\mathring{A}$ where x_{Se} is the Se content [53, 54]. The presence of a single structural phase for all the Se concentration makes this system very suitable for a systematic investigations of electron correlation effects in driving the system towards the insulating state.

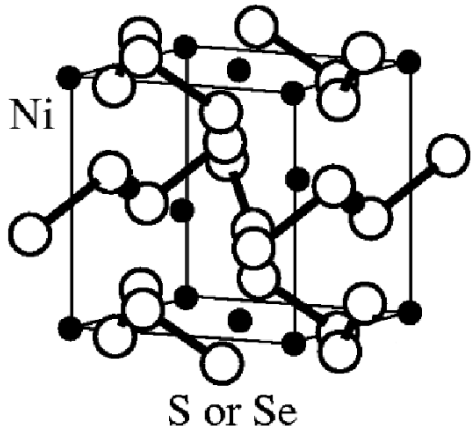

FIGURE 2.10: crystal structure of the $NiS_{2-x}Se_x$ solid solution. Ni and $(S, Se)_2$ pairs form a NaCl-type structure and each $(S, Se)_2$ pair is aligned parallel to another one.

2.2.3 Electronic structure

Quantitative evaluations of band structure of $NiS_{2-x}Se_x$ are still at a somewhat rudimentary stage, because of the difficulty of taking into account electron correlation effects, but an outline is beginning to emerge and a reasonable explanation of the main physical features of the system is today possible.

Goodenough's qualitative picture

Goodenough provided a conceptual framework for ordering the bands for electrons of topmost energy in materials with pyrite structures. Let us focus on pure NiS_2. Following references [58, 59], a good way of viewing the structure of pyrite is that of S_2 molecules dissolved in a face centered Ni crystal lattice. The octahedral symmetry of the metal atom causes a loss in degeneracy of these orbitals (cubic field splitting): two orbital sets of different energy and symmetry are created. The higher energy set contains two d orbitals of e_g symmetry while the lower energy set contains the remaining three orbitals which has t_{2g} symmetry. The electrons fill the orbitals according to the Hund's Rule and the Pauli Exclusion Principle. Indeed the e_g orbitals are half filled and are the highest occupied molecular orbitals, containing one electron in each e_g orbital. On the other hand, 3p orbitals of S_2^{-2} dimers will split into bonding σ, π and antibonding $(\sigma*,\ \pi*)$ states where σ, π and $\pi*$ are occupied and $\sigma*$ is unoccupied. According to this scenario, NiS_2 would be predicted a metal, although resistivity measurements reveal an insulator behaviour [55].

Let us now consider the electron correlation effects. Due to the strong

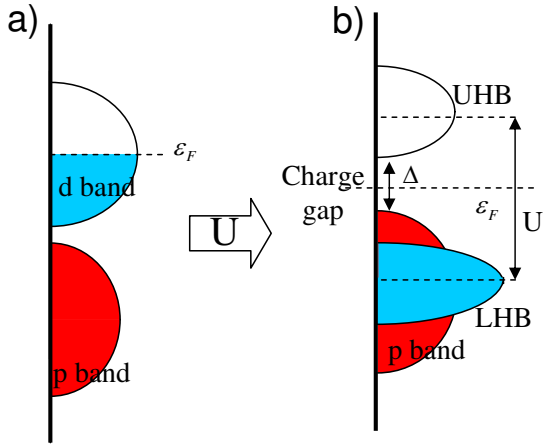

FIGURE 2.11: Qualitative electronic band structure of NiS_2 neglecting (a) or accounting for (b) the electronic correlation

Coulomb repulsion, metal transition 3d orbital are splitted into upper and lower Hubband band, with an energy spread of about 5 eV. In this energy gap S 3p orbital are located. In this band structure picture electron hoppings between Ni sites occur mediated by the chalcogenide sites, mainly caused by peculiarities of the pyrite crystal structure [61]. According to Zaanen Sawatzky Allen (ZSA) scheme, the insulating states of the system must be referred as charge-transfer insulator type (see figure 2.11). The charge transfer gap Δ is about 0.5 eV [51].

Let us discuss Se alloying effects on the system. Since S and Se are isoelectronic the substitution process does not alter the electron count. However, due the greater radial extension of Se orbitals with respect to S ones, Se alloying leads to an increase of wave functions overlapping and consequently to an increase of electron hopping probability, which is equivalent to a band broadening. A similar band-width controlled (BC) MIT has been also recognized in a series of $RNiO_3$, R being a rare-earth element from La to Lu, and the BC-MIT acting by the bond distortion of the orthorhombic perovskite [4].

Experimental results

Experimental information concerning the band structures of the $NiS_{2-x}Se_x$ system derives mainly from photoelectron spectroscopy. Early works of X ray photoelectron spectroscopic (XPS) in the range $0 - 25$ eV below the Fermi level E_F show for NiS_2 at 300 K the S 3p and Ni 3d bands overlap in

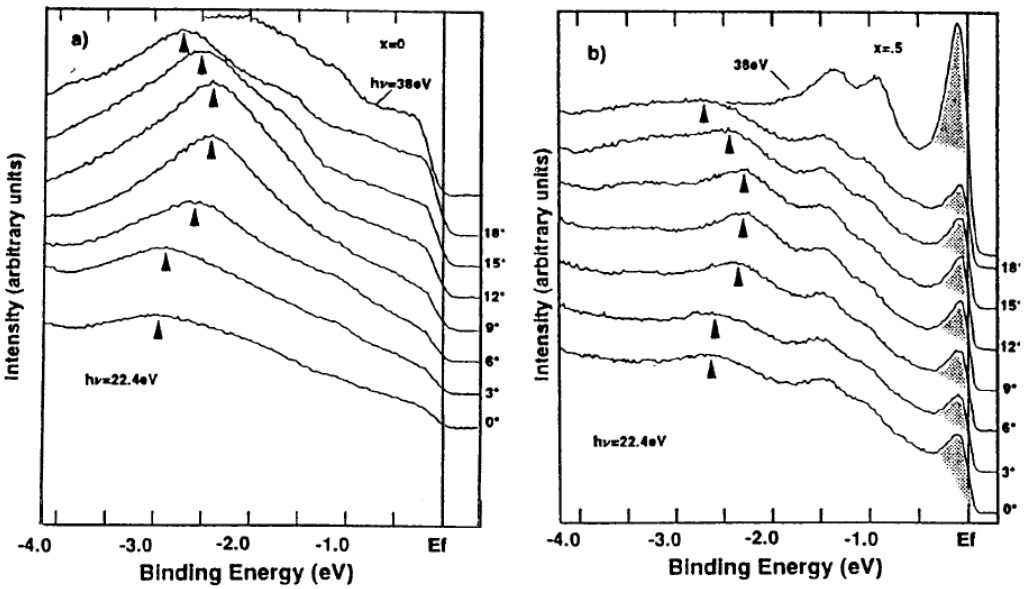

FIGURE 2.12: Valence band UPS spectra of (a) NiS_2 and of (b) $NiS_{1.5}Se_{0.5}$ [62]

this range of energies [52].

A detailed investigation via angle resolved photoemission spectroscopy on $NiS_{2-x}Se_x$ for the composition range $0 \leq x \leq 0.5$ has been carried out [62]. On the pure system, the shoulder near the Fermi energy E_F has been assigned to e_g states and is found to merge with the S 3p band [see panel a) of figure 2.12]. On increasing the Se contents, a noticeable shift of the anionic p band towards the Fermi level is found, without any drastic change in the energy separation between the t_{2g} and e_g bands or any shift with respect to E_F. A characteristic narrow band, absent in pure NiS_2, develops near E_F for x = 0.5 [see panel b) of figure 2.12], and loses spectral weight rapidly as the temperature is increased, as shown in figure 2.13. The appearance of the narrow peak cannot be explained by one-electron band theory. This suggests that the peak is due to many-body effects [62]. This spectral feature has been interpreted as a spectral weight transfer, indicating significant correlation effects in the system [62, 63]. Moreover the leading edge of this peak closely tracked the resistivity of the alloy over the temperature range $25 - 120$ K as shown in the inset of figure 2.13. This finding can be consider a direct evidence of the disappearance of the insulating state due to the gap collapse [62].

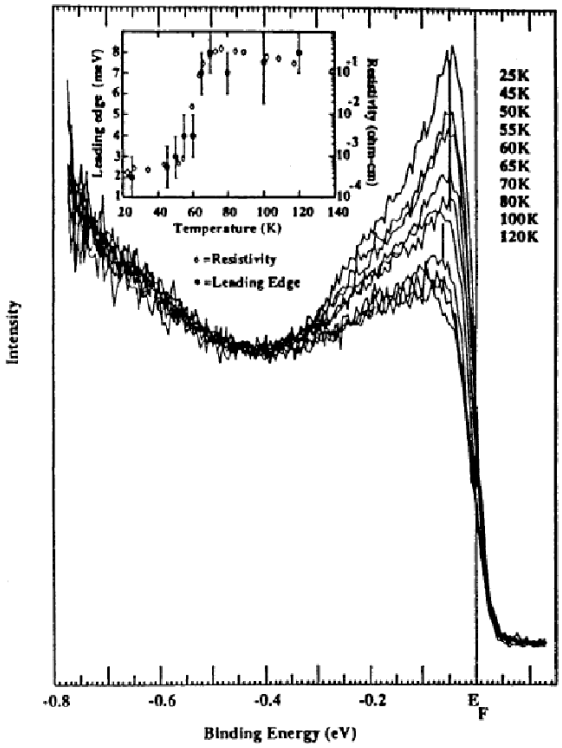

FIGURE 2.13: Temperature dependence of the UPS photoemission peak near the Fermi level. Note the similar temperature behaviour of the leading edge position and of the resistivity as function of temperature, as shown in the upper inset. After ref [62].

2.2.4 Other measurements

Heat capacity anomalies have been reported at the various phase transitions for NiS_2 [64], $NiSe_2$ [65] and for several intermediate compositions alloys [66, 67]. Entropies values at the concomitant transition differ considerably. Let us focus on the electronic contribution (γ) to the heat capacity for the metallic phase in the composition range $0.5 < x < 2$, as determined from low temperature heat capacity measurements. It is well known that elementary solid state theory predicts for the specific heat a power law relation ($C = \gamma T + aT^3$, where the aT^3 and γT are the contributions anticipated for lattice excitations and electron respectively [68]). As a consequence, plots of C/T vs T^2 should be linear, with the intercept yielding the value of γ. Actually, such plots are never quite linear for the $NiS_{2-x}Se_x$ system. Observed curvatures have been tentatively ascribed to spin fluctuations [69, 70]. Despite such problems, the γ values obtained by extrapolation from the essentially linear regions to the intercept, as carried out by the various investigators, are in

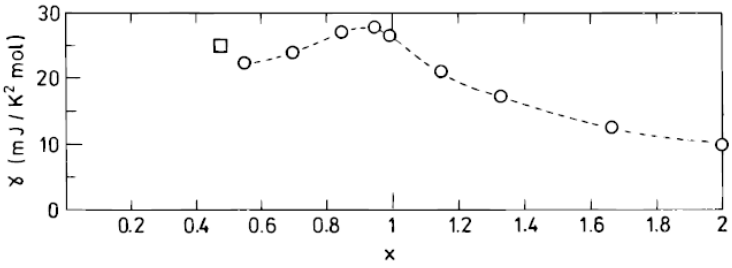

FIGURE 2.14: Values of the electronic contribution to the heat capacity of $NiS_{2-x}Se_x$ for x > 0.5. After ref [67]. The square symbol refers to unpublished measurements of Kim et al.

reasonable agreement. We show in figure 2.14 a compilation of γ values for x > 0.55; it is seen that the electronic contributions for the alloys are higher by a factor of up to 3 compared to the value $\gamma = 9$ mJ/mol K^2 for $NiSe_2$, which is a poor metal. This enhancement can again be directly linked to electron correlation mechanism, repeatedly invoked for alloys of intermediate composition x. It is of interest that γ peaks near x = 1 and 0.44; the former corresponds to the enhanced fluctuations near the AFM-PM boundary, whereas the latter reflects the effective mass enhancement near the AFM-AFI transition. Ultimately, however, the widening of the bands with increasing x becomes dominant, leading to an increase of charge mobility and to a reduction of γ.

2.2.5 High pressure studies

Whereas chemical substitution is a convenient method for varying magneto-transport properties of the Ni pyrite, it has several disadvantages. Indeed we have to deal with several samples whose real amount of substituted species is often not exactly known and impurities affecting the physical properties of the system can be introduced in different quantities in the different samples. Applying high pressure on a single sample can be a route to tune the physical properties of the system in a more systematic and controlled way. Indeed the effect of pressure on various physical properties of the NiS_2 system has been largely investigated.

Resistivity curves of pure NiS_2 single crystals showed a sharp drop on increasing pressure [see panel b) of figure 2.1], with an insulator to metal transition that occurs at room temperature at 4.6 GPa due to the increase of the electron bandwidth related to pressure induced lattice shrinking [28]. Below this critical pressure value the insulator to metal transition can be achieved only by cooling the system. The anomalous behavior of resistiv-

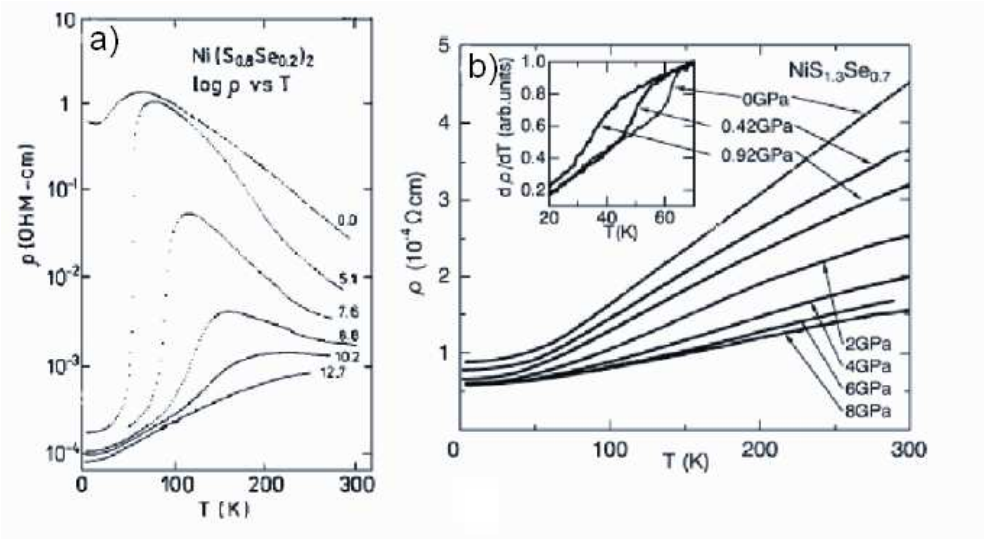

FIGURE 2.15: Electrical resistivity of a) $NiS_{1.6}Se_{0.4}$ [73] and b) $NiS_{1.3}Se_{0.7}$ [74] as a function of temperature for various pressure values. The inset of panel b) shows the temperature derivative of resistivity at selected pressures. A jump associated with antiferromagnetic ordering at Neel temperature can be seen [74].

ity corresponding to a para-antiferromagnetic transition was found in the metallic state [28].

Bearing in mind Se substitution effects on electronic structure of Ni pyrite, the application of pressure has been claimed to be equivalent to Se alloying [74]. In Se alloying compounds, a similar resistivity behaviour is observed in the composition range x = 0.0, 0.2, 0.4 [71]. On increasing the Se content in the composition range $0.5 < x < 1.2$, the application of pressure reduced the resistivities somewhat but did not greatly affect the trends in the variation of ρ with T [72]. Panel a) of figure 2.15 shows the variation in resistivity of a polycrystalline sample with x = 0.4 Se content as function of pressure [73]. On rising the pressure the hump in the resistivity curves becomes more prominent and then fades away beyond 1 GPa, while the resistivity at any given temperature drops on increasing the pressure. The equivalence of pressure and Se content has been somehow confirmed by the pressure dependence analysis of the Neel temperature for $NiS_{1.3}Se_{0.7}$ sample [see inset of panel b) of figure 2.15]. By comparing the pressure and x dependence of the Neel temperature, it results that the application of 1GPa corresponds roughly to 0.15 Se substitution in $NiS_{1.3}Se_{0.7}$ [74]. However no clear indication arises about the validity of this equivalence for all the Se alloying range.

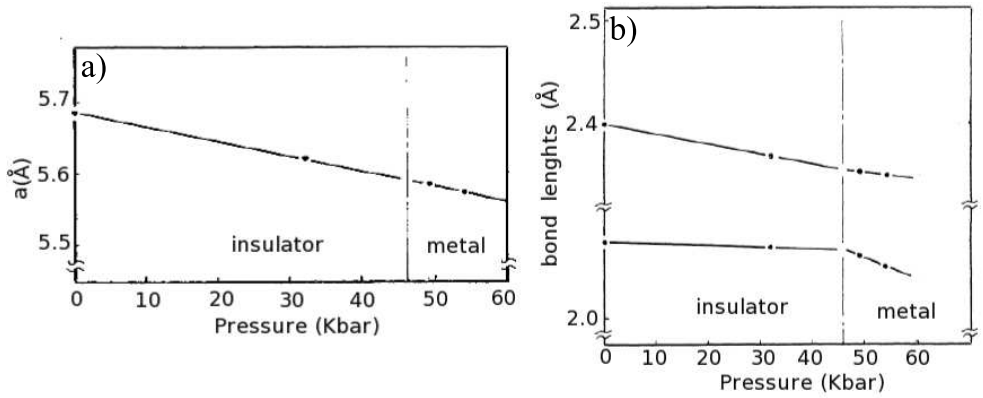

FIGURE 2.16: Room temperature pressure dependence of a) cubic lattice parameter a and b) bond lenghts in NiS_2 [75]

X-ray diffraction measurements on single crystal NiS_2 as function of pressure have been performed [75]. A careful analysis of structure changes and bond distances under pressure have been reported. The cubic structure is found to be stable over the whole explored pressure range (0-6 GPa). The pressure dependence of the lattice parameter a was found to be almost linear, also crossing the transition point [see panel a) of figure 2.16]. S-S bond distance is the feature most affected by the pressure: it remains fixed as long as the system is in the insulating state, whereas it diminishes with rising p > 4.6 GPa, where the system enters the metallic state; by contrast, the Ni-S distance decreases steadily [see panel b) of figure 2.16]. The pressure induced metal insulator transition affects also the compressibility of NiS_2 [76] which value is 9.2×10^{-4} GPa and 7.1×10^{-4} GPa for the insulating and metallic states, respectively.
As discussed above, the application of external pressure renders NiS_2 metallic, lowering the activation energy for conduction [61, 71, 77] and closely mimics the effect of increasing the Se admixture under ambient conditions. This can be seen from the comparison of figure 2.8 and figure 2.17, where a tentative of pressure-temperature phase diagram for NiS_2 can be drawn [78]. These observations suggest again that the various changes in physical properties of the $NiS_{2-x}Se_x$ system reflect alterations in electronic structure rather than structural effects or rearrangements.

However, it is worth noting that pressure and Se alloying act in an opposite way on the crystal structure, shrinking and expanding the lattice respectively. It seems almost reasonable that the two MITs, induced by pressure and Se alloying respectively, may be guided by different electronic mechanisms, as it will be pointed out from ours measurements, resolving this

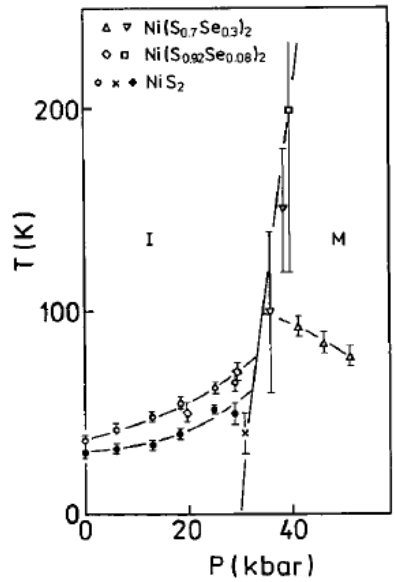

FIGURE 2.17: Phase diagram as function of pressure and temperature for $NiS_{2-x}Se_x$ on varying the Se content [78].

apparent paradox.

2.2.6 Quantitative Interpretation of Experimental Findings

The experimental observations discussed in previous sections can be rationalized by drawing on the theory of electron correlation effects. This approach is justified by the fact that with increasing x the $NiS_{2-x}Se_x$ system evolves from a Mott-Hubbard insulator to a poor metal. As discussed above, under the simplest approximation, the crystal field splits the Ni-d levels into a lower set of threefold degenerate levels (t_{2g}) and an upper set of twofold degenerate levels (e_g). Therefore, a model Hamiltonian, analogous to eq. 1.7, may be constructed from half-filled e_g states of Ni 3d and filled σ^* of S_2 3p [12, 62] as:

$$H = \sum_{<ij>\sigma} t(d^\dagger_{i\sigma} p_{j\sigma} + p^\dagger_{i\sigma} d_{j\sigma}) + \tag{2.1}$$

$$(\epsilon_d - \mu) \sum_{i\sigma} n_{d,i\sigma} + (\epsilon_p - \mu) \sum_{i\sigma} n_{p,i\sigma} + U \sum_i n_{d,i\uparrow} n_{d,i\downarrow}$$

where $d^\dagger_{i\sigma}$ ($p^\dagger_{i\sigma}$) is the creation operator of an $e_g(\pi^*)$ electron with spin σ at site i and $n_{d,i\sigma}$ ($n_{p,i\sigma}$) is a number operator of $e_g(\pi^*)$ electrons with spin

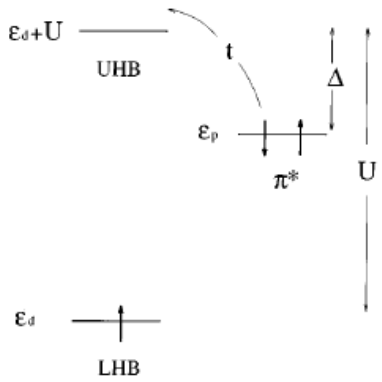

FIGURE 2.18: Schematic band structure of NiS_2 according to the Hamiltonian 2.2 [12].

σ at site i. The electron hopping is considered only between the nearest-neighbor Ni and S_2 and only the on-site Coulomb repulsion on Ni is assumed to be appreciable. The undoped material NiS_2 has a charge-transfer gap $\Delta(= \epsilon_d + U - \epsilon_p)$ between the occupied π^* band and the empty e_g band and is expected to correspond to the parameter region $t << \Delta$ for which the ground state of the Hamiltonian is a charge-transfer insulator (see 1.2 section), as shown in figure 2.18.

Although Local Density Approximation (LDA) band-structure calculations usually fail in reproducing insulating ground state in strong correlated system, many of the experimental features related to electronic structure of $NiS_{2-x}Se_x$ compounds are correctly captured by Hamiltonian 2.2, evaluated within this theoretical framework [62]. According to LDA predictions, bonding and antibonding S_2 dimer are separated of 9.5 eV. Also Ni 3d bands split into an upper and lower Hubbard band with an energy gap of 5 eV. According to this interpretation, NiS_2 is a charge-transfer insulator with its gap, $\Delta = 2$ eV, between the filled antibonding S_2 band and the empty upper 3d Hubbard band. The relative positions of the p and d bands are confirmed by a resonant photoemission experiment revealing that the top of the valence band has p character [50].

2.3 Properties of vanadium dioxide

The vanadium oxides comprise compounds with different formal vanadium valency stages, which range from two in VO, three in V_2O_3, and four in VO_2 to five in V_2O_5. In addition to these configurations mixed valent compounds

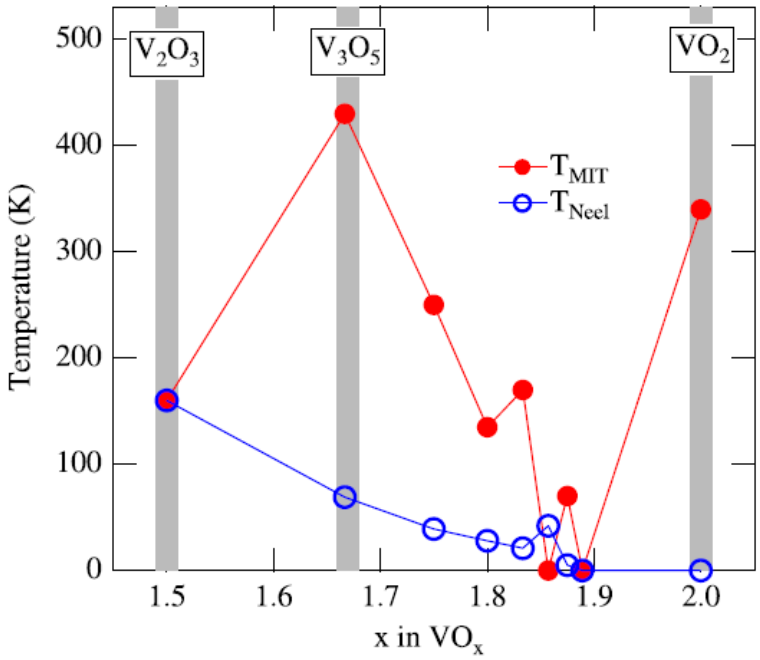

FIGURE 2.19: Metal to insulator transition temperatures and magnetic ordering temperatures of compounds belonging to the Magnéli phases. After Ref. [80].

can be synthesized. Among the latter, the so-called Magnèli phases [79], defined by the general stoichiometric formula:

$$V_nO_{2n-1} = V_2O_3 + (n-2)VO_2 \tag{2.2}$$

where $3 = n = 9$, are of special interest since they give rise to closely related compounds with peculiar physical properties [80]. All compounds of the Magnèli serie, with the only exception of V_7O_{13}, display a first-order MIT (see figure 2.19). Among V_nO_{2n-1}, VO_2 (n $=\infty$) shows a MIT on decreasing the temperature below $T_{IM} = 340$ K, characterized by a simultaneous structural transition from rutile to monoclinic phase, which fact hindered to clearly identify the structural or the electronic degrees of freedom as the origin of the transition. Despite intense work over four decades the understanding of the MIT in VO_2 is still far from being complete. Several models have been proposed, ranging from Peierls-type to Mott-Hubbard-type scenarios, stressing, to a different degree, the role of lattice instabilities and electronic correlations in driving the system towards the insulating phase. The structural peculiarities of the MIT in VO_2 led to identify the V-V dimerization as a key mechanism in driving the systems into the insulating phase and thus the MIT in VO_2 was initially ascribed to a Peierls instability. However the

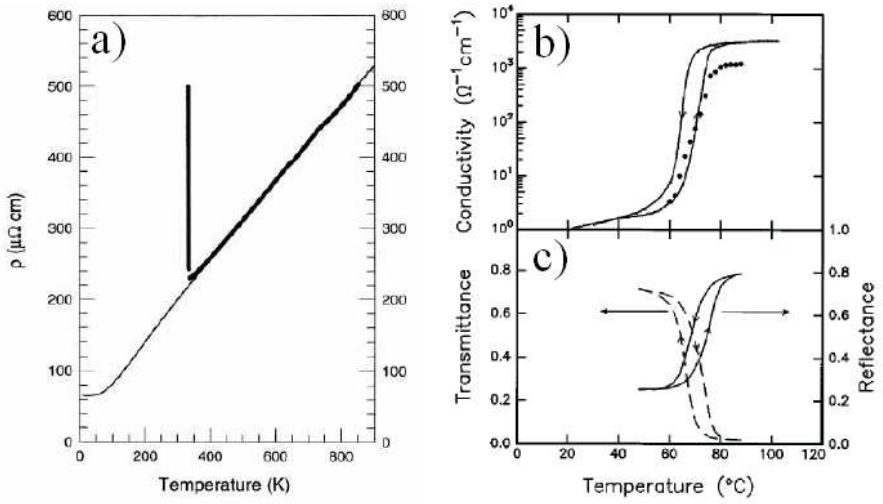

FIGURE 2.20: Panel a) VO_2 resistivity as a function of the temperature from ref. [89]. Panel b) and c): temperature dependence of DC conductivity (a) and of reflectance and transmittance at 2000 cm^{-1} (b) of a VO_2 thin film on sapphire substrate (film thickness 1500Å) from ref. [88].

splitting of the d band due to the lattice distortion is expected to be much smaller than the observed value ($\sim$ 2.5 eV) [81]. Yet, neither of these pictures has been so far successful in explaining a broader range of the physical phenomena shown by VO_2.

2.3.1 Insulator to metal transition in VO_2

According to resistivity measurements [29], shown in panel c) of figure 2.1, VO_2 undergoes a temperature driven MIT characterized by an abrupt jump in resistivity, up to five orders of magnitude in high quality crystalline samples [82–84] and accompanied by a transition from rutile to monoclinic structure [85, 86]. Since the electrical conductivity σ along the c axis being only twice larger than the *in plane* value [84, 87, 88], σ in metallic VO_2 phase is nearly isotropic. The activation energy below T_{IM} is about 0.5 eV. In the high temperature metallic phase, an anomalous linear temperature dependence of resistivity up to 800 K has been observed [see panel a) of figure 2.20] [89].

Optical properties of VO_2 began to be studied shortly after Morin's paper of 1959 [29]. Optical transmission of polycrystalline VO_2 thin film has been reported in the photon energy range 0.25 eV $\div$ 5 eV, with the gap edge identified at $\sim$ 0.7 eV [81, 87] (see 2.3.4 section). This change in the relative transmittance of VO_2 thin films is more easily observed in the infrared region [88]. At the MIT, the transmittance of thin VO_2 films drops to zero, while

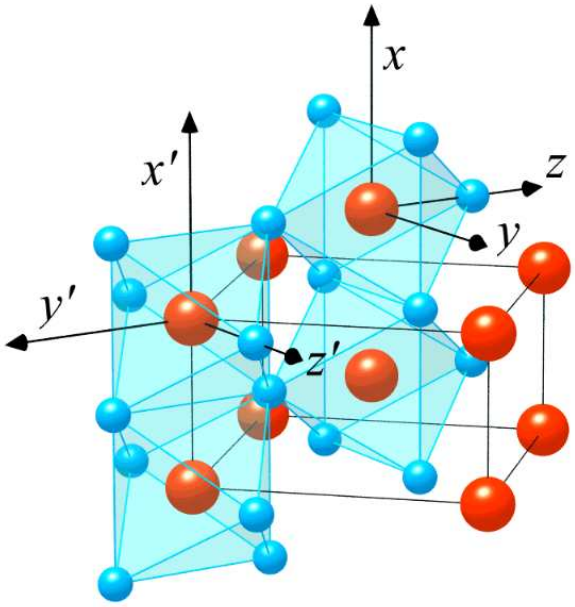

FIGURE 2.21: VO_2 rutile structure. Spheres indicate V ions; oxygen ions are placed at the octahedra vertexes.

reflectance rises [see panel b) of figure 2.20].

Conductivity, as well as optical properties, shows a thermal hysteresis, whose temperature width ranges between 1 and 5 degrees, depending on the sample quality, and being lower on samples with higher conductivity discontinuity. In the insulating phase, no long-range magnetic order evidences are provided by both susceptibility and NMR measurements [84,90]. These characteristics make this system very appealing for technological applications for instance in window coatings, infrared sensors, transistors, or opto-electronic memories and switches [91–93].

2.3.2 Structural transition in VO_2

Rutile phase

The rutile structure of metallic VO_2 is displayed in figure 2.21. It is based on a simple tetragonal lattice formed by V atoms, each surrounded by an oxygen octahedron, with space group D_{4h}^{14} ($c = 2.8514$ Å, $a = 4.5546$ Å). VO_6 octahedra form edge-sharing strings and consequently V atoms are equally spaced (separation 2.88 Å) along the c axis (see figure 2.21). Octahedra centered at the corners and at the center of the cell are rotated by 90° around the tetragonal c axis relative to each other and the octahedral edge-sharing

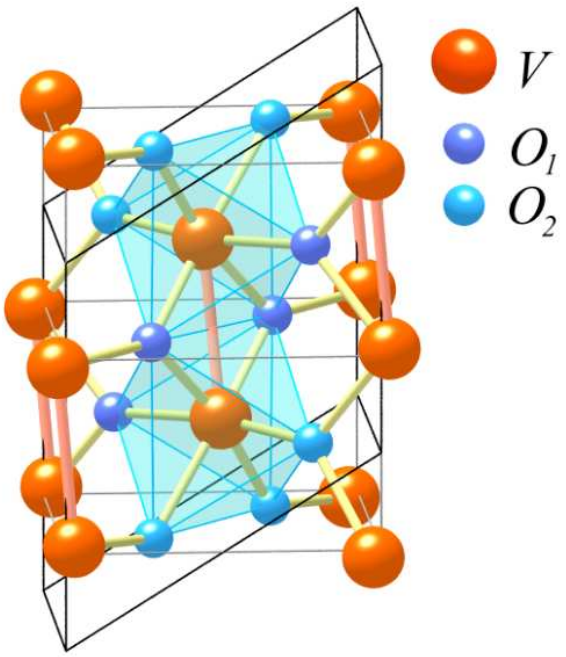

FIGURE 2.22: Schematic representation of V-V dimerization in the M1 monoclinic structure of VO_2.

strings are interlinked via corners. The apical V-O distance is 1.933 Å and the equatorial V-O distance is 1.920 Å. Unit cell contains two unit formula [85].

Monoclinic M1 phase

On decreasing temperature below 340 K the system enters the M1 monoclinic insulating phase. In this structure, in each V-V chain, V ions form pairs along the c axis (separation 2.63 Å within pairs and 3.16 Å between pairs). In addition each V-V pair is tilted respect to the c axis, leading to a zigzag pattern [86] (see figure 2.22). Due to such distortion, a doubling of the unit cell occurs along the c axis, with space group changing from D_{4h}^{14} to C_{2h}^{5}. The unit cell contains four unit formula. The lattice constants and the monoclinic angle are a_{M1}=5.743 Å, b_{M1}=4.517 Å, c_{M1}=5.375Å, and β_{M1}=122.61°, respectively. Since b axis contracts, but c and a axis expand on entering the M1 phase, the change in volume ΔV is rather small (ΔV$\simeq$0.04%). Besides the two V-V bond lengths, as a consequence of the lattice symmetry reduction, two different apical V-O bond lengths of 1.77Å and 2.01Å appear. Moreover, the lateral displacement of the vanadium atoms causes a shift relative to the rather fixed oxygen octahedra, therefore affecting the $(p-d)$-like V-O bonding and leading to two short and two long equatorial V-O bond

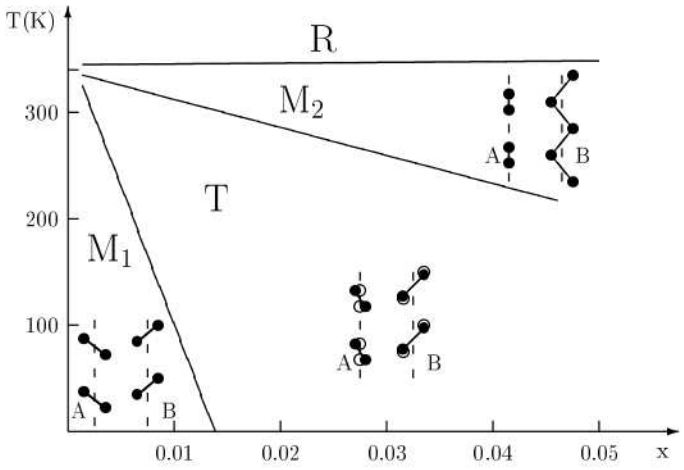

FIGURE 2.23: $V_{1-x}Cr_xO_2$ phase diagram as a function of temperature and Cr concentration x from Ref. [98]. R indicates the metallic rutile phase; M1, M2, M3 indicate the three different insulating monoclinic phases

lengths of 1.86, 1.89, 2.03, and 2.06 Å. The distortion from the rutile phase to the monoclinic phase on entering the insulating phase was originally ascribed to a Peierls dimerization of the V-V chains, equally spaced along the c axis in the rutile phase. This point will be further discussed in the following.

2.3.3 Cr-doped compounds: M2 and M3 phases

The understanding of VO_2 and the MIT is even more complicated due to the presence of additional phases of this material, which appear under peculiar growing condition or on applying of uniaxial stress or on doping of the system with small amounts of donor/acceptor impurities of the order of few percent [94, 95]. These can be interpreted as metastable phases for VO_2, whose free energies at ambient conditions are slightly higher then that the M1 phase [96]. Donor impurities, such as W or Nb, strongly reduce the insulator to metal transition temperature (W doping reduces T_{IM} of about 20 K/W%) and increase the conductivity in the insulating state [97]. As an example, on doping with few percent of W, resistivity of VO_2 increases by two orders of magnitude, with a strong reduction of the activation energy of the insulating phase, which suggests the presence of an impurity band below the gap, at about 0.05 eV [97]. The effect of these impurities can be described by conventional extrinsic semiconductor theory. On the contrary, acceptor impurities, such as Cr or Al, lead to negligible effects on conductivity on both the insulating and the metallic phases, but give rise to important structural

modifications. On doping VO_2 with a small amount of Cr two additional monoclinic insulating phases appear, characterized by a different extent of the Peierls distortion. The study of these compounds is important in order to address the role of the lattice symmetry breaking in driving the MIT in VO_2. The phase diagram as a function of the Cr substitution fraction x is shown figure 2.23, as given by Marezio *et al.* in Ref. [98]. According to figure 2.23, Cr-doped VO_2 enters, on cooling, the monoclinic M2 phase in a first order metal-insulator transition [112]. On further decreasing the temperature, transition to the triclinic M3 (also called T) phase occurs [99,100], which, for Cr concentrations smaller than 0.015, is followed by a first order transition to the monoclinic M1 phase [98]. According to X-ray measurements by Marezio et al., each of the three low-temperature phases shows a particular distortion pattern of the atomic arrangement especially of the characteristic vanadium chains (see figure 2.24). Whereas in the M1 phase both the metal-metal pairing and the zigzag-type lateral displacement are observed on each chain, in the M2 phase only half of the chains dimerize and the zigzag-type deviations are reserved to the other half of the chains. Finally, the M3 (T) phase is intermediate, as those chains, which in the M2 phase dimerize, gradually start to tilt, whereas the zigzag chains start to dimerize until distortions in both chains are identical and eventually the M1 phase is reached. Hence, the M3 (T) and M1 phases can be regarded as superpositions of two M2-type displacements with unequal and equal weights, respectively.

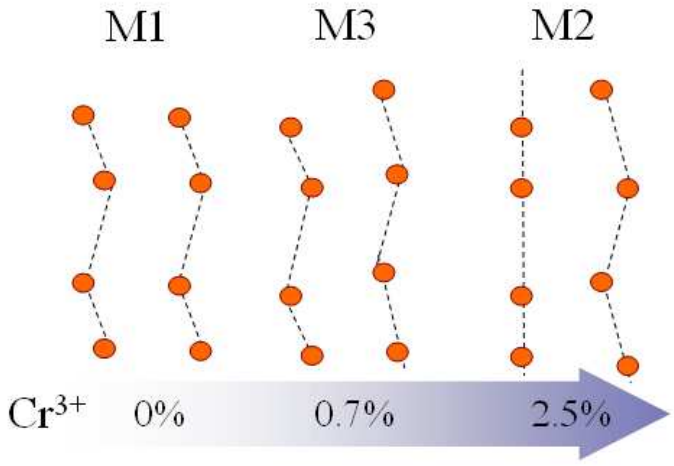

FIGURE 2.24: Schematic representation of the V-chains distortion patterns in the M1, M3 and M2 monoclinic phases of $V_{1-x}Cr_xO_2$.

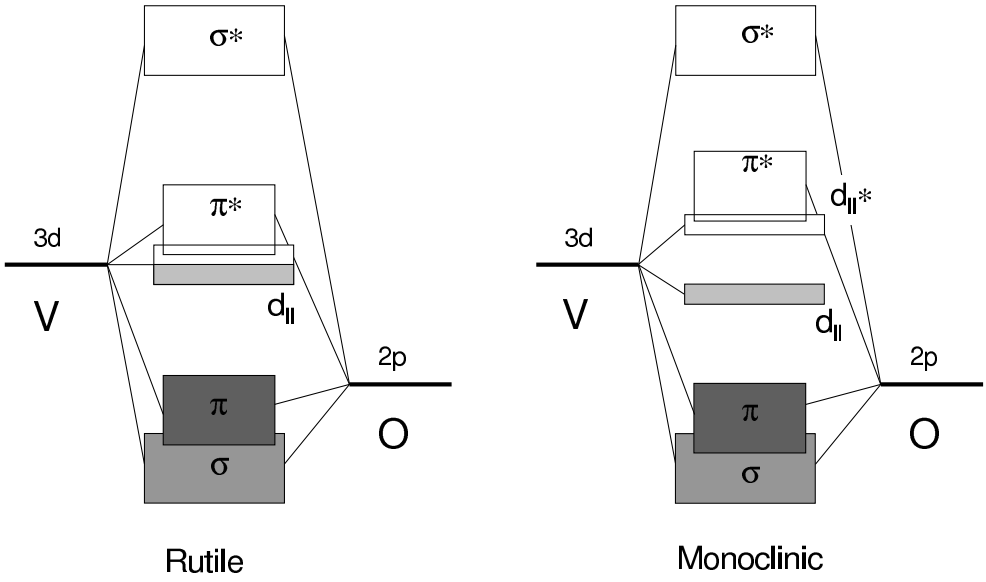

FIGURE 2.25: Schematic representation of the VO_2 electronic structure in the metallic rutile and in the insulating monoclinic phase. Empty blocks represent unfilled bands.

2.3.4 Electronic structure

Goodenough's qualitative picture

Within the ionic approximation, vanadium valence is +4, with one electron filling the external $3d$ levels, and in a simple picture it could be expected to be a metal with an half filled band, but experiments indicate that the compound is in fact an insulator. Many of the main aspects of the electronic properties of VO_2 have been qualitatively captured long ago in a molecular orbital description by Goodenough [58], who first proposed that the lattice distortion, leading to the R to M1 transition i.e., the V-V pairing and their off-axis zigzag displacement, implies a band splitting with the formation of a Peierls-type gap. Let us consider the rutile structure. The tetragonal crystal field removes the five-fold degeneracy of the 3d levels leading to the t_{2g} triplet and the e_g doublet. Two of the 3 t_{2g} orbitals are mixed with O $2p$ orbitals, leading to the σ and π low lying filled bands (see figure 2.25).

The corresponding antibonding orbitals give rise to the empty σ^* and π^*

bands. On the contrary the last V t_{2g} orbital lies along the c-axis direction and grants a strong direct overlap with neighboring V in the chains, giving rise to the partially filled $d_{\|}$ band. In order to account for the quasi orbitally isotropic metallic state in the Goodenough picture, an overlap between the $d_{\|}$ band and the bottom of the empty π^* band was postulated.

On entering the monoclinic phase, the V-V pairing within the vanadium chains parallel to the rutile c axis causes the splitting of the $d_{\|}$ band into filled bonding and empty antibonding states, with the formation of a Peierls-like gap between them. Moreover the zig-zag displacement of V ions increases the $p-d$ overlap, causing a shift of the filled π band toward lower energies and a rise of the empty π^* band. According to Goodenough, the rise of the π^* band is crucial in leading the MIT. In this configuration (see figure 2.25), the electronic state within the dimers is a localized singlet state, which explains both the insulating and diamagnetic character of VO_2.

First principles studies based on molecular dynamics and local density approximation (LDA) confirmed this general molecular-orbital scheme, which ascribes the MIT to the lattice distortion [101,102]. The same order of bands for the insulating and the metallic phases have been obtained, confirming the splitting of the $d_{\|}$ band and the rise of the π^* band. However, as will be discussed in section 2.3.5, these theories fail in describing the gap opening, and thus the insulating phase, suggesting a key role played by electronic correlation.

Experimental results

Experimental information concerning the band structures of the VO_2 has been provided by optical and photoemission experiments, which confirms the scenario traced by Goodenough. According to optical and photoemission measurements [81,87,103] the lowest unfilled $3d$ levels of V lie well above the top of the $2p$ O bands. In panel a) of figure 2.26, ultra-violet photoemission spectroscopy (UPS) data of metallic and insulating VO_2 from Ref. [81] are shown. In the insulating phase it is quite evident the band at around 0.9 eV, ascribed to the $d_{\|}$ band, showing a bandwidth of about 1.5 eV. Ultra-violet reflectance measurements [81] allowed for an estimation of the $d_{\|}$-$d_{\|}^*$ splitting, which results to be rather large, about 2.5 eV, and a rise of about 0.5 eV of the π^* band at the MIT has been proposed [see panel b) of figure 2.26]. The rise of the π^* band implies a charge redistribution to the $d_{\|}$ band. Orbital polarization from nearly isotropic in the metallic phase to completely polarized in the insulating phase was recently probed by means of soft-x-ray absorption spectroscopy [104].

The analysis of the symmetry and energies dependence of electronic struc-

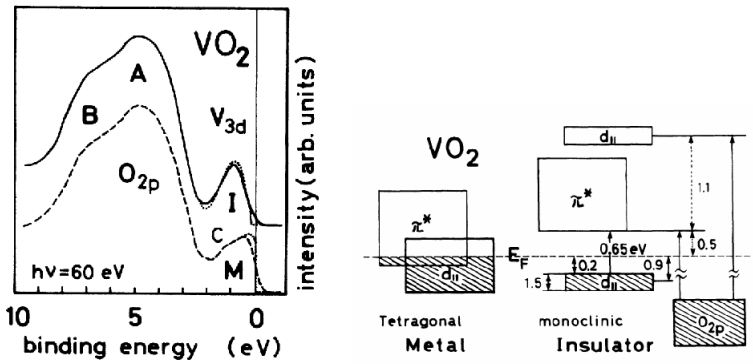

(a) (b)

FIGURE 2.26: Panel a: Ultra-violet photoemission spectroscopy (UPS) results for VO_2 in the metallic (M) and the insulating (I) phase. Panel b: Schematic energy diagram obtained combining UPS, ultraviolet and infrared spectroscopy [81].

tures of VO_2 across the T-dependent MIT have been recently reviewed in a detailed photoemission and X-ray absorption studies of valence and conduction bands [105,106]. The energy position and width of O 2p and V 3d bands are in good agreement with those of the previous works. The observation of a V 3d spectral weight transfer occurring at the MIT has been interpreted as a signature of both electron-electron and electron-phonon interactions, as better discussed in the following section.

2.3.5 Role of electronic correlation

Several theoretical works reported on *ab initio* electronic structure calculations, based on local density approximation (LDA) and molecular dynamics [101,102]. These calculations demonstrated that the structural transition in VO_2 is responsible for the splitting of the $d_{\|}$ band and for the rise of the π^* band, in qualitative agreement with experimental results and addressing the MIT to a Peierls-like mechanism. However these calculations do not yield the *complete* opening of the gap in the monoclinic phase, which on the contrary is rather large ($\sim$ 0.7 eV), but a 0.04 eV overlap between the $d_{\|}$ band and the empty π^* band was obtained [102]. Moreover the splitting of the $d_{\|}$ band due to the lattice distortion is expected to be much smaller than the observed value ($\sim$ 2.5 eV [81]). Similar results have been obtained for the M2 monoclinic phase [102]. From the early studies on VO_2 the impossibility to obtain the insulating phase within first principle calculations opened a debate

on the role of the electronic correlation and on whether the MIT is driven by a Mott-Hubbard rather than a Peierls-like mechanism [91, 96, 101, 107]. Nowadays this question has not yet a clear answer.

Experimental evidence for strong electronic correlation in VO_2

There are many experimental evidences of strong electronic correlation in VO_2. First of all in the rutile phase VO_2 shows typical features of a correlated metal. The anomalous linear temperature dependence of resistivity above T_{IM} (see panel a) of figure 2.20) with the absence of saturation observed up to 800 K is inconsistent with band calculations and suggests that metallic VO_2 is close to the Mott-Hubbard insulator and differs from a conventional Fermi liquid [89]. Moreover a large red-shift of the plasmon resonance, which vanishes in the insulating phase, has been observed in metallic VO_2 by means of termoreflectance measurements [108]. This result points out the presence of a precursor of the MIT and is in good agreement with recent optical measurements (that will be discussed in detail in Chapter 6), showing the occurrence of a redistribution of spectral weight (i.e., the frequency-integrated optical conductivity) within a broad energy scale (~ 5 eV) [109]. This suggests electronic correlation to be crucial for the MIT, even though the insulating state may not be a conventional Mott insulator because of the V-V pairing.

Above all these results, the existence and the relative electronic properties of the M2 phase in Cr-doped samples as well as in pure VO_2 (available by peculiar growing condition [110]), are a topic very difficult to reconcile with all those theoretical approaches, which addressed the MIT to the structural transition only. Indeed in the M2 phase half of the V-V chains shows the pairing but not the zigzag displacement, while the other half show the opposite. To account for the insulating behavior of M2 VO_2, Goodenough proposed a splitting of the partially filled π^* band together with the $d_{\|}$ band [111], but the continuous transition from M1 to M2 through the M3 phase rules out any reordering of the bands between these two phases [112]. For this reason, as stressed by Rice *et al.* [96], all the insulating phases of VO_2 were of the same type. In this view, both the pairing, which splits the $d_{\|}$ band, and the off axis displacement, which rises the π^* band, are essential to open the gap. Therefore the insulating behavior of the M2 phase was exploited as the main point against band theory [96]. Furthermore, NMR and EPR measurement indicated that V^{4+} ions forming equally spaced V chains behave magnetically as S=1/2 Heisenberg chains. This result strongly supports the idea that this system is close to a Mott-Hubbard insulator.

The question whether the physics of the insulating low-temperature phase

is dominated by the Mott-Hubbard or the Peierls scenario, i.e. by correlation or band effects, has been addressed by recent photoemission studies [105]. The observation of a V 3d giant spectral weight transfer occurring Across the MIT (see figure 2.26) has been interpreted by authors as a distinctive signature of the orbital occupation mechanism in leading the opening of the band gap.

However no clear indications of orbital ordering in VO_2 cames from experimental results. More recently, the MIT in VO_2 has been investigated using bulk sensitive hard-x-ray photoemission [106]. According to Eguchi et al. V 3d spectral weight transfer responsible for the gap formation occurs from the coherent state (the quasiparticle band) at Fermi level to the incoherent states (the lower Hubbard band), supporting a Mott-Hubbard transition picture for the first-order MIT in VO_2.

Theoretical models for VO_2

Zylbersztejn and Mott [113] proposed an electronic structure where the $d_{\|}$ band is split in a lower Hubbard band and an upper Hubbard band by the electronic Coulomb repulsion U. Since the π^* band is not split, the MIT is driven by the moving up of the π^* band due to the lattice distortion from the R to the M1 phase. This scenario, which suggests the simultaneous acting of electronic correlation and electron-lattice coupling, defies classification of the MIT in VO_2 by simple categories and suggests that no single model correctly captures all the relevant physics. Following this line, Paquet *et al.* [114] presented a band model for VO_2, which aimed at incorporating both the electron-electron interactions and the electron-lattice coupling on an equal footing. They studied the following Hamiltonian:

$$H = H_{\|} + H_{*} + H_{el-el} + H_{latt} \tag{2.3}$$

where $H_{\|}$ and H_{*} are tight binding terms describing the $d_{\|}$ and the π^* band in which the hopping integrals account for the lattice distortion; H_{el-el} describes the electron-electron interaction in the $d_{\|}$ and the π^* band and H_{latt} describes the lattice energy. Using accepted values for the electronic structure parameters, they were able to study the temperature dependence of the distortion amplitude and of the magnetic momentum, minimizing the free energy. A good agreement with experiments was obtained. In this model the metal-insulator transition is primarily driven by electron-electron correlations, and the key point is the strong renormalization of the Coulomb repulsion by the lattice distortion which rises the π^* band. On the contrary the V-V dimerization gives a small energy contribution.

The role of electronic correlation in VO_2 has been studied in a theoretical framework in which the Dinamical Mean Field Theory (DMFT) joins the LDA scheme. A multi-orbital model, to account for π^*-$d_\parallel$ overlap has been used. The Hamiltonian of the system contains intra-orbital (U) and inter-orbital ($U_{\alpha,\beta}$) Coulomb repulsion. The full Hamiltonian reads:

$$H = H_{LDA} + U \sum_{i,\alpha} n_{i\alpha} \uparrow n_{i\alpha} \downarrow + \sum_{i,\alpha,\beta,\sigma,\sigma'} U_{\alpha\beta} n_{i\alpha\sigma} n_{i\beta\sigma'} - J_H \sum_{i,\alpha,\beta} S_{i\alpha} \cdot S_{i\beta} \quad (2.4)$$

where J_H is Hund's rule interaction and

$$H_{LDA} = \sum_{k,\alpha,\beta,\sigma} \epsilon_{\alpha\beta}(k) a^\dagger_{k\alpha\sigma} a_{k,\beta,\sigma} + \sum_{i,\alpha,\sigma} \epsilon^0_{i,\alpha,\sigma} n_{i\alpha\sigma} \quad (2.5)$$

$a_{k,\beta,\sigma}$ is the annihilation operator of an electron of wavevector k with spin σ in the orbital β with energy; $n_{i,\beta,\sigma}$ is the corresponding n-operator, in the real space; $\epsilon_{\alpha\beta}(k)$ is the energy dispersion related to the α and β orbital overlap. A single-site approach correctly captures the properties of the metallic phase, but it is necessary to increase U to unphysically high values to induce an insulating phase [115]. A cluster extension of DMFT in which the dimers are taken as the key unit allowed a full description of VO_2 in good agreement with experiments [116]. In particular using U $\sim$4eV and J_H $\sim$0.7eV a nonmagnetic insulator with a $\sim$0.6 eV gap was obtained. In this theoretical scenario the physics of VO_2 is that of a renormalized Peierls insulator, where the bonding-antibonding splitting is renormalized by correlations and the MIT may therefore be labeled as an orbital-assisted collaborative Mott-Peierls transition [104].

2.3.6 High pressure studies on pure and Cr-doped VO_2

Since the theoretical description of VO_2 is still not well assessed, more experimental work, addressed to separate the role of lattice and of electron localization, is strongly required to clarify the origin of the MIT. High pressure is an ideal tool for studying the role of electronic Coulomb repulsion U in electron correlated systems. Indeed, lattice compression typically increases the orbital overlap and the electronic bandwidth (W), thus allowing for a systematic study of the physical properties of the system as a function of U/W. For this reason high pressure data are very useful for comparison with theoretical prediction.

Unfortunately there is an almost complete lack of high pressure experimental data on VO_2 apart for early resistivity measurements. Pure VO_2 (M1) shows a small pressure-induced increase of T_{IM} in the 0$-$4 GPa range [83]

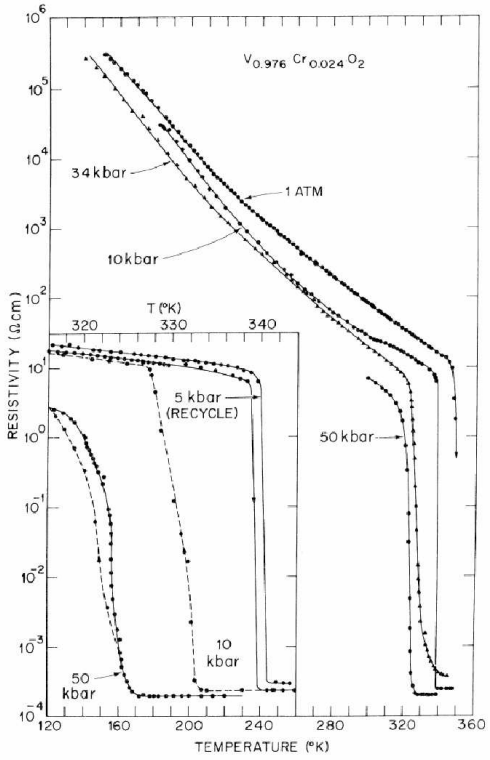

FIGURE 2.27: Temperature dependent resistivity of $V_{0.976}Cr_{0.024}O_2$ as a function of pressure from Ref. [98]

(see figure 2.28). The pressure rate $dT_{IM}/dP \sim +0.08$ K/GPa is in agreement with Clausius-Clapeiron equation because there is a volume expansion at the transition (of about 0.1%).

On the contrary 2.5% Cr-doped VO_2 in the M2 phase shows a ∼20 K decrease of T_{IM} within the 0-3 GPa range, whereas on further increasing pressure T_{IM} remains almost constant up to 5 GPa [98] (see figure 2.27 and 2.29). The negative pressure rate is not inconsistent with Clausius-Clapeiron because the volume of the M2 phase is larger than that of the M1 phase, and there is a contraction at the MIT. The discontinuity at around 3 GPa has been ascribed to a pressure induced M2 to M3 transition. On the basis of thermodynamics considerations, supported by the obervation of a slight decrease in resistivity at around 1 GPa at room temperature, the existance of a triple point at P∼2.5 GPa and T∼ 320 K has been conjectured. Therefore, a pressure induced M2 to M3 transition at room temperature is expected to occur at around 1 - 1.5 GPa. [98].

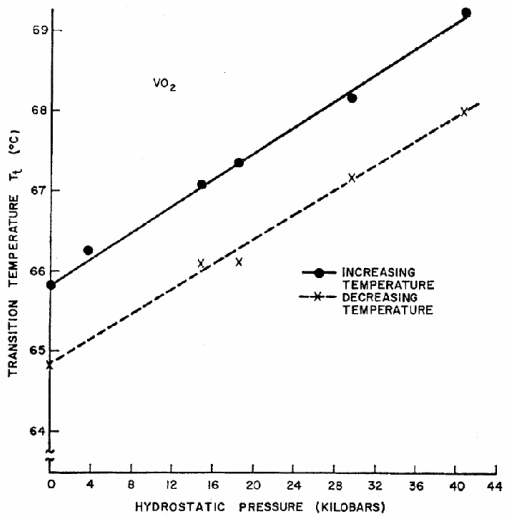

FIGURE 2.28: Insulator to metal transition temperature of VO_2 as a function of hydrostatic pressure from Ref. [83].

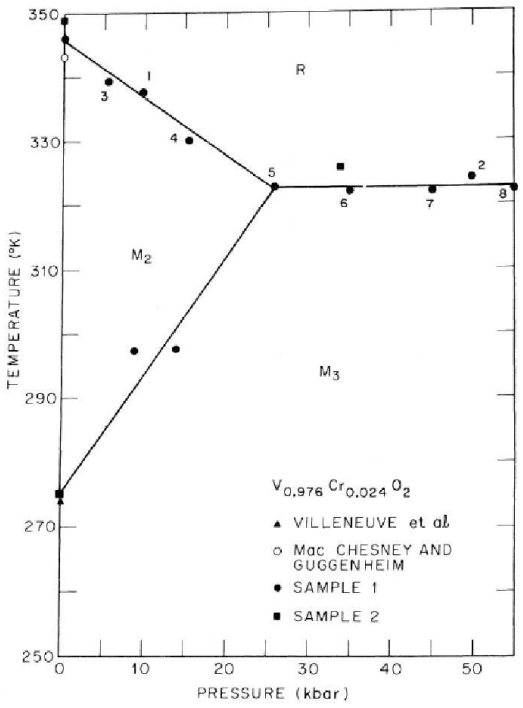

FIGURE 2.29: Tentative phase diagram of $V_{0.976}Cr_{0.024}O_2$ from Ref. [98].

2.4 Measurements plan

Raman and Infrared spectroscopy allow to independently monitor the electronic and the structural transitions, providing information on both lattice and electron dynamics. Moreover these two techniques allowed the investigation of the sample properties as a function of pressure using a diamond anvil cell, in the experimental setups that will be described in the next Chapter.

With the aim of addressing the role of electron-electron and electron-phonon interaction in leading the MIT in solid Te, $NiS_{2-x}Se_x$, and $Cr_xV_{1-x}O_2$ the following measurements have been carried out:

- Room temperature Raman and MIR spectroscopy measurements on solid Te as a function of pressure up to 15 GPa and 10 GPa respectively. Taking full advantage from the collaboration with prof. S. Scandolo (ITCP Trieste, Italy) a Density Functional Theory (DFT) study of valence electrons density has been performed with the aim of addressing pressure induced band structure modifications

- Room temperature high pressure Raman and MIR measurements on $NiS_{2-x}Se_x$ samples, in order to investigate the mechanism leading to the metallization in the pressure and Se alloying regimes. Exploiting the collaboration with Dr. G. Sangiovanni (Max-Planck Institut Stuttgart, Germany) a Dynamical Mean Field Theory (DMFT) study has been carried out to provide a qualitative understanding of the mechanism of the MIT.

- Room temperature high pressure Raman and MIR measurements on pure and Cr-doped VO_2 (with 2.5% and 0.7% Cr concentration), showing M2 and M3 monoclinic phase, in order to provide further information on the role of the different lattice distortion in leading the MIT.

Chapter 3

Experimental techniques

A brief description of the experimental techniques and the relative apparatus employed in the present work is given in this chapter. Special emphasis is placed on the diamond anvil cell for high pressure generation.

3.1 High pressure technique

Many different types of devices are available to produce high pressures. They can mainly be divided into two broad families: those based on a piston-cylinder vessel and those in which the sample is compressed between anvils. Diamond Anvil Cell (DAC) is the most largely diffused device for generating high static pressures. Compared to piston cylinder devices, the diamond anvil cell is three or four orders of magnitude less massive and generates pressure one to two orders of magnitude higher than previous devices. Pressure of several tenths of GPa can be applied and with particular technical implementations the Mbar range is reachable. Moreover, the diamond transparency to the electromagnetic radiation over a wide frequency range make this instrument a simple but powerfull tool for the spectroscopic investigation of matter under extreme condictions.

3.1.1 The high pressure diamond anvil cell

The principle of operation of the diamond anvil cell (DAC) is sketched in figure 3.1. Two opposite cone-shaped single crystal diamond anvils with small flat top faces (culets) squeeze a metallic plate, which has a small hole in the center [117] (figure 3.1). Together with the sample, a proper hydrostatic medium must be placed inside the gasket in order to avoid pressure gradients in the sample chamber, at least in the cases in which the sample is not

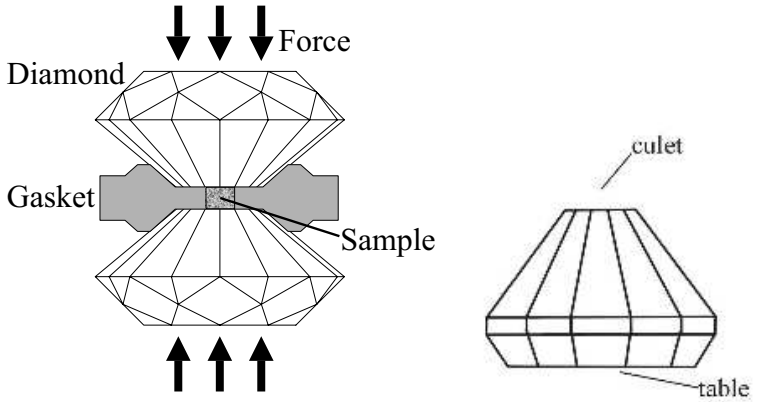

FIGURE 3.1: Schematic representation of a diamond anvil cell (DAC).

hydrostatic itself. On applying an external force of moderate intensity, a large pressure can be reached inside the hole, due to the ratio between the surface of the external and the internal anvil faces, which multiplies the external load by a large factor ($\sim 10^3$). The metallic plate acts as a gasket, containing the sample and preventing the direct anvils contact (and the consequent breakage). The friction between the diamond surfaces and the gasket results in a coercing strain toward the hole, thus compensating the internal pressure.

The accessible pressure range using a DAC depends on several factors such as the dimensions of the diamond and of the hole, and the material of the gasket.

Diamonds

Diamond is suitable for anvils due to its hardness and its trasparency to electromagnetic radiation, which makes the DAC well-adapted for spectroscopic studies, such as Raman and infrared spectroscopy and X-ray diffraction [117,118]. On the basis of impurities concentrations, diamonds are classified as Type Ia, employed in diffraction experiments, or IIa, characterized by a lower impurity level employed for both Raman and IR spectroscopy, showing a low photoluminescence and an almost flat transmittance from the far infrared to the visible region (see figure 3.2), apart from the 1900-2600 cm^{-1} region where the presence of two strong multi-phononic absorptions makes the diamonds opaque.

The diamond anvils are cut from natural, gem quality stones to have an octagonal or hexadecagonal shape, which is preferred, for they withstand the stress gradients better. The inner face (culet) has typically a 100-800 μm diameter, while the external face (table) diameter is 2-4 mm large. Diamond

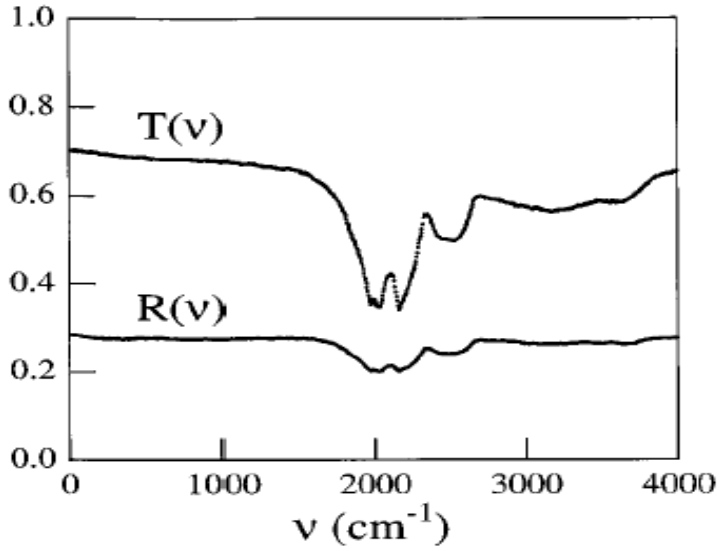

FIGURE 3.2: Type IIa diamond transmittance and reflectance in the far and mid infrared region, from Ref. [119].

thickness is about 1-3 mm. The culet must be perfectly parallel to the table in order to prevent dangerous strains. Great care must be taken in centering and aligning the two anvils to avoid premature failure of diamonds at high pressure.

Gasket

The capability of containing extremely high pressure originates from the anvil-gasket friction and its small thickness [120]. The gasket material can be either molybdenum (for measurements in 0-5 GPa range), or stainless steal (0-10 GPa), or rhenium (0-50 GPa). In order to avoid large deformation and instability of the hole, the gasket must be precompressed to a thickness only slightly greater than the final thickness, which depends on the maximum pressure that is planned to be applied. The higher the pressure the thinner the gasket and the smaller the sample volume. For example, with diamond tips of 400 μm in diameter, and a maximum pressure of 40 GPa, we have preindented the stainless steel gaskets to a thickness of about 50 μm, while with tips of 800 μm and maximum pressure of 15 GPa, the indented thickness was 50 μm. Typically a 200μm thick foil is compressed between the diamonds until about 50-100μm thickness is reached (indentation). The outflown gasket materials provides a massive support which assists the pressure containment. Moreover the diamonds imprint allows to set the gasket during the loading procedure in the same orientation as it had during indentation.

Hole

After indentation a hole is drilled in the centre of the gasket. The radius of the hole is around a third of the radius of the flat anvil culet. In the case of our 400 μm diameter culets we have drilled holes of 125 μm; 250 μm for the 800 μm diamond tips. Holes are drilled with an electro-erosion machine. After careful alignment of the preindented gasket by use of a microscope, wires of tungsten of several diameters are used to produce fine holes of the appropriate size. The wire serving as cathode, the conducting gasket as anode, electrical sparks are repeatedly produced. The erosion process lasts for a few minutes. Under working condition the cylindrical sample chamber dimensions are about 100-200 μm diameter and 50μm height.

In the next section the characteristic properties of the two different cells used in the experiments performed in the present work are summerized: the BETSA membrane DAC, employed mainly for the Raman investigations and the opposing plate DAC, employed for the mainly for infrared Reflectivity and Transmittance measurements.

The BETSA membrane DAC

The BETSA (France) membrane DAC, show in figure 3.1.1, is equipped with IIa diamonds with 800μm culets diameter. The large culet diameter allows to use a gasket with a hole diameter up to 350 μm. Using gasket made of stainless steel (AISI 316) the 0-15 GPa pressure range can be explored. The anvils are placed on two tungsten carbide basal plates, mounted on two tungsten carbide hemispheres. The anvil alignment is guaranteed by the basal plates translation and tilt. To make diamond faces parallel and centered to each others, they are delicately put in contact. The parallelism is verified looking with a microscope at the interference fringes generated illuminating with a withe light source. Fringes arise in the region where the culet are separated by a distance multiple of $\lambda/2$ and disappear when they are perfectly parallel. This technique ensures parallelism with an error of the order of 10^{-3} rad. The mechanical stability of the piston-cylinder matching of the two block of the cell guarantees the conservation of the alignment during the use. The basal plates and the alignment system have optical access in form of cones. The optical aperture is 45 degree. Force is applied using a metallic membrane, screwed to the body (cylinder) of the cell. On increasing the helium pressure into the membrane by means of a capillary, the piston sliding within the cylinder pushes the upper anvil against the bottom one.

FIGURE 3.3: Sketch of the piston-cylinder BETSA DAC.

D'anvils opposing plates DAC

The opposing plates DAC producted by D'Anvils (Israel) is a compact and simple screw driven pressure cell. Its reduced dimensions (diameter $\sim$ 25 mm, height $\sim$ 12 mm in working conditions) make this cell very suitable for using in a microscopy setup. This DAC is equipped with IIa diamonds, with 400μm culet diameters. Using a stainless steel (AISI 316) gasket with a 150μm hole diameter pressure up to 30 GPa can be reached. A sketch of the cell is reported in figure 3.4.

Diamond anvils (5 in Fig 3.4) are fixed with glue to tungsten carbide backing plates (3 and 6), with a 1.2 mm hole diameter and 60° angular opening. The upper backing plate is inserted in a tight way in the steel platen (2) and three lateral adjustment screws in the lower platen (8) allow to obtain the mutual centering of the culets. Two pins (7) assure the maintenance of the centering and help in mounting the gasket (4). Pressure is achieved by gentle tightening the tension screws (1). Since the cell mechanism does not pin down the tilting of the platen during compression, it is important to follow a careful procedure during pressurizing. Before any operation such indenting or pressurizing the two anvils must be put in contact. Parallelism is achieved by gently tightening the tension screws till the disappearance of the Newton interference rings. The cell thickness (i.e. the distance between the two platens) is then measured at three reference points at the platen cir-

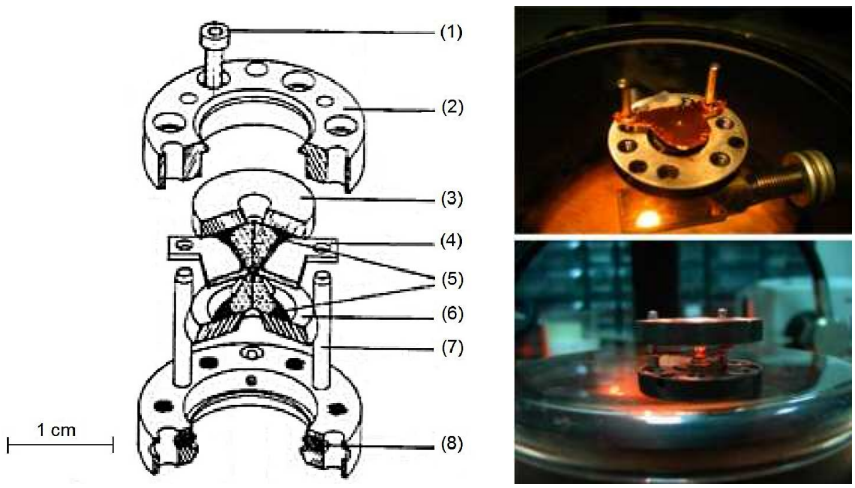

FIGURE 3.4: Sketch of the D'anvils opposing-plate cell. Diamonds anvils (5) are glued to the basal plates (3 and 6), mounted on two steel platens (2 and 8). (4) gasket; (7) steel pins (7); (1) tension screw.

cumference, 120° apart. During indenting or pressurizing, the cell thickness must be measured at the same three points. Keeping flat within 5 μm the difference between the reference and the actual cell thickness at the three points ensures the preserving of parallelism within 10^{-3} rad.

3.1.2 In situ pressure measurement

Sample pressure in the DAC is evaluated putting a pressure gauge in the gasket hole next to the sample. This gauge can be a crystal of well-known equation of state, but a faster and more convenient method is to follow the pressure shift of fluorescence lines of a luminescent compound. The most commonly used gauge is ruby, adopted also in this thesis for pressure determination. Ruby (Al_2O_3 with Cr^{+3} impurities) shows two sharp and intense fluorescence lines R_1 and R_2 at 692.7 nm and 694.25 nm, respectively, at ambient temperature and pressure conditions (Figure 3.5).

R_1 and R_2 lines exhibit a strong dependence on the interatomic distances and thus on pressure, showing a shift toward longer wavelength. Owing to the strong intensities of the signal, very small ruby sphere ($\sim 5\mu$m) can be used loaded in the DAC together with the sample and used as pressure gauge. Ruby fluorescence is typically excited by a laser (both He-Ne or argon ion lasers are proper to use) and analyzed by a monochromator. The pressure calibration is typically performed by means of the more intense R2 line whose pressure dependence was established and improved during the years by extrapolating state-equations and non hydrostatic data from shock-

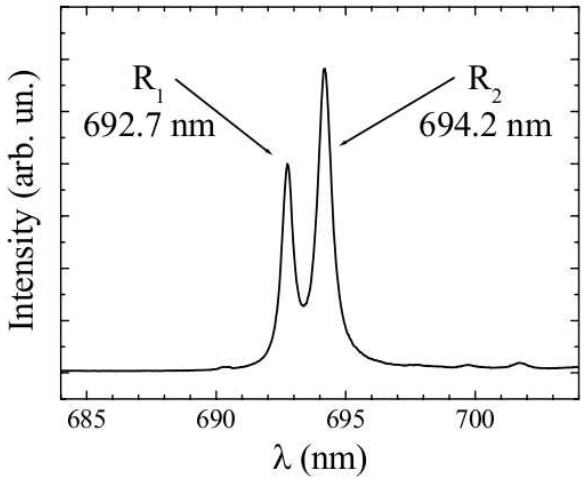

FIGURE 3.5: R_1 and R_2 fluorescence lines of ruby (Al_2O_3 with Cr^{+3} impurities) at ambient pressure.

wave experiments [122, 123]. The room temperature calibration is reported in figure 3.6 from Ref. [123]. In the 0-30 GPa range the linear extrapolation

$$P = \alpha \Delta \lambda \tag{3.1}$$

with $\alpha = 2.74 GPa/nm$ ca be adopted (see dashed line in figure 3.6). In prefect hydrostatic conditions the ruby fluorescence technique ensure pressure indetermination of $\pm$ 0.1 GPa in the 0-10 GPa range and $\pm$ 0.5 GPa for pressure up to 30 GPa. However pressure gradients on the sample may be larger, depending on the pressure transmitting medium used. In the experiments presented in this work, pressure errors has been overestimated, proportionally to the R_1 line width.

3.2 Raman scattering setup

Raman spectroscopy is a useful technique in order to obtain information about lattice dynamic, and about the modifications of the phonon spectrum induced by doping, pressure, or temperature. As mentioned above, diamonds are very suitable for this type of spectroscopy owing to their large transparency in the visible light region. The only disadvantage is the presence of the strong one-phonon Raman contribution at around 1300 cm^{-1} which prevents the spectrum reliability in the 1200-1500 cm^{-1} range.

In this work, Raman spectra have been collected in back-scattering geometry by means of a commercial LABRAM Infinity micro-spectrometer by

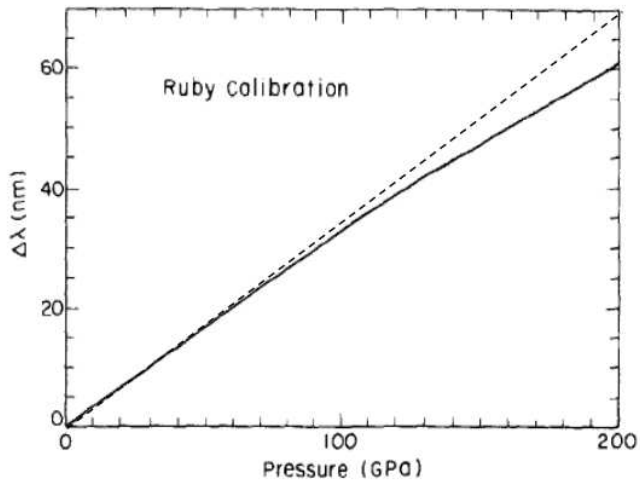

FIGURE 3.6: Room temperature pressure calibration of the shift of the R_2 ruby fluorescence line [123]. Dashed line is the linear extrapolation in the 0-30 GPa range.

Jobin Yvon equipped with an adjustable optical notch filter, an optical microscope and a cooled low noise multichannel charge coupled device (CCD) detector (1024 X 256 pixel). A 16mW He-Ne laser (λ=632.8 nm) has been used. If necessary, the incident power can be attenuated by filters placed in a filter wheel. The laser beam is reflected by the notch filter toward the microscope. Optical objectives with 10x to 50x magnifications can be used to focus the beam onto the sample and collect the backscattered light. The latter is sent again to the notch-filter, which in transmission rejects the elastically scattered light from sample and optics (see figure 3.7). The low frequency cutoff within this setup is at about 100 cm^{-1}. Before entering the monochromator, the light is focused into an adjustable pinhole confocal with the sample, in order to reduce the scattering volume along the optical axis. The monocromator is equipped with two gratings (600 and 1800 lines/mm), that can be remotely rotated in order to select the spectral range. Photons are detected by a CCD device and analyzed by a computer. Frequency calibration is performed using the known emission lines from a Ne lamp.

The backscattering geometry does not allow to collect spectra at very low Raman shift. However this setup has the great advantage that a confocal microscope can be used, thus allowing to easily collect Raman spectra from very small samples. The laser spot diameter is about 5 μm using the 20x objective and about 2 μm using the 50x. The pinhole aperture can be adjusted so to obtain a scattering volume of only a few μm across. Moreover

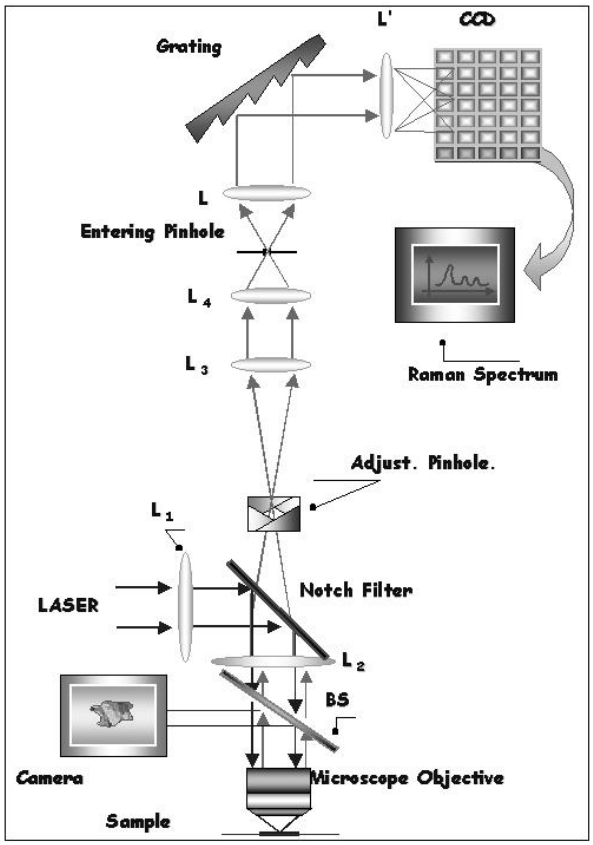

FIGURE 3.7: Optical scheme of the micro-Raman spectrometer employed in the present work.

focusing and aligning can be set by means of a camera. These characteristic of the Raman setup allow measurements as a function of pressure using a DAC.

Both the BETSA and the D'Anvils DACs described in section 3.1.1 were employed for Raman measurements. A 22 mm focal length 20x objective was used in order to fit the angular aperture and the working distance of the cells. The pinhole aperture was adjusted in order to reduced the diamond fluorescence background contribution. 1800 lines/mm grating was used, obtaining a resolution of about 3 cm^{-1}. Stainless steel gasket with about 250 μm (BETSA) and 150μm (D'Anvils) diameter holes were used respectively. The sample, in form of finely milled powder or of a small single crystal, was placed on top of a pre-sintered NaCl pellet into the gasket hole. This procedure ensures good hydrostatic conditions and the high thermal conductivity of diamond prevents strong heating of the sample impinged by the laser spot.

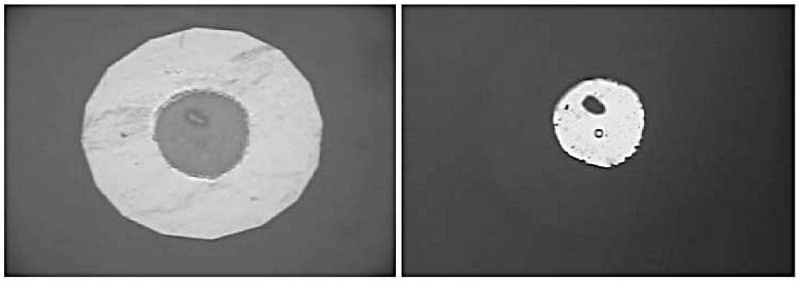

FIGURE 3.8: A small VO_2 crystal loaded in the gasket hole with ruby chips into a NaCl pellet for high pressure Raman measurements. Culet diameter is 400 μm. The picture has been taken in reflection, on the left, and transmission configuration, on the right.

A small ruby chip was also placed inside the gasket hole for pressure determination. Ruby fluorescence was directly measured by means of the Raman spectrometer. In figure 3.8 a picture of a sample loaded in the gasket hole is shown.

3.3 Infrared setup

Infrared spectroscopy is a suitable investigation technique for studying charge delocalization processes, providing information on the low frequency electron dynamics. Moreover the possibility to probe the sample in a DAC both reflection and transmission configuration makes this technique very powerful to study pressure dependence of the transport properties of the systems. Transmittance measurements provide directly information on absorption band, allowing for a simple analysis. The limit of this technique originates by the saturation of spectra in dealing with high absorbent samples. On the contrary high pressure reflectivity measurements can be also performed on strongly absorbent samples. A data collection on a wide frequency range allows to extract the optical conductivity via the Kramers-Kroenig (KK) analysis. Moreover the standard analysis must be corrected to account for the diamond-sample interface. However no conventional sources have been used in those experiments because of the high brilliance required due to the small dimensions of samples. The use of synchrotron radiation is then required and the fact that it is a broad band source allows to measure in each spectral range only by changing the beam-splitters.

High pressure infrared measurements presented in this work have been carried out at the IR beamline SISSI (*Source for Imaging and Spectroscopic Studies in the Infrared*) of the synchrotron laboratory ELETTRA in Trieste,

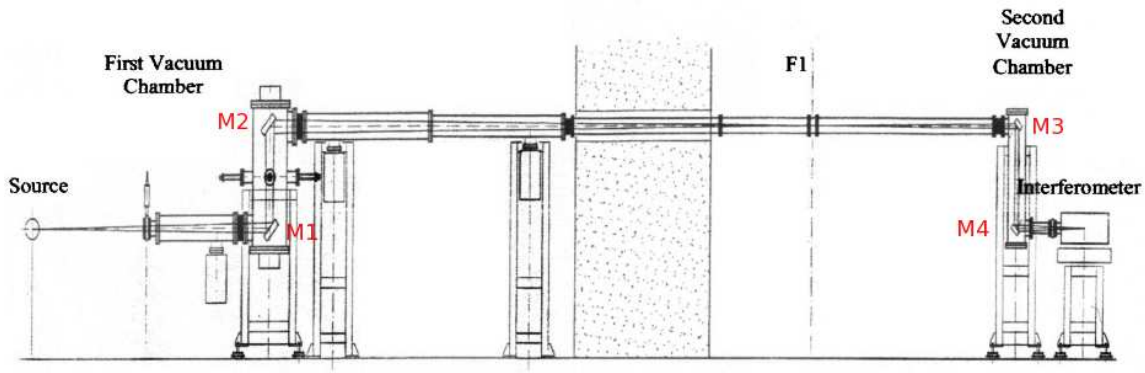

FIGURE 3.9: The layout of the SISSI (Source for Imaging and Spectroscopic Studies in the Infrared) beamline at ELETTRA

Italy [124]. This infrared source provides high brilliance from the far infrared to the visible frequency region. As shown in figure 3.9 the radiation is collected from bending magnet and enters the first vacuum chamber, which hosts the plane extraction mirror M1 and the ellipsoid mirror M2 which focuses the radiation beyond the shielding wall of the synchrotron hall in the intermediate focal point F1. The second vacuum chamber hosts the third M3 (plane) and fourth M4 (ellipsoidal) mirrors, in a symmetric optical configuration with respect to M1 and M2. This optical design permits the aberrations by the transfer optics due to the wide emission angle to be minimised. M4 focuses the infrared radiaton on the diamond window (point F2), which is the last UHV component of the first branch. The experimental station consists of a Bruker IFS-66v Michelson interferometer coupled to a Bruker Hyperion-2000 cassegrainian infrared microscope equipped with a 15x objectives, a nitrogen cooled MCT detector and a Mylar (or a KBr) beam splitter (BS). Within this setup the 300-8000 cm^{-1} frequency range can be explored.

The screw clamped D'Anvil cell described in section 3.1.1 has been used, in order to fit the vertical acceptance of the IR microscope. NaCl and KBr cubic salt were both used as pressure transmitting medium. As for the FIR transmission measurements, the samples were finely milled and pressed between the diamond anvils in order to obtain a compact and thin sample slab with well defined thickness ranging between 2 and 5 μm. Eventually this procedure ensures sharp surfaces, that are important also for reflectivity measurements, where the quality and the number of interfaces are critical parameters.

The sample slab was carefully shaped for fitting inside the gasket hole and then placed on top of a pre-sintered NaCl (KBr) pellet, together with a ruby chip. The present loading procedure enables the sample slab to main-

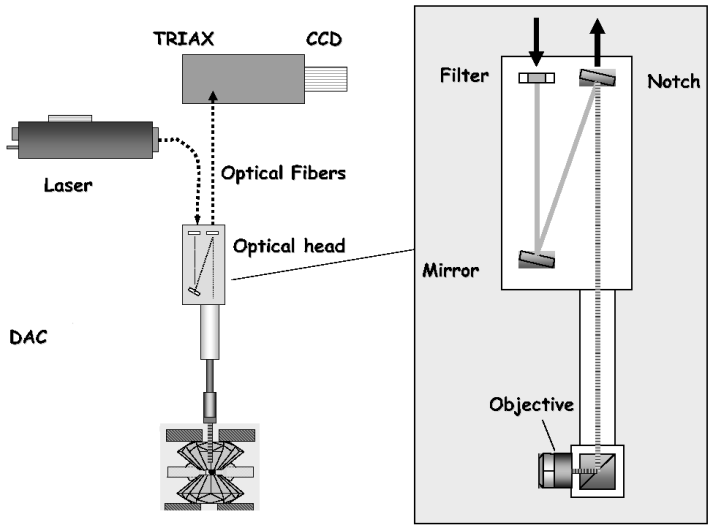

FIGURE 3.10: Scheme of the optical head employed for the ruby fluorescence measurements at SISSI.

tain a direct contact with the diamond surface on the side where reflectivity spectra are collected and ensures a net interface. Moreover this simple multi-layer structure (diamond/sample/pressure medium/diamond), assures a rather easy theoretical modeling of trasmittance and reflectivity spectra, thus allowing the calculation of the optical conductivity by means of a local analysis, instead required the non-local KK analysis (see appendix B).

The measuring procedure is the following: the DAC is mounted over a home built holder that ensure to place the DAC always in the same position. This holder is fixed to the microscope sample stage that allows to finely align the DAC. Adjustable apertures mounted in the microscope are then fixed so to collect only the signal from the sample placed inside the DAC. The apertures are kept the same for all the experimental run. Moreover, mirrors that couple the microscope and interferometer are aligned so to couple the focus of the IR radiation to the visible focus of the white light of the microscope, so to be sure that aligning by eye the DAC, exactly the sample signal is then detected. The focus has to be kept fixed for all the experimental run.

Ruby fluorescence was measured by means of a spectrometer composed by a TRIAX monochromator (by Jobin Yvon) equipped with a 1800 lines/mm grating and a CCD detector whose output signal is analyzed by a dedicated computer. Resolution was about 3 cm^{-1}. An optical head represented in figure 3.10 was used to focus the 514 nm line of a 100 mW Ar ion laser into the DAC and to collect the backscattered signal without removing the DAC from the sample compartment. The laser is sent to the objective via optical

fiber. The ruby fluorescence collected by the objective is sent by a notch beam-splitter to the outgoing fiber which is coupled to the spectrometer.

Measurements are taken first in the mid-IR then the BS is changed and the near-IR and the visible are measured. In each spectral range IR data are collected over the sample and also some reference spectra are acquired.

At the end of the each pressure run we measured the light intensities reflected by a gold mirror placed between the diamonds $I_R^{Au}(\omega)$ and by the external face $I_R^{D'}(\omega)$ of the diamond anvil. By using the ratio $I_R^{D'}(\omega)/I_R^{D}(\omega)$ as a correction function, we achieved the reflectivity $R(\omega)$:

$$R(\omega) = \frac{I_R^S(\omega)}{I_R^{Au}(\omega)} \cdot \frac{I_R^{D'}(\omega)}{I_R^D(\omega)} \tag{3.2}$$

The transmittance $T(\omega)$ is obtained using:

$$T(\omega) = \frac{I_T^S(\omega)}{I_T^{DAC}(\omega)} \cdot \frac{I_R^{D'}(\omega)}{I_R^D(\omega)} \tag{3.3}$$

where $I_T^{DAC}(\omega)$ is the transmitted intensity of the empty DAC without gasket and with the anvils in tight contact.

Chapter 4

High pressure measurements on solid Te

The group VI elements (S, Se, Te...) exhibit very interesting features under pressure, undergoing successive structural phase transitions and becoming metallic as a consequence of the lattice compression. Optical spectroscopy has proved to be an important tools in the determination of the crystal and electronic structure more appropriate to these systems. Indeed infrared spectroscopy allows to study the low energy electron transitions, making possible to establish the width of the forbidden energy gap, Raman scattering, probing the lattice dynamics, is very suitable to address the lattice structure, in such cases better than X ray diffraction. Coupled with high pressure, these two spectroscopic techniques provide useful information on the mechanisms responsible for the electronic and structural transitions induced by the volume reduction. Although physical properties of solid Te have been largely investigated, to the best of our knowledge, there is a significative lack of high pressure optical data on the system.

In this chapter a survey of optical measurements on solid Te is given, followed by the discussion of high pressure Raman measurements on the system carried out within this Ph.D thesis. The analysis of high pressure reflectivity data recently acquired at the IR Beamline Sissi of Elettra synchrotron is also presented. In the last section a Density Functional Theory study of the valence electron bands within pseudo-potential approximations is reported.

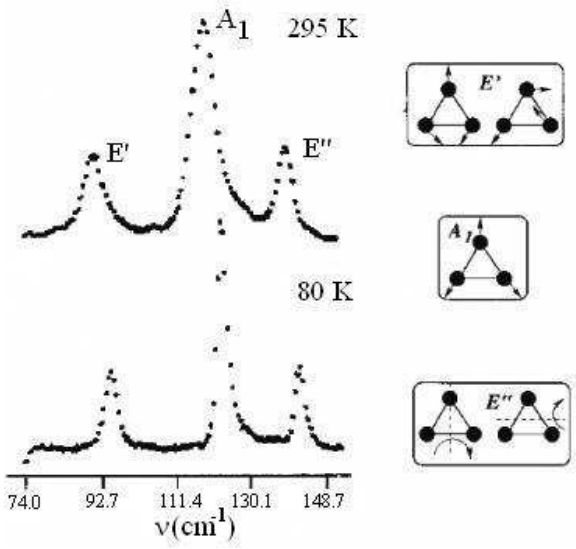

FIGURE 4.1: Raman spectra of solid Te at 295 K (a) and at 90 K (b) respectively [127]

.

4.1 Optical studies on solid Te

4.1.1 Survey of Raman measurements on solid Te

According to group theory, trigonal Te (space group D_3^4) has five Raman active modes ($A_1 + 2E$) and only one infrared active mode (A_2). Following Ref. [126], among Raman active modes, the two doubly degenerated symmetry modes E' and E" and the A_1 symmetry mode, identified at ambient pressure at 90, 140, 120 cm^{-1} respectively, correspond to rotational and asymmetric and symmetric breathing of Te atoms in the plane perpendicular to the helical c axis. A schematic representation of eigenvectors of each specific phonon mode taken along the c axis is shown in figure 4.1.

Raman spectra of solid Te collected at selected temperature are shown in figure 4.1. The comparison between the two spectra illustrates the thermal anharmonic effects on the shift and width of the modes [127].

On increasing pressure on trigonal Te, the b axis contracts greatly with respect the a and c axes [36]. As a consequence, a denser packing of chains and a progressive reduction of the Peierls distortion are achieved with pressure, leading to an increase of interchain interactions and giving rise to a transfer of electronic charge from covalent bonding to to inter-chain bonding. The changes in the bonding state and atomic distances of trigonal Te obviously influence the lattice dynamics.

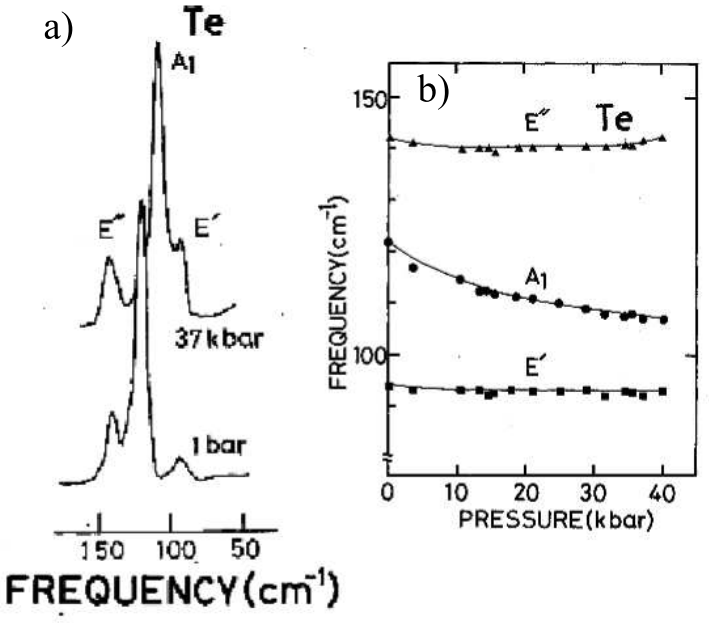

FIGURE 4.2: (a) Room temperature Raman spectra of solid Te as function of pressure; (b) Pressure dependence of Te Raman active modes. After ref. [36]

.

Raman spectra of solid Te at selected pressure and phonon frequencies pressure dependence are shown in panel a) and panel b) of figure 4.2, respectively. Variations of the relative intensities of phonon peaks must be ascribed to polarization effect, particularly strong in crystalline Te. The main effect of the pressure results in an almost linear softening of the chain expansion type A_1 mode, as a consequence of the lattice symmetrization which induces the strengthening and weakening of inter- and intra-chain bounds [36, 41]. A weakly increase of the two E phonon frequencies is observed in the same pressure range.

4.1.2 Survey of Infrared measurements on solid Te

The electronic properties of solid Te have undergone an intensive investigation in last years. Due to the spiral chain structure, Te atoms experience different bonding strengths along different spacial directions (i.e. parallel and perpendicular to the screw c axis). The anisotropic character of the crystal structure reflects on the magnitudes of the optical response of the system. The temperature and the polarization dependences between 300 and 10 K of the absorption edge of single-crystal Te have been studied only long time ago by Tutihasi et al. [128] in order to elucidate energy band configuration

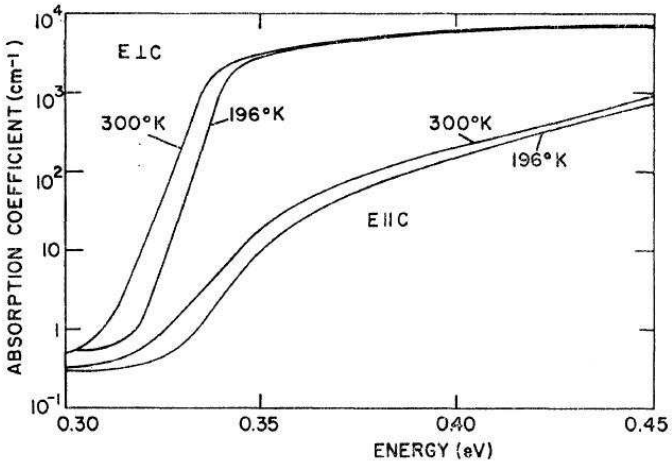

FIGURE 4.3: Trigonal Te absorption edge curves at selected temperatures as function of incident light polarization (parallel and perpendicular to the c axis respectively) [128].

.

and, as a consequence, the nature of the transitions involved at the band-edge. The dichroism of the optical absorption edge of solid Te is well evident from figure 4.3, which illustrates the absorption coefficient as a function of energy [128]. As well evident from the spectra, a strong depletion is observed in the low frequency region, due to the opening of the insulating gap evaluated at about 0.33 and 0.35 eV, depending on the light polarization. These values are consistent with early resistivity measurements [33].

Panel a) of figure 4.4 shows the pressure variation up to 96 kbar of the reflectivity spectra (shifted upwards by 0.1 one with respect the other) of powdered polycrystalline Te [129]. The reflectivity at 1 kbar is relatively small (about 0.1) in the near-infrared region, rises near 1.3 eV with increasing photon energy and has a broad peak around 3.0 eV, which corresponds to a semiconductor-like spectrum. At 38 kbar just below the transition to the metallic state the reflectivity becomes larger over the entire energy region. The broad peak in the visible region shifts to lower energy. At the transition to the metallic state a further increase of the reflectivity is observed in the near-infrared and visible region. On increasing the pressure above to 50 kbar two peaks around 1.0 and 2.0 eV appear while in the near-infrared region the reflectivity remarkably increases becoming larger than that in the visible region. On further increasing the pressure Te shows a metallic behaviour.

The optical conductivity curves $\sigma(\omega)$ derived from the reflectivity spectra at each working pressure are shown in panel b) of figure 4.4. It should be

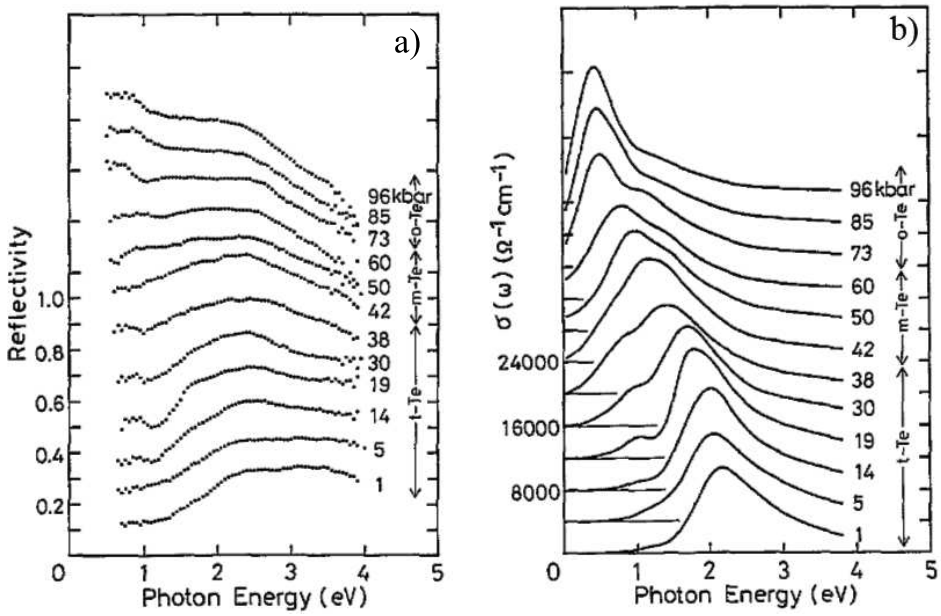

FIGURE 4.4: Pressure induced modification in room temperature a) reflectivity spectra and b) derived optical conductivity of solid polycrystalline Te [129].

.

noted that the zero lies of the ordinate are shifted by 4000 Ω^{-1} cm^{-1} for each different pressure. The optical conductivity at 1 kbar indicates semiconducting behaviour with an optical gap and two main peaks at 2.2 eV and 1.2 eV. Bearing in mind that the highest valence band is constituted by two of the four 5p electrons which are in non-bonding lone-pair (LP) orbitals and the lower conduction band is formed by anti-bonding orbitals ($\sigma^\star$) between neighbouring chains, these two spectral features have been ascribed to the LP to $\sigma^\star$ optical transitions. On increasing the pressure up to 38 kbar the main peak and the shoulder shift to low energy and grow, while the optical gap becomes narrow and progressively approaches to zero at the transition point. The frequency shift and the enhancement of the two peaks as well as the closing of the gap can be understood taking into account the increase of interchain interaction and the weakening of covalent bonds within the chain.In addition, the authors claim the appearance of a Drude term as a signature of the metallic state.

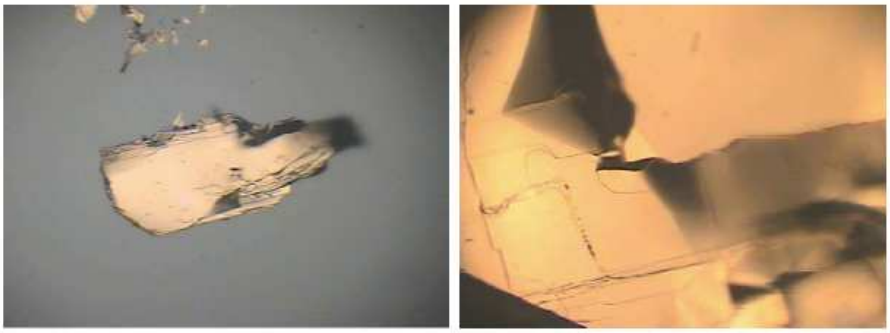

FIGURE 4.5: Images of a small piece of commercial solid Te by Aldrich visualized through the camera.

4.2 Synthesis and characterization on solid Te

Commercial solid Te by Aldrich with 99.999 % purity is employed for both Raman and Infrared spectroscopic investigation (see figure 4.5). The trigonal structure is readily revealed in Te by cleaving a crystal since the relatively weak binding between chains generates planes of easy cleavage parallel to the c axis. High pressure measurements have been preceded by a detailed room temperature Raman characterization of the samples. A room temperature Raman spectrum of Te is shown in Fig. 4.6. All the three main structures predicted by group theory for the trigonal phase are clearly observed.

Measured spectra were fitted by using a standard model curve given by the sum of electronic and phononic contributions:

$$\big(1+n(\omega)\big)\left[\frac{B\omega\gamma}{\omega^2+\gamma^2}+\sum_{i=1}^{N} Ph(\omega;\omega_i,\Gamma_i,A_i)\right] \tag{4.1}$$

The parameters B and γ characterize the electronic response, ω_i, Γ_i, and A_i are the frequency, linewidth, and intensity of the i-*th* phonon peak, respectively. The quantity $\big(1+n(\omega)\big)$ accounts for the Bose-Einstein statistics. Damped harmonic oscillators have been employed to describe phonon excitations [132]:

$$Ph(\omega;\omega_i,\Gamma_i,A_i) \rightarrow \frac{A_i\Gamma_i^2\omega_i\omega}{(\omega_i^2-\omega^2)^2+\Gamma_i^2\omega^2} \tag{4.2}$$

In order to account for the background in the Raman spectra, a linear baseline has been included in the fitting curve. Best fitting curve is drawn in solid line in figure 4.6.

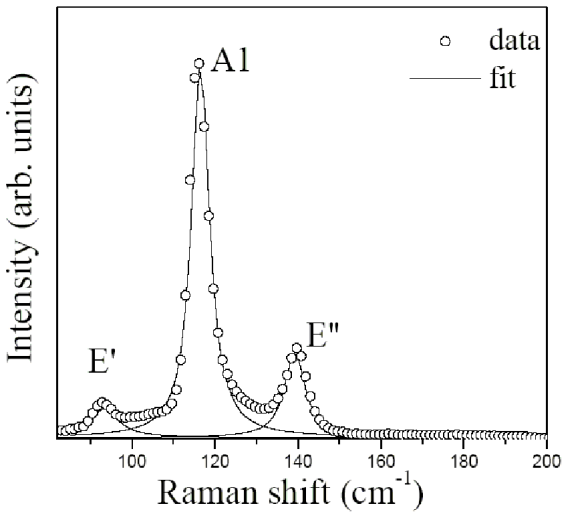

FIGURE 4.6: Room temperature Raman spectrum of solid Te from ours samples and best fit curve (solid line) from equation 4.1.

4.3 Solid Te at high pressure

Raman and Infrared measurements under high-pressures are very suitable to determine both lattice and electron dynamics properties of a system. In order to investigate the role of the electron-electron and the electron-phonon interaction in driving the electronic and structural transitions, Raman and infrared (MIR) spectroscopy measurements as a function of pressure, up to 15 GPa and 10 GPa respectively, have been carried out on room temperature Te.

4.3.1 High pressure Raman measurements on Te

High pressure Raman measurements have been performed on small Te polycrystalline samples ($\approx$ 50x10x10μm^3) using the apparatus described in 3.2 section. The samples have been loaded in the screw clamped DAC together with a ruby cheap and ethanol methanol 4:1 mixture and NaCl as hydrostatic media (see 3.1 section). A maximum pressure of 11 and 15 GPa has been reached, respectively.

Room temperature Raman spectra of Te samples using ethanol-methanol mixture (panel a) and using NaCl (panel b) as hydrostatic media are shown in figure 4.7 at selected pressure. The effect of pressure on Te Raman spectrum appears complex, although, on increasing pressure Raman spectra do not significantly change their peak pattern and their general spectral shape. This general pressure behavior and in particular the persistence of the Ra-

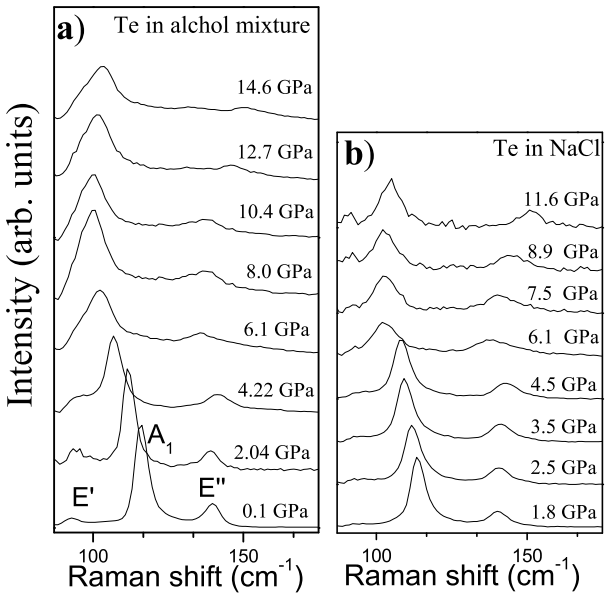

FIGURE 4.7: Room temperature Raman spectra of Te using ethanol methanol 4:1 mixture (a), and NaCl (b) at selected pressure. Background obtained by the fitting procedure has been subtracted for clarity.

man spectrum above 11 GPa is specially important in addressing the real sequence of structural phases followed by Te on increasing the pressure. As matter of fact, the old transition scheme [36–38] predicts the absence of Raman response in this pressure regime. Nevertheless the occurrence of an incommensurate lattice modulation leads to extra Raman active modes ($3A_g + 3B_g$), estimable within the sinusoidal approximation of superspace group theory [130, 131]. Therefore the presence of Raman signal in this pressure range is consistent with the presence of the incommensurate modulation [30, 39] and incompatible with previous high pressure scenario.

Looking at figure 4.7, between $0 - 4$ GPa an almost regular hardening of the phonon frequencies of the two E modes has been observed, while the A_1 mode shows a clear softening of the phonon frequencies down to low energy side. Increasing pressure up to 8 Gpa also the E" mode seem to soft towards low frequency side like the A_1 mode, wile above this pressure value A_1 mode to be constant while the E" mode show a clear hardening of its frequency value. We notice that the degeneracy of the E modes is not removed by pressure at least over the explored range.

These findings are quantitatively confirmed by the results obtained ap-

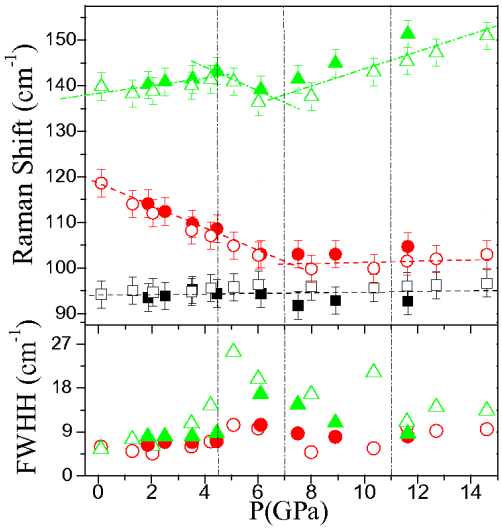

FIGURE 4.8: Pressure dependence of phonon frequencies (upper panel) and of phonon widths (lower panel) of Te. Open (close) symbols refer to measurements performed using ethanol-methanol mixture (NaCl) as hydrostatic medium.

plying the fitting procedure described above. The pressure dependence of the phonon frequencies is shown in the upper panel of figure 4.8. On applying pressure up to 4 GPa the A_1 mode shows a softening of about 10 cm^{-1}, while the phonon frequencies of the two E modes weakly increase. It is well known from X-ray diffraction measurements [36] that, as consequence of the lattice compression, the *b* axis contracts with increasing pressure, while the changes of the c axis and the a axis are rather small [36]. Since the A_1 mode corresponds to the symmetric intrachain dilation and compression in the *ab* plane while the E' mode corresponds to rigid-chain rotation which affects interchain bonds, the pressure dependence of Raman spectrum is consistent with a progressive weakening of intrachain bonds at expenses of the interchain atomic interactions. The spectroscopic signature of the metallization process at $\sim$ 4 GPa can be found in the progressive increasing of the electronic contribution observed in the Raman spectra (not shown here). On further increasing the pressure between 4 and 7 GPa a softening of E" mode takes place. This softening can result from the pressure induced transition Te-I to Te-II at 4 GPa. Finaly a rather abrupt change of the slope in the same phonon frequency occurs at $\sim$ 7 Gpa (see figure 4.8) probably due to the disappearance of Te-II phase, which is completely removed at 7.5 GPa according to the new transition scheme [30, 39].

It should be noted that the onset of several phase transitions can be also

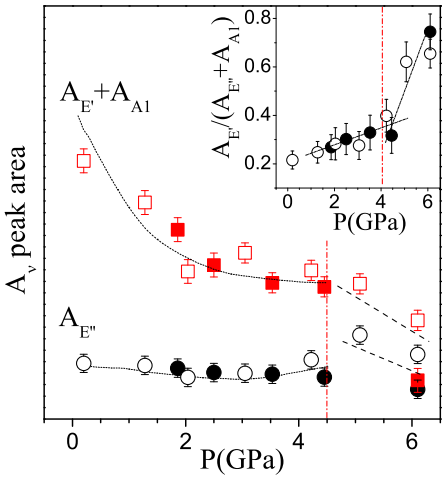

FIGURE 4.9: Phonon integrated areas of E" mode (black circles) and of the E' mode plus A_1 mode (red squares). Dotted line are guides for eyes. Inset: integrated areas ratio as function of pressure. Open and full symbols are referred to pressure measurements using ethanol-methanol mixture and NaCl as hydrostatic medium respectively.

evinced in the pressure dependence of the phonon widths of A_1 mode and the E" mode, shown in the lower panel of figure 4.8. As is evident, the widths of the two Raman peaks show clear discontinuities which mark two critical pressures that correspond to TeI $\rightarrow$ TeII transition (4 GPa) and the complete removal of Te-II phase (8 GPa).

On further increasing the pressure, the E" mode shows a significant hardening while the A_1 mode seems to remain almost constant over the whole explored pressure range (see figure 4.8). No phonon anomalies in Raman spectra are detected at 11 GPa. Since the A_1 mode is mainly an intrachain mode and the E mode involves the motions of atoms in different chains, this features suggest a possible charge transfer process activated by lattice compression between different chains. This scenario is confirmed by a systematic study of Raman peak integrated areas, reported in figure 4.9. On increasing pressure a general reduction of Raman spectra signal is observed for all the phonon modes, although more evident for the A_1 mode then for the E modes. Since a comparison among the absolute areas between different spectra may be questionable, an analysis of peak areas ratios has been performed for each spectrum. The pressure dependence of the areas ratio $(E")\ /(A_1 + E')$ in the pressure range 0 - 6 GPa is shown in the inset of figure 4.9. Two different regimes below and above the threshold pressure value of 4 GPa, where the MIT takes place, are clearly identifiable. On increasing pressure up to

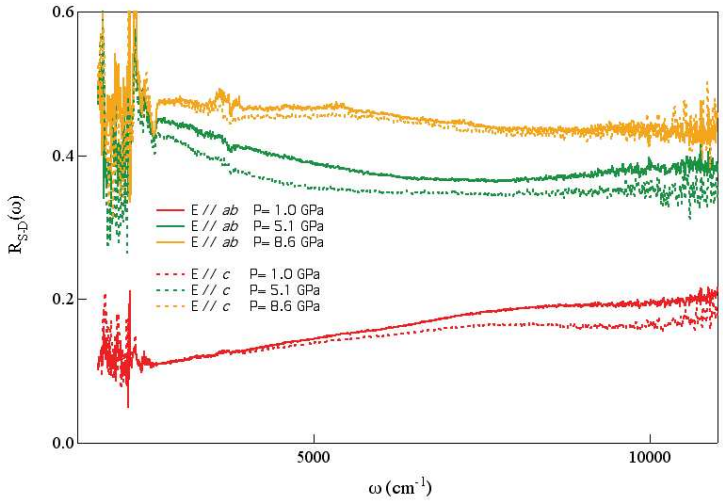

FIGURE 4.10: Room temperature single crystal Te reflectivity curves as function of the light polarization at selected pressure.

6 GPa, since the two phonon areas are progressively smaller, their comparison became less reliable.

4.3.2 High pressure infrared measurements on Te

In order to understand the role of lattice symmetrization in the metallization process occurring in solid Te, high pressure infrared reflectivity measurements have been recently performed (July 2009) at the infrared beamline Sissi of Electra synchrotron in Trieste. Great care has been taken in the choice of the sample and in the determination of the proper orientation of the crystal loaded in the DAC. The Infrared setup described in 3.3 section has been employed for the present measurements. For radiation polarized parallel and perpendicular to the c axis of the crystal the result are shown in figure 4.10 at selected pressure. Although the data analysis is still incomplete, we can safely ascribe the progressive increase of the reflectivity curves for both the directions of light polarization to the metallization process, setting in the system as the pressure is raised above 4 GPa.

Starting from reflectivity data, one can obtain via the Kramers-Krönig transformations the real part of the electrical conductivity, which provides information about carrier dynamics of the system. The optical conductivity obtained from a preliminary data analysis is show in figure 4.11. It is rather apparent that the spectra collected in a perpendicular geometry show a faster band gap closure than those collected with a parallel geometry. On these bases it seems that an unexpected increase of the electronic anisotropy occurs

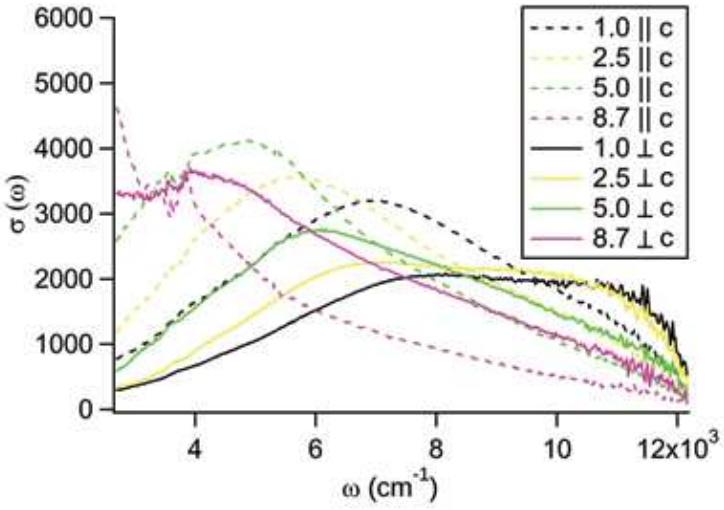

FIGURE 4.11: Frequency dependent optical conductivity of single crystal Te as function of the light polarization at selected pressure

on increasing the pressure. This would be an important result which, if confirmed by a more accurate data analysis, will deserve further theoretical and experimental investigations.

4.3.3 High pressure DFT calculations on trigonal Te

In order to investigate the behavior of Te valence electron charge density ($5S^2$ $5P^4$) a Pseudopotential Density Functional Theory calculation is employed using the Quantum-Espresso code [133]. This research activity has been carried out within a close collaboration with Prof. S. Scandolo (ICTP Trieste), one of co-authors of the code and Dr. D. Chermisi, a Ph.D. student of the group of prof. P. Postorino. A full structural relaxation under the influence of Hellmann-Feynman forces and stresses is performed until no force component exceeded 0.004 eV / $\mathring{A}$ for several target pressures using the variable cell shape method. For each relaxed cell electronic bands and electronic density of states was computed in order to study the gap closures as function of pressure. Moreover the normal mode at each pressure using both the small displacement method and the Density Functional Perturbation Theory was obtained. The structural results obtained at ambient pressure are in good agreement with experimental ones even if the intrachain bond lengths are overestimate by about 10%. This means that the reduction of the overall anisotropy of the cohesive forces, due to the approximation of the exchange-correlation energy, does not affect the response of the unit cell parameters to

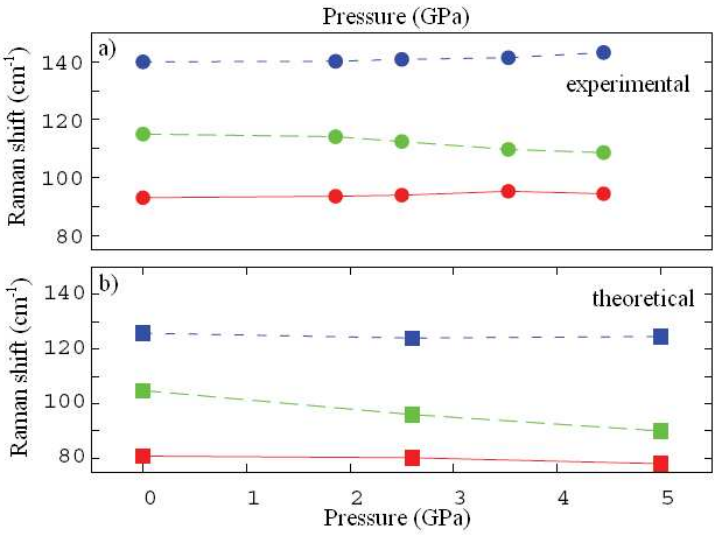

FIGURE 4.12: Comparison between room temperature experimental (a) and theoretical (b) phonon frequencies as function of pressure

compression, while leads to a slight overestimation of the sensitivity of the intrachain distance to pressure. This is reflected in an underestimation of the phonon frequencies, more significant for the intrachain mode. However, the calculated phonon frequencies show the same pressure dependence as the experimental ones, including the clear softening of intra-chain A_1 mode due to inter-chain charge transfer (see figure 4.12). As to the last point a plot of the valence electron charge density at 0 and 5 GPa is shown in figure 4.13. On increasing the pressure a reduction of the electron density between nearest neighbour intrachain Te atoms in favour of an enhancement of the charge density towards the Te atom in the adjacent chain takes place thus indicating a pressure driven interchain charge transfer. This has been also identified as the underlying mechanism for the metallization process.

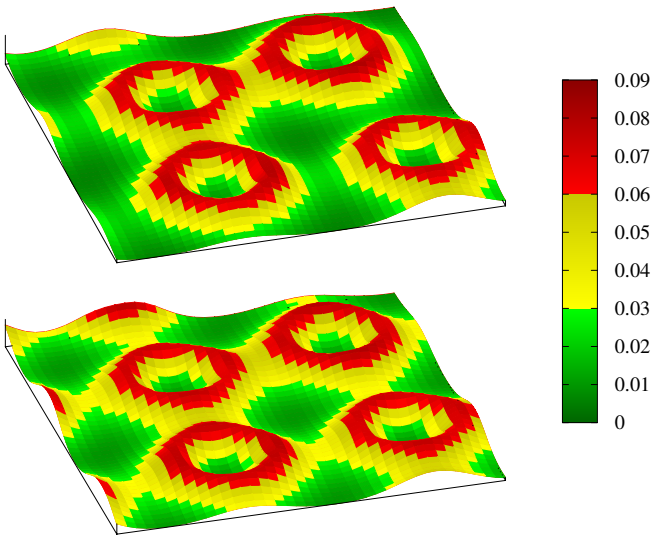

FIGURE 4.13: Valence electron charge density (arbitrary units) calculated at 0 GPa (a) and 5 GPa (b) for the plane containing three nearest neighbour and a second neighbour atom.

Chapter 5

High pressure measurements on $NiS_{2-x}Se_x$

Transition metal pyrites provides a particularly interesting opportunity to study, both theoretically and experimentally, systems characterized by narrow band electron configuration. In determining their physical properties, a decisive role is played by 3d metal bandwidth and local 3d electron correlation. This is the case of NiS_2, which, having a half filled e_g band, is expected to be a metal, but it is an insulator. To explain this point and clearly disentangle the effect of Se alloying and pressure, Raman and Infrared measurements have been carried out on several compound of $NiS_{2-x}Se_x$ family under ambient pressure and temperature conditions as well under high pressure on the parent compound NiS_2. In this chapter, after reviewing the most relevant optical measurements on the system available in the literature, the main results obtained from our high pressure spectroscopic investigation will be presented and discussed. The comparison of optical properties of $NiS_{2-x}Se_x$ compounds with that of NiS_2 as function of pressure demonstrates that despite the strong similarities, Se-alloying and pressure work in a completely different way in rendering metallic the charge transfer insulator NiS_2.

5.1 Optical studies on Ni-pyrites

5.1.1 Survey of Raman measurements on $NiS_{2-x}Se_x$

Raman spectroscopy is a powerful tool to study lattice dynamical properties of a system. Moreover, since Raman active modes involve only S (Se) ions displacements [54], this spectroscopic technique is extremely sensitive to changes in anionic composition in $NiS_{2-x}Se_x$. According to traditional group

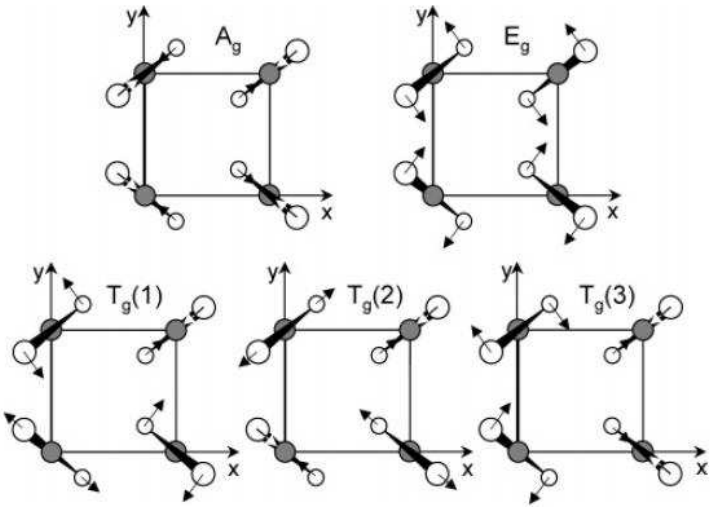

FIGURE 5.1: Atomic displacements for the Raman-active modes of MX_2 pyrite (after ref [134]). Open and filled circles represent X and M atoms, respectively.

theory, pyrites have five active Raman modes, which can be classified into the following symmetry species

$$\Gamma_R = A_g + E_g + T_g(1) + T_g(2) + T_g(3).$$

The atomic displacements of the five Raman active modes of pyrite structure are shown in figure 5.1. The totally symmetric A_g mode corresponds to the in-phase stretching vibrations of the $(S_2)^{2-}$ dimer. In the doubly degenerate librational E_g mode, the S atoms are displaced perpendicularly to the dimer axis. Finally, the triply degenerate T_g modes can be described by various librational and stretching vibrations or their combinations. A particular case could be out-of-phase stretching vibrations of the $(S_2)^{2-}$ dimer, although we should bear in mind that any coupling between librational and stretching motions are allowed by this symmetry species [134]

Room temperature Raman spectra of polycrystalline $NiS_{2-x}Se_x$ thin films for the whole composition range [54] are shown in figure 5.2. Four of the five predicted Raman active modes can be identified in NiS_2 spectrum. Within the low frequency region the doublet, located around 270 and 280 cm^{-1} has been assigned $T_g(1)$ and E_g symmetry types, while, on the high frequency side, a strong peak and a weak shoulder detected at 475 and 485 cm^{-1} have been found to correspond to A_g and $T_g(2)$ symmetries respectively [54, 135, 136]. The spectra of $NiS_{2-x}Se_x$ are qualitatively similar to that of pure NiS_2, since librational peaks of NiS_2 seem to evolve continuously into the stretching

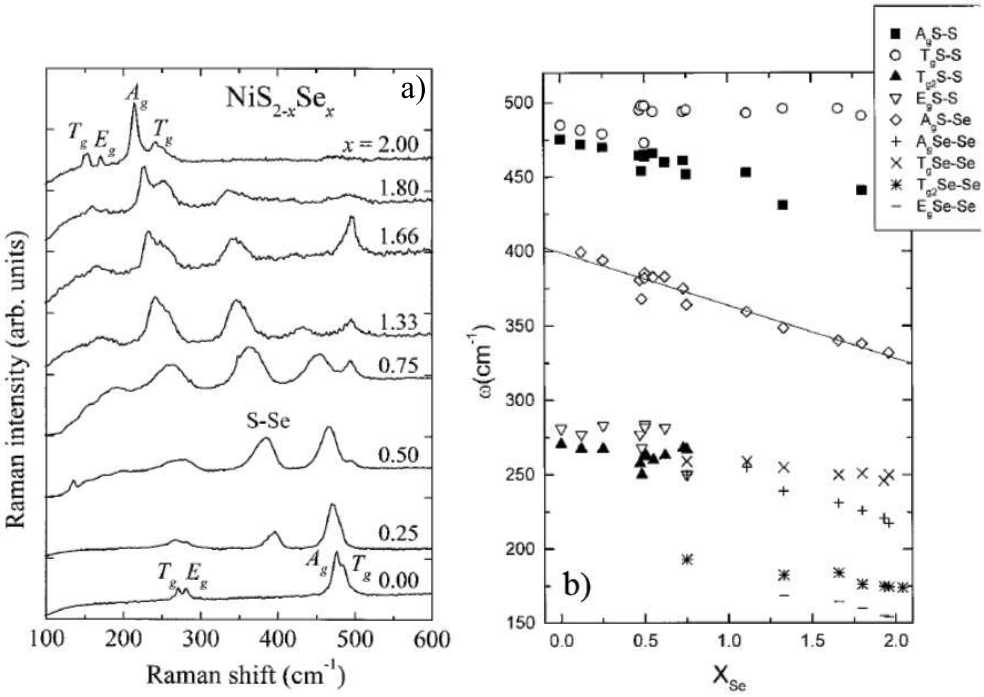

FIGURE 5.2: a) Room temperature Raman spectra of the $NiS_{2-x}Se_x$ for indicated values of x. b) Frequency of the vibrational modes versus x obtained from the Raman spectra [54].

peaks of $NiSe_2$. The symmetry assignation of the peaks appears to be actually the same. Spectra of $NiS_{2-x}Se_x$ samples show an additional peak, situated between the low-energy T_g, E_g doublet and the high energy A_g, T_g pair, assigned to A_g symmetry, which corresponds to the stretching vibration of mixed S-Se pairs [135]. This assignment is supported by the fact that its intensity vanishes for the two end compounds and reaches a maximum for x $\sim$ 1. The presence of this peak shows that S-Se pairs are formed, in contrast with other systems with the pyrite structure, such as RuS_xSe_{2-x}, where S and Se do not bond together [137].

For x $>$ 0.4 an additional strong peak around 500 cm^{-1} whose frequency does not change with x and which reaches a maximum for around x = 1.7, can be observed in the spectra of figure 5.2 a). The authors of ref. [54] ascribed this feature to NiS_2 precipitate within the $NiS_{2-x}Se_x$ alloy or with disorder-activated peaks.

Phonon frequencies of $NiS_{2-x}Se_x$ as function of the Se content are shown in panel b) of figure 5.2. As it can be seen from the figure, all phonon frequencies are found to decrease more or less linearly with increasing the Se content. This trend can be easily understood, since increasing the Se content

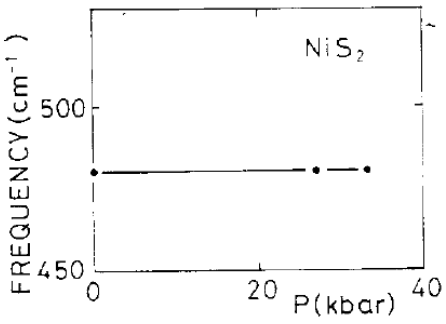

FIGURE 5.3: Pressure dependence of the Raman frequency shift of NiS_2 [138].

is accompained by a linear increase in lattice constant [54, 75].

High pressure Raman response of NiS_2 up to 13.2 GPa have been investigated by Takahashi *et al.* in early 80's [138]. No indications of a structural phase transition are found in the system according to high pressure X ray diffraction data [75]. Unfortunately no spectra are shown in ref. [138]. The pressure dependence of A_g mode up to 33 kbar is reported in figure 5.3. The costant value of A_g mode cannot be explained by simple consideration of compressibility, but it may be explained by electron-phonon (e-ph) interaction [57]. Indeed the results of electrical conductivity, thermoelectric-power, and Hall effects measurements as function of temperature carried out on single crystal $Ni_{1-x}Co_xS_2$ ($0 \leq x \leq 0.12$) exhibit anomalous properties which cannot be accounted for in term of conventional one electron band theory, requiring instead a model which involves small polaron hopping conduction in a narrow correlation split band also in the case of pure NiS_2 [57]. It is worth to notice that remarkable e-ph coupling could significatively broaden the phonon peaks [139]

5.1.2 Survey of Infrared measurements on $NiS_{2-x}Se_x$

In the last few years several infrared measurements have been carried out on $NiS_{2-x}Se_x$ in order to elucidate the nature of the Se alloying- and pressure-induced MITs. At ambient conditions reflectance spectra and optical constants of pyrites MX_2, (where M = Fe, Co, Ni, Cu, and X = S, Se, Te) have been investigated from 0.5 to 5.0 eV by Bither et al. in early 70's [140]. According to ref. [140] the optical properties of 3d metal disulfides can be interpretated in terms of a qualitative band model, in which the metallic or semiconducting behaviors of this class of systems can be ascribed to metal-sulfur-metal overlap. While t_{2g} orbitals of the transition metals are still regarded as 'localized' on the cations, e_g electron are believed to play a key

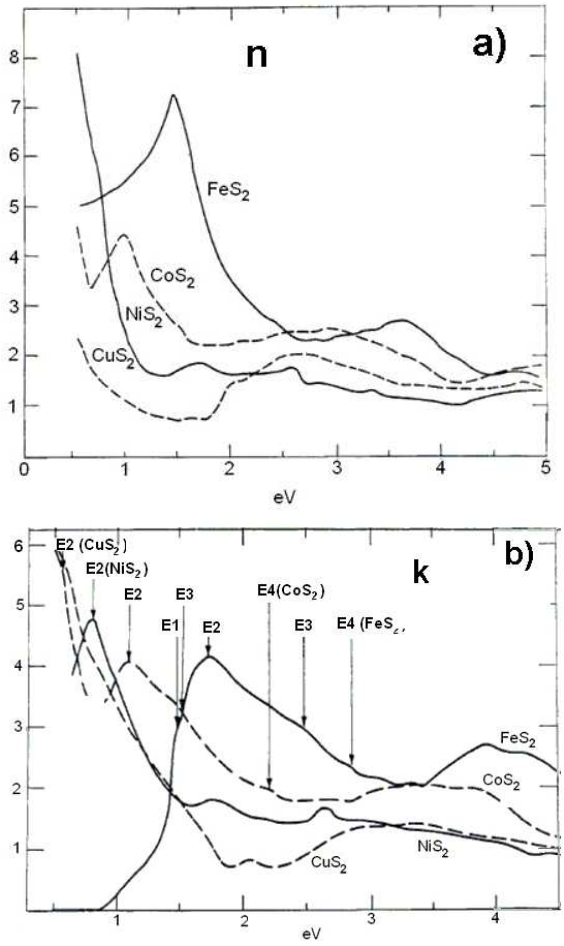

FIGURE 5.4: Real (a) and imaginary (b) parts of the complex refractive index for FeS_2, CoS_2, NiS_2, and CuS_2 at ambient condictions [140].

role in determining the extent of orbital overlap and low energy electronic excitations (see 2.2.3 section). E1, E2, E3 and E4, absorption peaks in the imaginary part of the refractive index [see panel b) of figure 5.4], correspond to the onset of the $t_{2g} \rightarrow e_g$ transitions [140].

More recently the infrared response of $NiS_{2-x}Se_x$ as a function of Se alloying and pressure has been studied by Takahashi et al. [141]. Reflectivity spectra of $NiS_{2-x}Se_x$ in the $0 \leq x \leq 1$ range divided by that of pure NiS_2 at ambient pressure are shown in panel a) of figure 5.5 [141]. Beyond some unwanted disorder effects in the optical spectra [141], it is observed that the reflectance in the low energy region increases with the substitution of Se for S, suggesting the onset of a charge delocalization process. Reflectivity spectra of single crystal NiS_2 from 0.5 to 3.8 eV up to 70 kbar are reported in

panel b) of figure 5.5. Also in this case, an increase of low energy reflectivity occurs, while the pressure dependence is small in the high frequency side. The enhance of reflectivity of NiS_2 above 41 kbar can be attributed to a Drude term related to the appearance of the metallic state. From these spectra, the real part of dielectric constant ϵ_1 has been calculated by Kramers-Krönig analysis [see panel c) of figure 5.5]. We notice that negative value of ϵ_1 are usually related to the existence of mobile electrons [68]. A close inspection

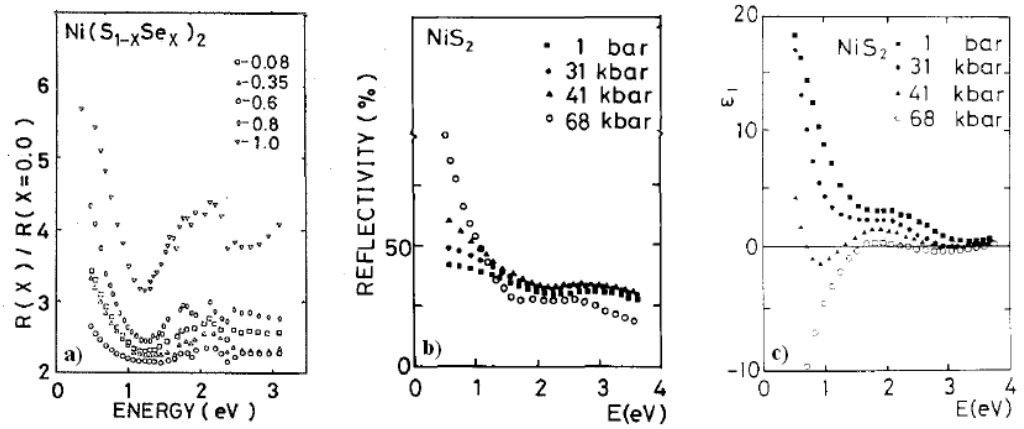

FIGURE 5.5: Room temperature reflectivity spectra of: $NiS_{2-x}Se_x$ a) and NiS_2 at selected Se content and pressure respectively. c) Real part of the dielectric constant as function of pressure. After refs [141]

of panel c) of figure 5.5 reveals at 4.1 GPa an anomalous behavior of the ϵ_1 spectrum, which is found to cross the zero value at around 0.8 and 1.2 eV respectively. This latter finding suggests a correlated bad metal behavior of NiS_2 as the pressure is increased above 4 GPa.

5.2 Synthesis and characterization of $NiS_{2-x}Se_x$ samples

$NiS_{2-x}Se_x$ samples have been provided by Prof. D. D. Sarma of the Indian Institute of Science of Bangalore (India). High density pellets of $NiS_{2-x}Se_x$ were made by reacting spectra-pure elements in stoichiometric ratios, with 5-10 % of the chalcogens taken in excess, in order to compensate for evaporation. The elements were sealed in evacuated (10^{-5} torr) quartz ampules, and heated to 450 K for a week. The samples then produced were characterized by x-ray diffraction, resistivity and photoemission measurements [142].

5.2.1 Optical characterization

Preliminary Raman and Infrared measurements on policrystalline $NiS_{2-x}Se_x$ alloy with different x values are shown in panel a) and b) of figures 5.6.

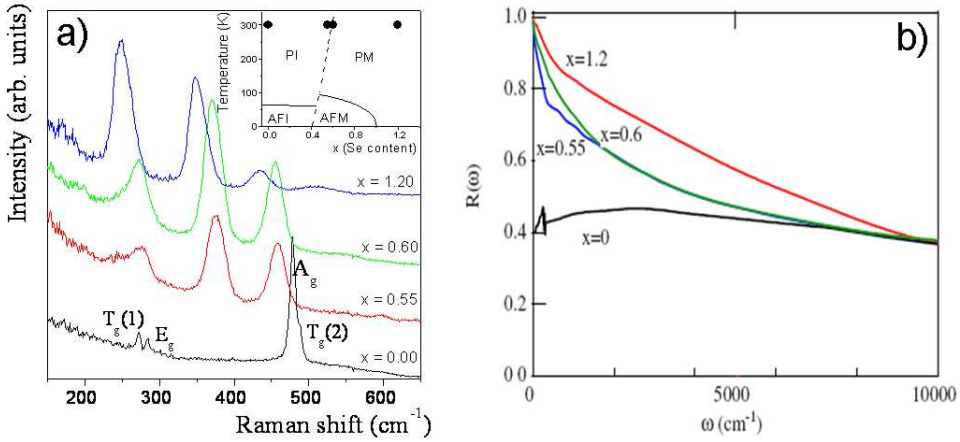

FIGURE 5.6: Raman (panel a) and optical reflectivity (panel b) spectra of Room temperature $NiS_{2-x}Se_x$ for $x = 0.0, 0.55, 0.6, 1.2$ at ambient conditions. Inset: Phase diagram of $NiS_{2-x}Se_x$ [4]. Black dots correspond to the samples measured in this work.

Our Raman data are in agreement with those previously reported in literature [54, 135, 136]. The homogeneity of the sample have been checked by comparing the raman spectra collected in different sample points. No polarization effects have been detected in the present analysis. The absence of peak located around 500 cm^{-1} indicates the good quality of the sample under investigation with respect those studied in ref. [54].

The ambient pressure nearly normal incidence reflectivity $R(\omega)$ has been measured between 50 and 35000 cm^{-1}. An *in situ* evaporation technique was used to measure the reference (see appendix C). The Reflectivity $R(\omega)$ of NiS_2 at ambient pressure is nearly flat from 50 to 10 000 cm^{-1} except for weak phonon contributions at 260 and 290 cm^{-1}. On increasing the Se content, $R(\omega)$ is progressively enhanced at low frequencies, characteristic of a metallic behavior.

Since the quality of the sample and in particular the distribution of Se atoms within the lattice is particularly important in these systems, we carried out a careful data analysis of the collected Raman and Infrared spectra. Moreover since the only previous Raman and Infrared studies were affected by some criticism, the present analysis at ambient condition on $NiS_{2-x}Se_x$ can be considered as a research study in itself rather then a mere characterization. For this reasons the analysis will be reported in the next paragraph.

5.3 NiS_2 at ambient pressure

5.3.1 Infrared vs Se alloying

The real part of the optical conductivity has been determined through Kramers-Krönig (KK) transformations starting from Reflectivity data shown in panel b) of figure 5.6. To this end, standard extrapolation procedures were adopted at both high and low frequency [146, 147]. The optical conductivity of NiS_2 is strongly depleted at low frequency (see figure 5.7), showing the Charge Transfer (CT) gap (evaluated at Full-Width-Half-Maximum of the absorption). On increasing the Se-content x, a large amount of spectral weight (SW) is transferred from high to low frequency through an isosbestic point at 8000 cm^{-1}.

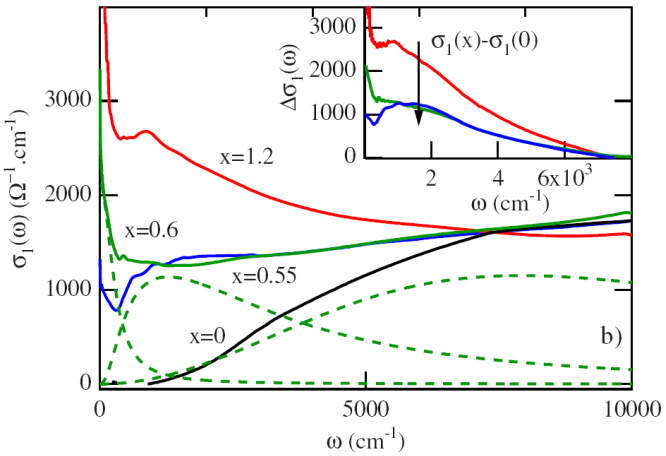

FIGURE 5.7: Room temperature optical conductivity spectra of $NiS_{2-x}Se_x$ for $x = 0.0, 0.55, 0.6, 1.2$ obtained from KK transformations. Thick dashed lines represent the DL fit of the $x = 0.6$ sample. Inset: Difference $\Delta\sigma_1 = \sigma_1(x) - \sigma_1(x = 0)$ spectra.

This suggests the main role played in the MIT by electronic correlations [4]. As it is better highlighted by the $\Delta\sigma_1 = \sigma_1(x) - \sigma_1(x = 0)$ difference spectra in the inset of figure 5.7, the low energy contribution to the $\sigma_1(\omega)$ is made up of two well distinct terms: one broad mid-IR band peaked around 2000 cm^{-1} and extending up to nearly 8000 cm^{-1}, and a sharp contribution below 500 cm^{-1}. In analogy with spectra of metallic V_2O_3 [148, 149], the narrow peak is attributed to quasi-particle (QP) coherent excitations around E_F, while the mid-IR term is associated to optical transitions from the QP peak to the upper and lower Hubbard bands. This scenario has been confirmed by fitting the $\sigma_1(\omega)$ curves through a Drude-Lorentz (DL) model.

Data can be described by a Drude term plus two Lorentzian oscillators. The Drude and the low energy oscillator (centered around 2000 cm^{-1}) describe the coherent and the mid-IR excitations around E_F, while the remaining oscillator at 10000 cm^{-1} mimics the CT and Hubbard transitions. The fitting components are reported as thick dashed lines in figure 5.7 for $x = 0.6$.

5.3.2 Raman vs Se alloying

Looking at figure 5.6, in the spectrum of NiS_2 two narrow peaks are well evident at $\sim$ 270 cm^{-1} ($T_g(1)$ + E_g) as well as an intense peak at $\sim$ 470 cm^{-1} (A_g). The latter shows a shoulder on the high frequency side to be ascribed to the $T_g(2)$ vibrational mode. On increasing the Se content, x, the two pairs of phonons, $T_g(1)$ + E_g and A_g + $T_g(2)$, evolves towards two broad bands, whose central frequencies progressively soften. As to the intensity, the two pairs show a different x dependence : at high x-value the $T_g(1)$ + E_g is remarkably enhanced, whereas, on the contrary, A_g + $T_g(2)$ is strongly depressed. The x dependence of the frequencies and intensities of the phonon peaks can be easily related to the Se content, bearing in mind that the substitution of S with Se leads to a progressive increase of the lattice parameter (see 2.2.2 section) and to a gradual change of S−S and Se−Se pair numbers. The substitution of S with Se is also responsible for the detection of the peak located at 370 cm^{-1} in x = 0.55 spectrum, which corresponds to A_g stretching vibration of mixed S-Se pairs. Finally two new Raman active modes, which have been associated to Se-Se libration, appears at 170 and 185 cm^{-1} in higher Se substituted Raman spectrum.

No evidence of the anomalous peak at $\sim$ 500 cm^{-1} discussed in ref. [54] has been found. Bearing in mind that in ref. [54] film samples have been measured, whereas in the present investigation only bulk samples have been considered, we can ascribed the missing 500 cm^{-1} peak to some unwanted substrate effects.

Measured spectra were fitted by using the standard fitting procedure described in chapter 4. Two phonon profiles are employed in the present analysis. Damped harmonic oscillator and simple Gaussian profiles, reported in equation 5.1 and 5.2 respectively, has been chosen to describe phonon excitations [132, 143]:

$$Ph(\omega;\omega_i,\Gamma_i,A_i) \rightarrow \frac{A_i\Gamma_i^2\omega_i\omega}{(\omega_i^2-\omega^2)^2+\Gamma_i^2\omega^2} \tag{5.1}$$

$$Ph(\omega;\omega_i,\Gamma_i,A_i) \rightarrow \frac{A_i}{\Gamma_i} exp\left(-2\frac{(\omega-\omega_i)^2}{\Gamma_i^2}\right) \tag{5.2}$$

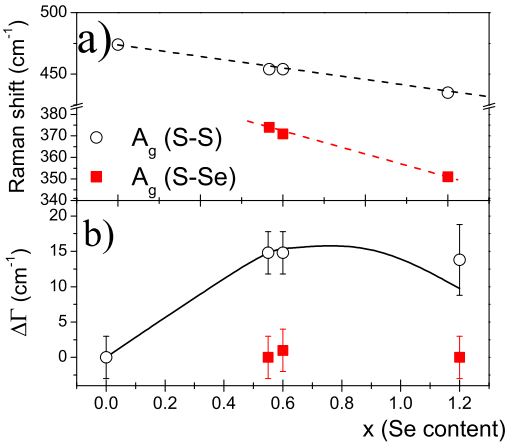

FIGURE 5.8: Phonon frequencies [panel a)] and $\Delta\Gamma = \Gamma(x) - \Gamma(x = 0.00)$ [panel b)] for S−S S-Se pair stretching modes in $NiS_{2-x}Se_x$ with x = 0.00; 0.55; 0.60; 1.20. Dashed and solid lines are guide for eyes and best fit curve respectively.

Best fitting parameters for both models are listed in table 5.1. Except for the $x = 0.00$ spectrum where only four active Raman modes are distinguished, over the whole Se alloying range only six modes are needed for a full description of the main spectral features. Moreover the onset of Se-Se stretching modes makes the analysis of low frequency (240−270 cm^{-1}) structures difficult, affecting the uncertainty determination.

Looking at the table 5.1 we notice that the best fit value of the parameters as obtained using the two models are very close and often within the calculated uncertainties. As it will be discussed in the following the extent of theoretical and experimental agreement depends upon the sample investigated and the model used. For reasons that will be argued in details at the end of this paragraph, we choose a lorentzian (gaussian) description of the phonon contribution in the x = 0.00 (x $\neq$ 0.00) sample spectrum. Phonon frequencies of S-S and S-Se pairs stretching modes as x function, shown in panel a) of figure 5.8, decrease almost linearly, mainly because of the increase of the unit cell volume.

The increase of phonon widths $\Delta\Gamma = \Gamma(x) - \Gamma(x = 0.00)$ for S-S and S-Se pairs stretching modes are shown in panel b) of figure 5.8. On increasing x, the S-S mode rapidly broadens. This last finding can be easily explained in term of substitutional disorder. It is well known that the natural width of the Raman line is determined, aside from experimental resolution, by the phonon lifetime τ which is governed by the spontaneous anharmonic decay into phonons of lower energy [144]. However in disordered systems

the scattering with impurities and defects limit the natural phonon lifetime. According to mass perturbation theory of the harmonic lattice dynamics, phonon linewidth broadening is found to depends mainly on three factors [145]:

$$\Gamma(x) \propto \sigma_m \omega^2 D(\omega) \tag{5.3}$$

where ω is the phonon frequency of the Raman active mode, D(ω) is the phonon density of states, and σ_m is the relative mass variance. The latter is defined as:

$$\sigma_m^2 = y_S \left(\frac{m_S - \overline{m}}{\overline{m}}\right)^2 + y_{Se} \left(\frac{m_{Se} - \overline{m}}{\overline{m}}\right)^2.$$

where $y_S = (2-x)/2$ and $y_{Se} = x/2$ are S and Se atoms fractional occupancies respectively. Since no structural transition occurs on changing the Se content, we can assume, as a first approximation, a nearly constant phonon density of states. Under this hypothesis $\Delta\Gamma$(x) reads as:

$$\Gamma(x) \propto \frac{x(2-x)\left(m_S - m_{\mathrm{Se}}\right)^2 \omega^2}{\left((x-2)m_S - x m_{\mathrm{Se}}\right)^2} \tag{5.4}$$

Theoretical widthline curve for the A_g stretching mode is drawn with solid line in panel b) of figure 5.8. A good agreement is found with experimental data, supporting the idea that disorder is the effective broadening mechanism setting in the system rather than electron phonon interaction.

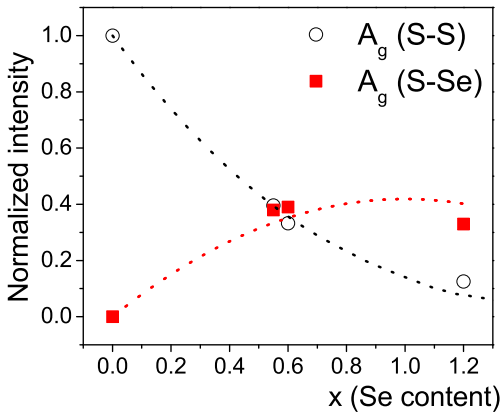

FIGURE 5.9: Normalized phonon intensities of Raman active modes for S−S S-Se pair stretching modes as function of Se content. S−S and S−Se probability distribution are plotted with dashed line.

Bearing in mind that the intensity of a mode involving a specific anionic pair is trivially proportional to the pairs number, an analysis of peaks intensi-

ties as function of the Se content may be very promising for the identification of the atoms species involved in the Raman modes.

Since a comparison among the absolute intensities between different spectra may be questionable, spectra have been normalized to phonon areas. The x dependence of the Raman intensity of S-S and Se-S A_g stretching mode are shown in figure 5.9. On the other hand, under the assumption of a random distribution of Se atoms within NiS_2 lattice, the number of pairs is given by:

$$P(k,n) = \binom{k}{n}\left(\frac{x}{2}\right)^k\left(\frac{2-x}{2}\right)^{n-k} \tag{5.5}$$

where k is the total number of Se atoms in each pair, n is trivially the number of atoms bonded together (i.e. two in our system). As well evident from the figure 5.9, on increasing x S-S pair population diminishes, whereas Se-S pairs number increases, as expected. The good agreement between the normalized intensities and the binomial probability distribution can be read as an *a posteriori* demonstration of the occurrence of substitutional disorder effects in the system.

Finally we discuss the effectiveness of the two fitting models used in the analysis (see equations 5.1 and 5.2). Details of the Raman spectra of x = 0.0 and x = 1.20 $NiS_{2-x}Se_x$ samples are shown in comparison with the best fit curves obtained with lorentzian and a gaussian profiles are shown in figure 5.10. A close inspection of figure 5.10 shows that the gaussian model fails

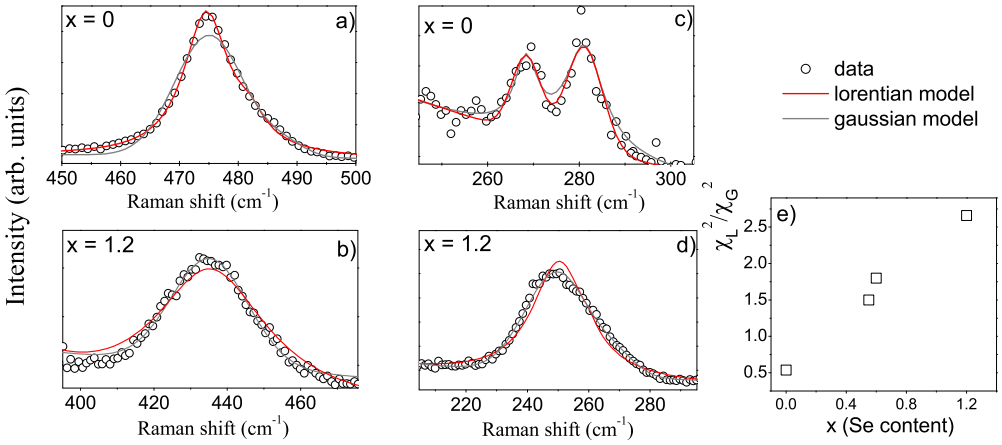

FIGURE 5.10: Details of the Raman spectra of x = 0 and x = 1.2 $NiS_{2-x}Se_x$ samples are shown in comparison with the best fit curves obtained with lorentzian and a gaussian profiles [panel a),b), c), and d)]. Panel e): Reduced chi square ratio χ^2_L/χ^2_G *vs* x.

in the description of experimental data for the pure NiS_2, while it becomes

more effective on increasing the Se content. The x dependence of reduced chi square ratio χ^2_L / χ^2_G [i.e. L (G) → lorentzian (gaussian)] of the two models is shown in the panel d) of figure 5.10. On varying the anionic composition a linear increase of χ^2_L / χ^2_G occurs. Bearing in mind that unhomogeneities and crystal defects strongly reduce the asymmetry of phonon profile, these latter findings can be explained in term of substitutional disorder effects.

TABLE 5.1: ω, Γ and normalized phonon intensities obtained from the above discussed fitting procedure.

Se content	Raman Shift (cm^{-1})		Γ (cm^{-1})		Intensity $\cdot 10^{-2}$ (a.u.)	
	Lor.	Gauss.	Lor.	Gauss.	Lor.	Gauss.
0.00	270 ± 3	270 ± 3	6 ± 3	6 ± 3	6.4 ± 0.3	6 ± 1
	282 ± 3	282 ± 3	9 ± 3	9 ± 3	5.7 ± 0.7	7.2 ± 0.1
	476 ± 3	474 ± 5	9 ± 3	10 ± 3	80 ± 3	79 ± 1
	485 ± 3	482 ± 5	5 ± 3	6 ± 3	7.2 ± 0.9	6 ± 1
0.55	191 ± 4	191 ± 5	20 ± 3	24 ± 3	2.3 ± 0.5	1.9 ± 0.3
	204 ± 5	204 ± 2	22 ± 3	19 ± 3	4.6 ± 0.8	3 ± 1
	235 ± 3	238 ± 5	25 ± 3	30 ± 3	4.9 ± 0.6	4.0 ± 0.8
	272 ± 3	272 ± 4	26 ± 5	25 ± 3	19 ± 8	18 ± 3
	373 ± 3	374 ± 3	26 ± 3	23 ± 4	38.0 ± 0.1	37 ± 1
	457 ± 3	454 ± 3	24 ± 3	21 ± 3	31 ± 4	22 ± 2
0.60	192 ± 6	196 ± 3	16 ± 7	16 ± 8	0.6 ± 0.1	0.4 ± 0.1
	204 ± 5	206 ± 3	49 ± 3	50 ± 3	7 ± 1	8.5 ± 0.2
	243 ± 3	260 ± 3	46 ± 3	45 ± 3	8.0 ± 0.8	8.8 ± 0.4
	271 ± 3	273 ± 3	36 ± 3	19 ± 3	23.0 ± 0.8	20 ± 2
	370 ± 3	371 ± 3	26 ± 3	24 ± 3	39 ± 1	41 ± 5
	454 ± 3	454 ± 3	25 ± 3	23 ± 3	22.1 ± 0.6	19 ± 6
1.20	170 ± 3	169 ± 3	19 ± 9	22 ± 8	2 ± 1	2 ± 1
	182 ± 3	189 ± 3	9 ± 3	15 ± 7	1.3 ± 0.3	1.0 ± 0.4
	244 ± 3	248 ± 3	19 ± 4	27 ± 4	33 ± 2	44 ± 6
	258 ± 3	250 ± 5	14 ± 3	15 ± 3	14 ± 4	7 ± 3
	350 ± 3	351 ± 3	22 ± 4	23 ± 3	34 ± 5	39 ± 3
	435 ± 3	435 ± 3	28 ± 5	23 ± 3	9 ± 4	7.0 ± 0.7

5.4 NiS_2 at high pressure

5.4.1 High pressure Raman measurements on NiS_2

Using the same experimental apparatus described in 3.2 section, high pressure Raman measurements on a small polycristalline slab ($\approx$ 50x10x10μm^3) of NiS_2 have been performed.

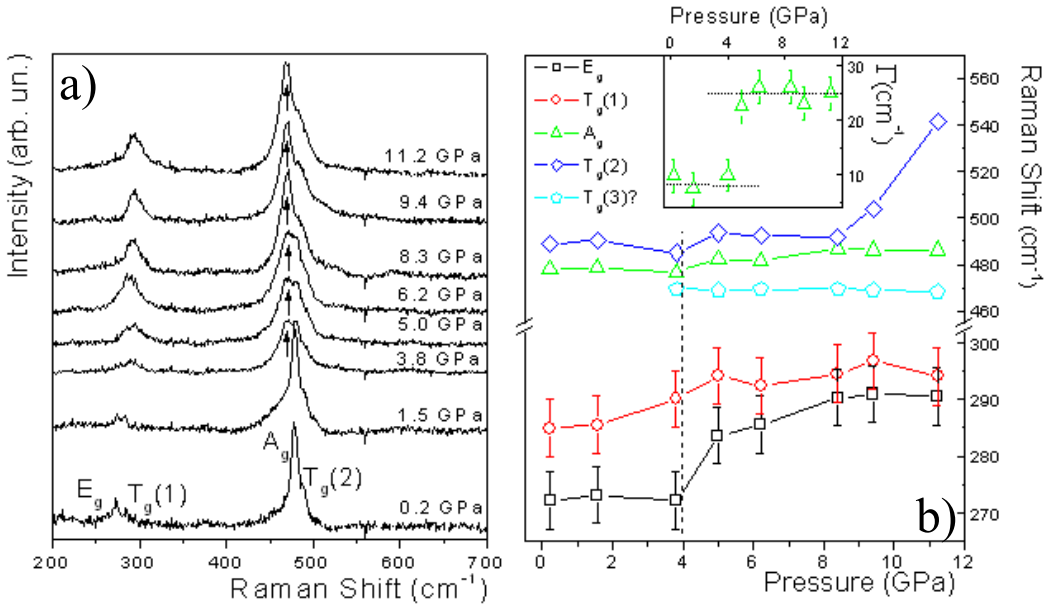

FIGURE 5.11: panel a) Room temperature Raman spectra of NiS_2 subtracted by diamond fluorescence and electronic background at selected pressure; panel b) Phonon frequencies as function of pressure. Inset full width at half maximum (Γ) for the A_g stretching mode as function of pressure

Raman spectra at different working pressure are shown in the panel a) of figure 5.11. Under lattice compression up to 3.8 GPa, the four peaks structure characteristic of the ambient pressure Raman response persists and all the phonon frequencies keep almost constant. Already at 3.8 GPa and on further increasing the pressure a shoulder on the low frequency side of the A_g mode at 470 cm^{-1} [see the arrow in panel a) the figure 5.11] appears, and a general hardening of all the phonon modes is observed. As usual we checked out the absence of strong and remarkable pressure gradient by comparing the spectra collected from different points of the sample. On the other hand, recent high pressure Raman measurements on FeS_2 pyrite have proved that non hydrostaticity mainly affects phonon widths and actually does not affect the phonon central frequencies and intensity pressure dependence [150].

Raman spectra have been analysed using the usual fitting procedure described in the previous 4.2 section and the best fit values of the phonon central frequencies are shown as a function of the pressure in panel b) of figure 5.11. All the high frequency modes appear almost pressure independent over the whole explored pressure range, except for the one labbeled $T_g(2)$ in panel b) of figure 5.11 which rapidly increase for P > 8 GPa. As to the low frequency modes $T_g(1)$ + E_g, which show a weak almost linear increase of their central frequency over the whole explored pressure range, the latter shows a rather abrupt anomaly at $\sim$ 4GPa, where the MIT occurs. It is worth to notice that also the pressure dependence of A_g phonon width shows a discontinuity at $\sim$ 4GPa [see the inset of panel b) of figure 5.11]. The latter discussed features can be thus assumed as a spectroscopic signature of the MIT.

As to the appearance of the new phonon peak around 470 cm^{-1}, it is possible to conjecture that this structure should be ascribed to $T_g(3)$, which, as an accident, has the same energy of the $T_g(2)$ mode at ambient pressure. However, due to the delicacy of the obtained results, additional measurements are planned in the coming months.

All the Raman results on $NiS_{2-x}Se_x$ reported in the present thesis work provide the x- and P- dependence of the Raman active modes, that is, bearing in mind that volume is expanded by Se alloying whereas it is compressed by pressure, also an extensive volume dependence of the phonon frequencies. As to the volume expansion by Se alloying x ray diffraction data are available in the literature [75]. Whereas as to the volume compression by pressure, structural data are available only up to 6.5 GPa. The volume estimation at higher pressure have been performed using the procedure developed in ref. [151]. Indeed the pressure dependence of the volume can be calculated from the zero pressure bulk modulus B_0. First of all, we consider the value v_s of the sound velocity [68]:

$$v_s = \frac{k_B}{\hbar}\Theta_D \frac{1}{\sqrt[3]{\rho\pi^2}}$$

With Θ_D (Debye temperature) and ρ (mass density) values extracted from ref. [67] (i.e. Θ_D = 350 cm^{-1} , ρ = 4455 kg/m^3) one achieves the sound velocity v_s, which corresponds to v_s= 4300 m/s for NiS_2. The bulk modulus B_0 can be estimated from:

$$B_0 = \rho v_s^2$$

The above values for ρ and v_s finally give B_0= 83 GPa. Assuming $B(P) = B_0 + B'P$, $V(P)$ is finally given by the Birch-Murnagham (B-M) equation

[152]

$$V = V_0 \left[1 + \frac{B'}{B_0} P\right]^{-1/B'} \tag{5.6}$$

where B' normally ranges between 4 and 8 [153].

The volume dependence of the phonon modes of NiS_2 on applying pressure as well as on Se-alloying is shown in figure 5.12. In order to simplify the analysis of the figure let look at the open stars there shown which represent a weighted average of the high- and low-frequency modes. Bearing in mind that a softening under volume expansion is the expected behaviour of phonon frequencies, it is rather evident that the metallization process under pressure is phonon-assisted and that only the high-frequency modes are involved. Within the volume range relative to Se-alloying both high- and low-frequency modes show the expected softening with the same $d\omega/dV$ rate. It is finally worth to notice that looking at the individual phonons under pressure, the $T_g(2)$ mode suggests the onset of a new regime at high volume compression (P > 8 GPa) and that the E_g mode appear to be affected by the pressure induced MIT.

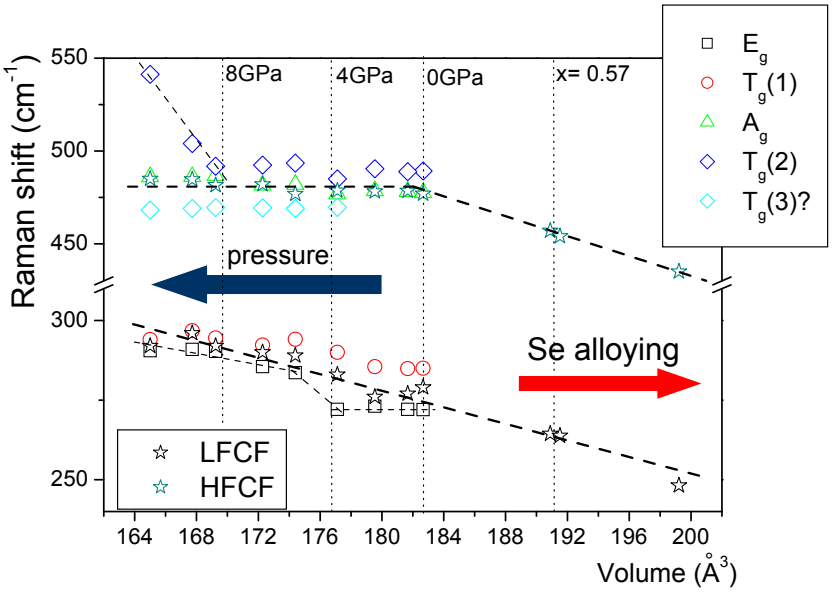

FIGURE 5.12: volume dependence of phonon frequency of NiS_2 and $NiS_{2-x}Se_x$. Open stars represent a weighted average of the high- and low-frequency modes, whereas dashed line are guides for eyes.

5.4.2 High pressure Infrared measurements on NiS_2

A NiS_2 10μm thick slab, obtained by pressing finely milled sample powder between the diamond anvils, has been placed in the gasket hole, where a NaCl pellet was previously sintered. The experimental setup described in 3.3 section has been employed for the present measurements. The slits of the microscope were carefully adjusted to collect transmitted and reflected light from the sample only and kept fixed for all the experiment.

High-pressure reflectivity spectra at diamond interface $R_{sd}(\omega)$ on NiS_2 are shown in figure 5.13. The strong two-phonon diamond absorption provides reliable data only above 2000 cm^{-1}. On increasing the pressure, $R_{sd}(\omega)$ is progressively enhanced at low-frequency showing an overdamped behavior, as a signature for a correlated bad metallic state. At high-frequencies all $R_{sd}(\omega)$ converge above 10000 cm^{-1}. In order to evaluate the accuracy of our high pressure measurements, we compare the $R_{sd}(\omega)$ data to the expected reflectivity at a sample-diamond interface, $R_{sd}^{cal}(\omega)$.

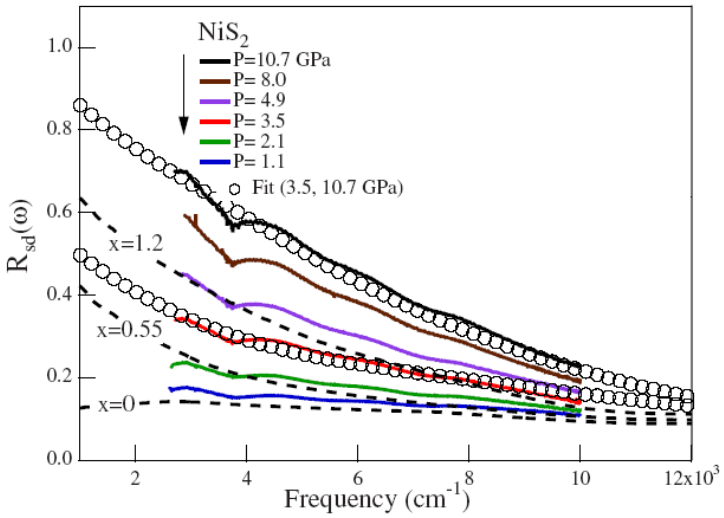

FIGURE 5.13: Room temperature $R_{sd}(\omega)$ measured for NiS_2 at high-P (thick solid lines) (open symbols show DL fits) and calculated $R_{sd}^{cal}(\omega)$ at sample-diamond interface for $NiS_{2-x}Se_x$ at selected x (dashed lines). The kink in $R_{sd}(\omega)$ at about 3700 cm^{-1} is instrumental.

The calculated $R_{sd}^{cal}(\omega)$ for NiS_2 (dashed lines in figure 5.13) is in good agreement with $R_{sd}(\omega)$ measured in the DAC at the lowest pressure (1.1 GPa) being both nearly flat and with a value $\approx 20\%$ over the whole frequency range. The same procedure has been applied to $NiS_{2-x}Se_x$ ($x = 0.55$, 0.6, 1.2) compounds and the resulting $R_{sd}^{cal}(\omega)$ are shown in figure 5.13 for the sake

of comparison. We then tried to fit the $R_{sd}(\omega)$ measured *vs* P for NiS_2 within the same Drude Lorentz framework previously used for $NiS_{2-x}Se_x$ at ambient pressure (see section 5.2). Although a certain degree of arbitrariness remains in fitting the data over a restricted spectral range, a reliable description of the $R_{sd}(\omega)$ at any pressure is obtained by the sum of a Drude and a mid-IR term plus a high-frequency oscillator kept constant at all pressures. This fit provides a robust estimate of the quasi-particle spectral weight (SW), defined by the sum of the Drude and of the mid-IR intensities. This sum remains nearly unchanged by varying the fitting parameters over realistic ranges. The microscopic mechanisms inducing the pressure and Se alloying MITs are further investigated by studying the quasiparticle SW as a function of the cubic lattice parameter *a*. The quasiparticle SW, shown for pure NiS_2

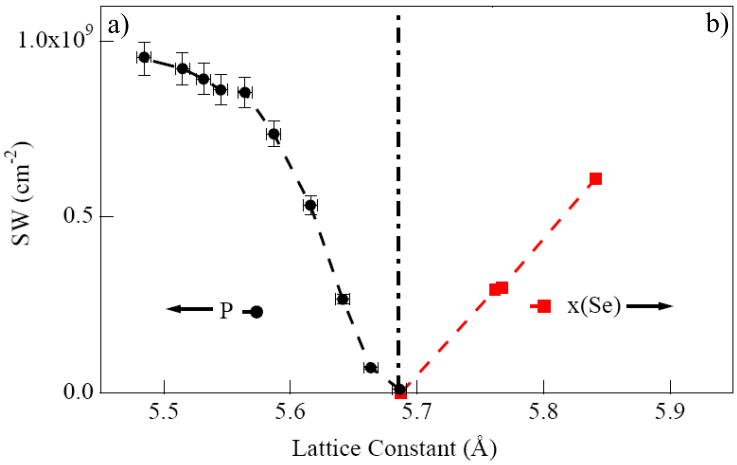

FIGURE 5.14: QP spectral weight (see text) *vs* lattice constant *a* for NiS_2 (a) and $NiS_{2-x}Se_x$ (b)

at each working pressure in figure 5.14 (a) and for $NiS_{2-x}Se_x$ at different Se contents in figure 5.14 (b), reveals a striking nonmonotonic behavior as a function of *a*. Its slow continuous increase for a < 5.57 *Å* (i.e., at the highest values of the pressure) reflects the progressive enhancement of the kinetic energy due to the applied P and corresponds to a nearly complete metallization of NiS_2. For a~ 5.57 *Å* up to $a_{eq} \sim 5.68$ *Å* (namely, the lattice parameter corresponding to NiS_2 at ambient conditions), correlation effects get larger and the SW drops rapidly to zero as a consequence of the Mott transition. On further increasing a above a_{eq} due to the Se alloying, the SW restarts to increase, owing to the onset of the Se-induced MIT. Despite the opposite behavior of the lattice parameter vs Se alloying and pressure, a linear scaling factor f $\sim$ 0.14/GPa between x and P has been formerly established from low-T dc-resistivity data [74] thus suggesting an equivalency

between the two metal insulator transition. However, the same f does not apply comparing the optical SW dependence on P and x. It is indeed clear from figure 5.14 that the rate of increase in SW is much larger with pressure than with x. The breakdown at finite frequencies of the dc linear scaling between x and pressure suggests that while a metallic state can be obtained from NiS_2 both by applying pressure and by alloying Se, this state takes place through substantially different microscopic mechanisms, involving different redistributions in the electronic density of states.

5.4.3 High pressure theoretical calculations on $NiS_{2-x}Se_x$

A qualitative understanding of the two different MITs can be obtained through self-consistent Nth order muffin-tin orbital (NMTO) Local Density Approximation (LDA) calculations [154] (see figure 5.15) performed in collaboration Dr. G. Sangiovanni (Max-Planck Institut Stuttgart, Germany).

At ambient pressure the Ni e_g-states with a bandwidth $W_{e_g} = 2.1$ eV and the antibonding $pp\sigma^\star$-S states are separated by a CT gap (Δ_{LDA}) centered around 1.5 eV. Beside this gap, a second LDA-CT gap is present between occupied $pp\pi$-S states below E_F and the e_g-Ni states [62]. Upon applying pressure, the lattice contracts and the entire band-structure around E_F is renormalized; e.g. by a factor of 1.13 at $P = 10$ GPa (dashed curve in figure 5.15 panel a). All features of the DOS stay the same, in particular, the energy scales, (W_{e_g} and Δ_{LDA}, are rescaled by a factor 1.13. Hence, the bandwidth-gap ratio $W_{e_g}/\Delta_{\mathrm{LDA}}$ remains nearly constant. On the other hand, the interaction U can be assumed to be constant, so that W_{e_g}/U increases by the factor 1.13, triggering a bandwidth-controlled metal insulator transition (BC-MIT). In the case of Se-substitution, the lattice expands (instead of shrinking) due to the larger atomic radius of Se ions. This leads to a very complementary scenario: While the changes of the e_g-bandwidth W_{e_g} are negligible, the CT gaps shrink (see figure 5.15 panel b). Assuming U again to be constant, the driving force for the metal insulator transition is now the the reduction of the charge transfer gap ($W_{e_g}/\Delta_{\mathrm{LDA}}$ increases, as W_{e_g} remains basically unaffected).

To compare with the experimental spectral weight, LDA "plasma frequency", defined by the average of the velocity over the Fermi surface has been calculated, in order to estimate for the weight of the Drude peak, which in turn is related to the experimental integrated (low frequency) spectral weight (see figure 5.16).

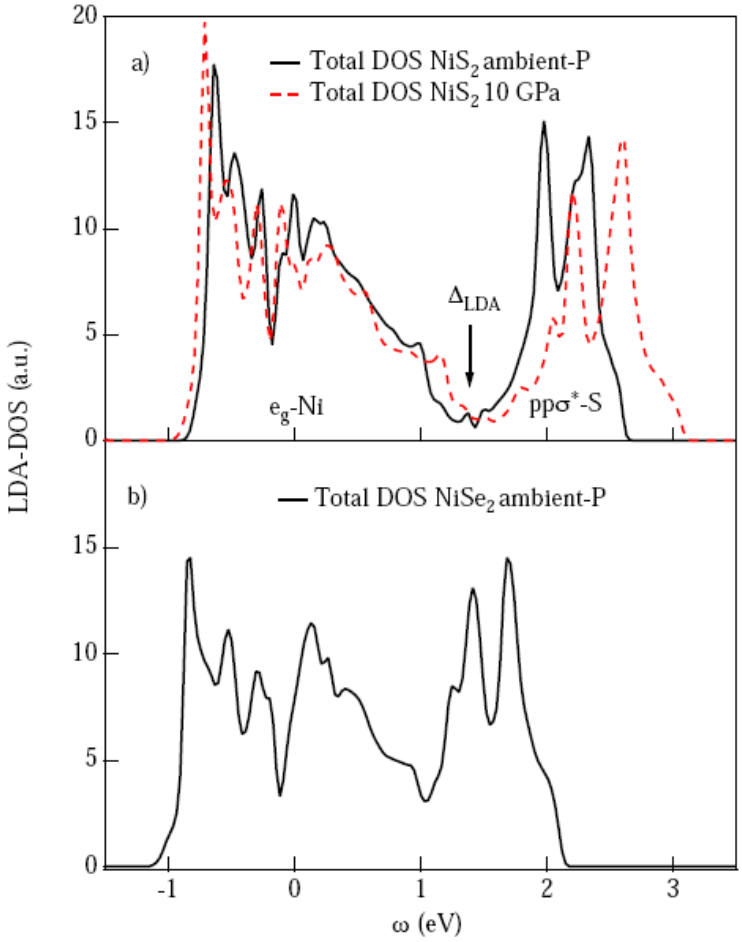

FIGURE 5.15: a) Total LDA-DOS for NiS_2. Solid line represent the DOS at ambient pressure, dashed lines at 10 GPa. b) Total LDA-DOS for the $NiSe_2$ compound. In the case of NiS_2, the 10 GPa DOS can be rescaled by a factor 0.88 on that at ambient pressure, resulting in an increase of W_{e_g}/U, keeping $W_{e_g}/\Delta_{\mathrm{LDA}}$ fixed. In contrast, Se-substitution results in a decrease of W_{e_g}/U and an increase of $W_{e_g}/\Delta_{\mathrm{LDA}}$ due to the shrinking of the charge-transfer gap Δ_{LDA}

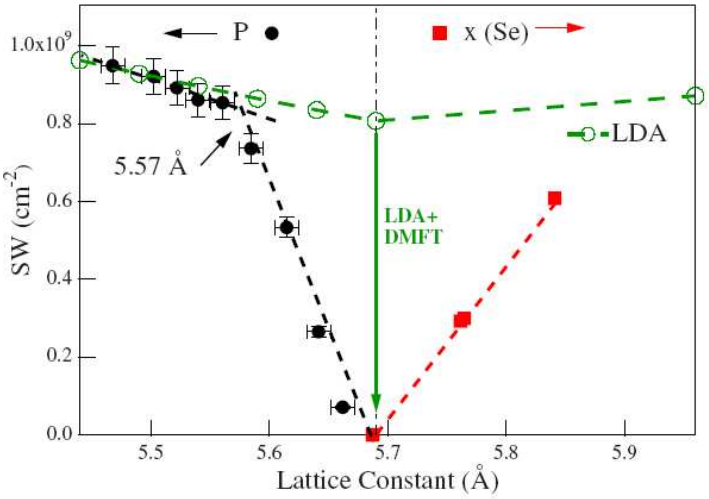

FIGURE 5.16: Comparison between experimental and LDA calculated spectral weight (SW) as function of the lattice parameter

Because of the different changes in the bandstructure under pressure and upon Se alloying, LDA gives very different slopes in agreement with experiment. For the insulating NiS_2 compound and close to the phase transition, correlations are not negligible and we have to do LDA plus Dynamical Mean Field Theory (DMFT) [155, 156] calculations. To this end, the NMTO bandstructure was downfolded to effective Ni e_g-states and the correlations of these two orbitals were treated by means of DMFT. For $U > 3J$ (U being the intra-orbital Coulomb interaction between the Ni e_g-states and J the Hund coupling), we find an opening of a gap for NiS_2, the two e_g-orbitals split. This insulating LDA+DMFT solution results in a very strong suppression of the plasma frequency (as well as of the SW) as indicated by the vertical arrow in figure 5.13).

Besides important similarities between the pressure- and Se- dependent phase diagrams, the present optical study reveals that a simple linear scaling between pressure and x, as that suggested by transport, does not hold at finite frequencies. The difference can be understood theoretically in terms of the two fundamental parameters for the MIT in a CT insulator: under pressure, $W_{e_g}/\Delta_{LDA} = \text{const.}$ and W_{e_g}/U increases, triggering the MIT; in contrast upon alloying Se, the increase of W_{e_g}/Δ_{LDA} is responsible for the MIT, whereas W_{e_g}/U even decreases. This makes $NiS_{2-x}Se_x$ under pressure an ideal system for the study of the MIT in a CT strongly correlated system.

Chapter 6

High pressure measurements on VO_2

VO_2 as well as many other Vanadium oxides shows a MIT (5 order of magnitude jump in conductivity) accompanied by a structural transition (monoclinic to rutile) at 340 K. In order to decouple the effects of the electron-electron and the electron-phonon interaction in leading the MIT occurring in this system, room temperature pure VO_2, in the monoclinic M1 phase, and two Cr-doped VO_2 samples, in the M2 and M3 monoclinic phases, respectively, have been studied as a function of pressure by means of Raman and Infrared spectroscopy. In this chapter, after a survey of optical measurements on the system is reported, high pressure measurements on pure and Cr-doped VO_2 are discussed and compared.

6.1 Optical studies on VO_2

6.1.1 Survey of optical measurements on VO_2

VO_2 have been object of several optical studies based on Raman and infrared investigations while, no optical data on Cr-doped VO_2 are available in the literature to the best of our knowledge.

Raman studies on pure VO_2 showed that the symmetry change at the MIT involves a complete modification of the phonon spectrum of the system. Typical Raman spectra of VO_2 below and above the transition temperature are reported in figure 6.1 (from Ref. [157]) and figure 6.2 (from Ref. [158]). In the monoclinic phase ($T < 340$ K) 17 peaks have been resolved [158]. A strong polarization dependence of the relative intensities of the peaks was observed on single crystals [158, 159], but most of the peaks were visible in all the

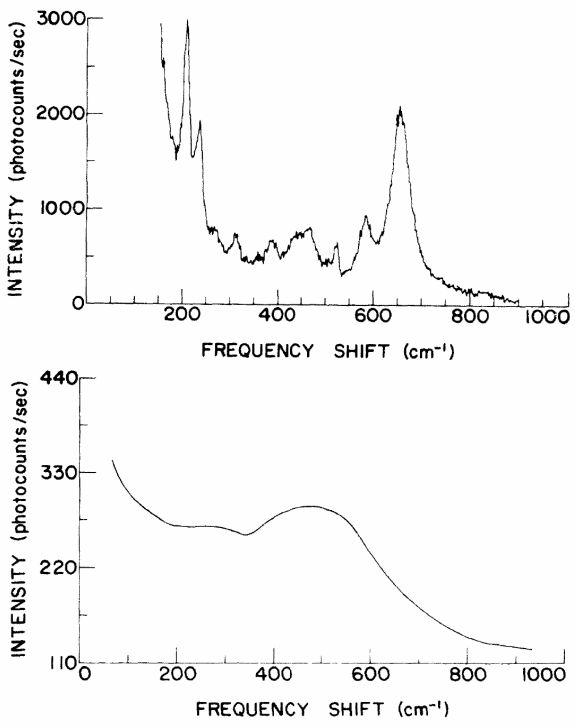

FIGURE 6.1: Raman spectra of VO_2 at 300K (upper panel) and 375K (lower panel) from Ref. [157].

polarization configurations, preventing a direct assignment of the modes to the irreducible representations Ag or Bg. In the rutile phase (T > 340 K) the quite smooth spectrum can be obtained by $3-4$ broad phonon contributions. These results are in agreement with group theory, which predicts 18 modes ($9\ A_g + 9\ B_g$) for the M1 phase, while 4 modes only (A_{1g}+B_{2g}+B_{1g}+E_g) are expected in the rutile phase.

Infrared reflectivity measurements on a VO_2 single crystal have been carried out to determine the infrared (IR) phonon spectrum of monoclinic VO_2. Of 18 IR-active phonon modes modes predicted by group theory in the monoclinic phase 15 have been identified, while, above T_{IM}, the sample shows a high flat reflectivity, typical of free carriers contribution, and no additional phonon contribution can be identified (see figure 6.3).

In order to study the electronic structure of VO_2, several optical investigations, from the IR to the UV frequency region, have been carried out [81, 87, 109, 161, 162]. An extended reflectance and transmittance study from 0.25 eV to 5 eV allowed to obtain the real and the imaginary part of

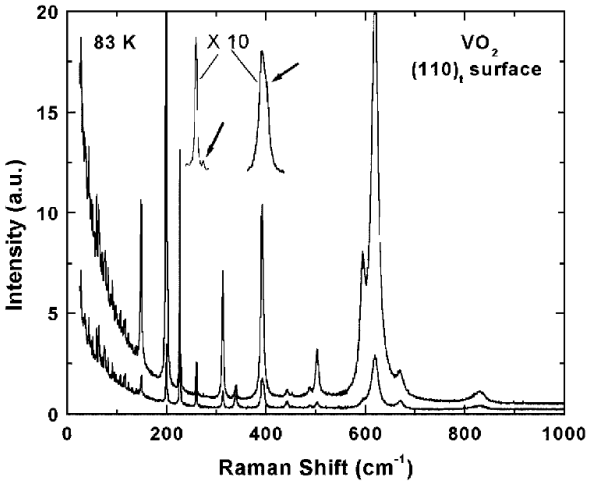

FIGURE 6.2: Raman spectrum of the (110) VO_2 surface at 83K analyzed along two orthogonal polarizations from Ref. [158]. The peak at 265cm^{-1} and the shoulder at 395 cm^{-1} are shown enlarged.

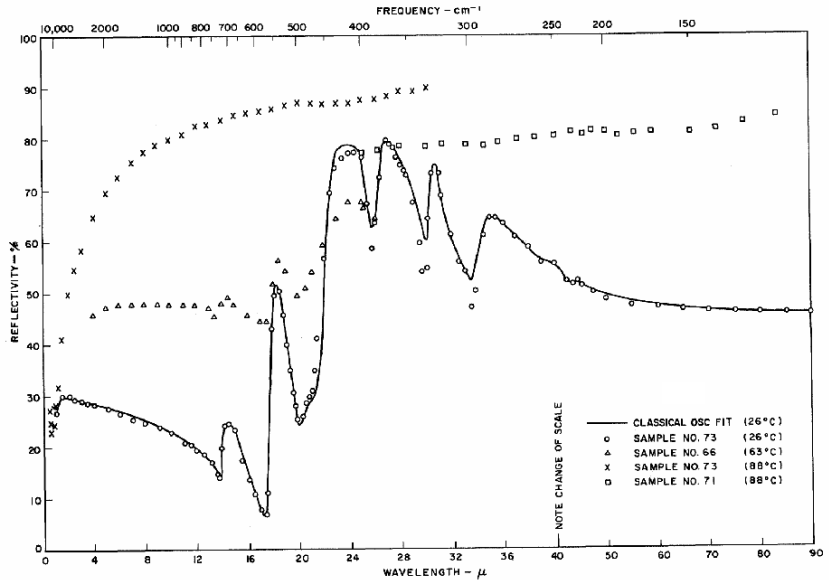

FIGURE 6.3: Infrared reflectivity of a VO_2 single crystal measured with incident polarization parallel to the rutile c axis, from Ref. [160].

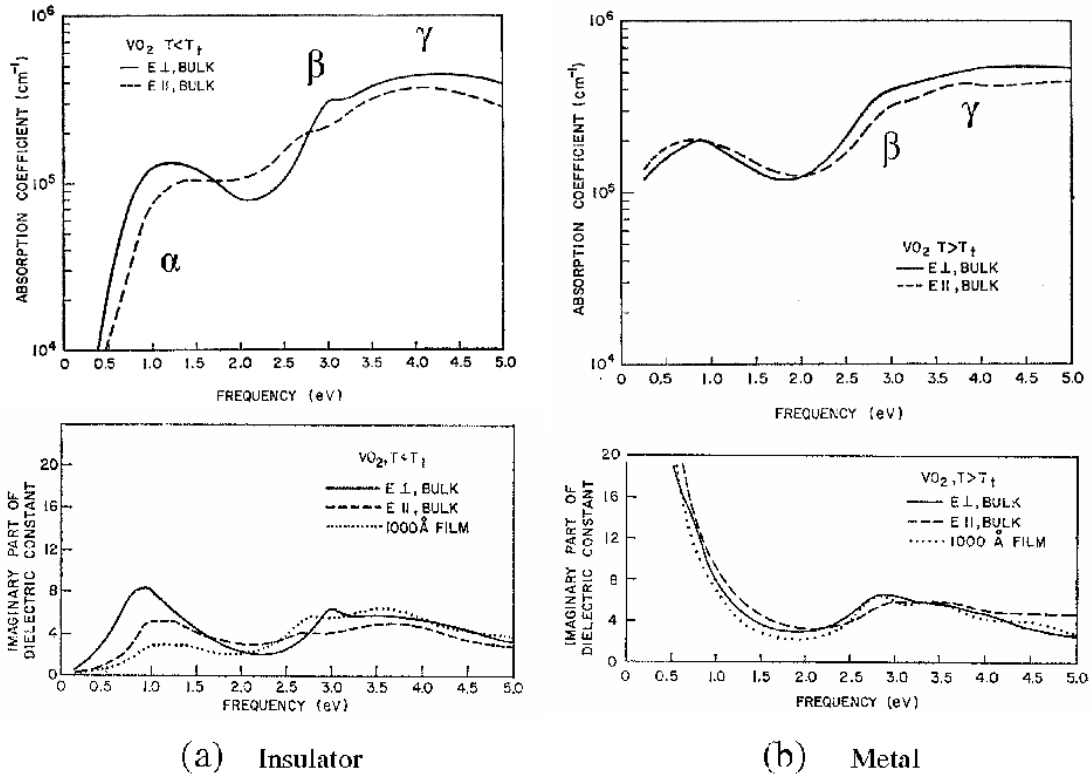

FIGURE 6.4: Absorption coefficient and imaginary part of the dielectric function of insulating (a) and metallic (b) VO_2 from a crystal sample (with polarization parallel, E$\|$, and orthogonal, E$\perp$, to the rutile c axis) and from a polycristalline film (dotted lines). α, β and γ indicate the band discussed in the text. From Ref. [87].

the frequency dependent dielectric function $\tilde{\epsilon}(\omega)$, and thus the real and the imaginary part of the complex refractive index $\tilde{n}(\omega)$ [87]. In figure 6.4 the absorption coefficient $\alpha(\omega) = 2k\omega/c$ and the imaginary part of $\tilde{\epsilon}(\omega)$, which is directly related to the optical conductivity $\sigma(\omega)$, for the insulating and the metallic phase are reported.

Three interband electronic excitations in the insulating monoclinic phase are clearly identified, beside of a slight anisotropy in the optical properties with polarization parallel (E$\|$) and orthogonal (E$\perp$) to the rutile c axis. The band at around 1 eV (labeled with α in figure 6.4) can be ascribed to the electron excitation from the bonding $d_{\|}$ to the π^* band. The optical gap edge is well define at around 0.6 eV. The high energy absorption at about 3.5 eV (γ) and 2.7 eV (β) were both originally ascribed to a charge-transfer excitation from the oxygen $2p$ levels to the vanadium π^* empty

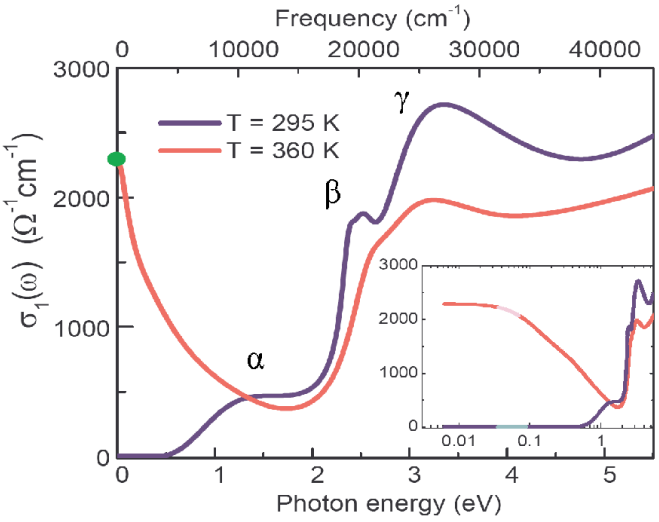

FIGURE 6.5: Optical conductivity of a 1000Å VO_2 film on Al_2O_3 substrate obtained from reflectivity measurements from Ref. [109]. α, β and γ indicate the band discussed in the text. Inset: the same data shown in a logarithmic scale in eV.

band. On increasing the temperature above T_{IM} a remarkable increase of the absorption in the low frequency side occurs. The α absorption band disappears, while the imaginary part of $\tilde{\epsilon}(\omega)$ shows a steep rise, ascribed to the free carriers response. An energy shift of about 0.5 eV to lower energy is shown by the γ band, that can be ascribed, in the scenario traced in section 2.3.4, to the shift of the π^* band due to the structural transition. On the contrary the β band does not shift on crossing T_{IM}. This result seems to invalidate the assignation of this peak to a charge transfer and a proper interpretation is still lacking.

A recent paper published on Science confirms previous results [109, 161, 162], but no direct comparison with band calculations accounting for electronic correlation have been performed yet. In figure 6.5 VO_2 optical conductivity $\sigma(\omega)$, obtained from reflectivity data, of a 1000Å VO_2 film on Al_2O_3 substrate at 295 K and 360 K from Ref. [109] is reported in the 0-5 eV frequency range. In the insulating phase the three band previously discussed above are quite evident. In the metallic phase the γ band shows a shift of about 0.5 eV to lower frequencies, while the β band does not move. In addition to the disappearance of the α band, it is clearly visible that the γ and the β bands lose intensity in favour of the free carriers Drude peak. The spectral weight (i.e. the frequency integrated optical conductivity) is recovered at a

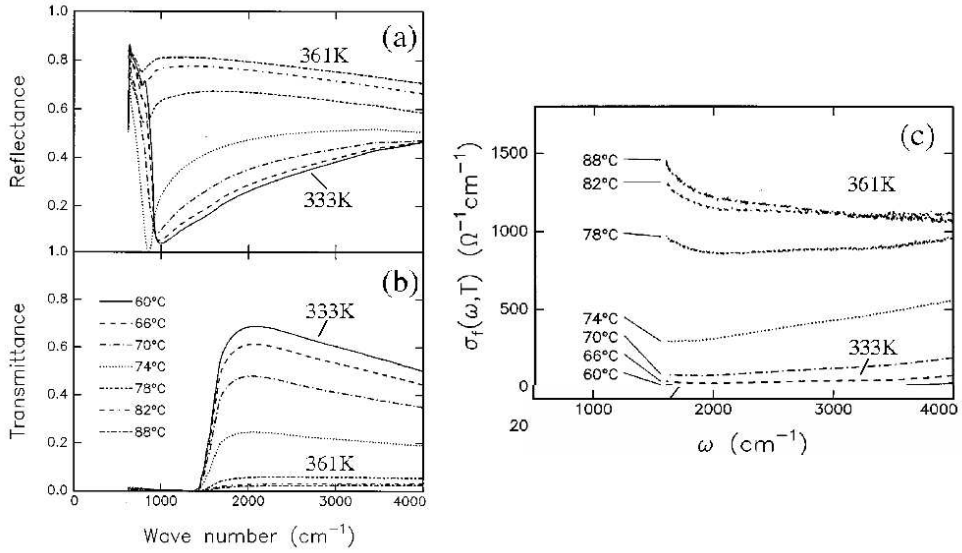

FIGURE 6.6: Mid infrared reflectance (a) and transmittance (b) as a function of temperature of a 1500Å VO_2 polycristalline film on sapphire substrate. In c: extracted optical conductivity as a function of temperature. From Ref. [88].

broad energy scale ($\gtrsim$5.5 eV). Data quality allowed for a detailed analysis of the free carriers Drude peak, which shows a 2.75 eV plasma frequency and persists at high temperature (at least up to 550 K). The "optical resistivity" $\rho = 1/\sigma(\omega \to 0)$ as a function of temperature shows an anomalous linear behaviour without any saturation, in agreement with DC resistivity measurements [89]. A carefull analysis of these data indicated that in the metallic state of VO_2 correlated charge carriers can not be treated as conventional Landau quasiparticles [109].

The temperature dependence of the optical properties of VO_2 close to T_{IM} has been carefully investigated in the mid-infrared frequency region. These results are reported here for a direct comparison with the mid-infrared data of the present work. In figure 6.6 a and b, reflectance R and transmittance T as a function of temperature of a 1500Å VO_2 polycristalline film on sapphire substrate are reported from Ref. [88]. Since the film is insulating at low temperature and the light is able to penetrate the VO_2 thin layer, the overall features of R and T spectra at the lowest temperature (333 K) are mainly determined by the sapphire substrate. As the temperature increases, R gradually increases and T decreases, the modification being complete well above T_{IM}.

The optical conductivity $\sigma(\omega)$, obtained exploiting the simultaneous measurements of R and T, is very small at 361 K, and shows an almost flat shape

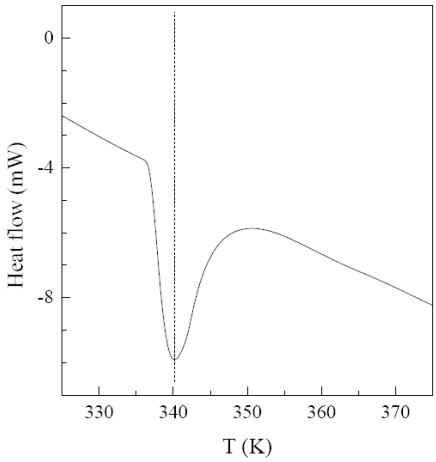

FIGURE 6.7: Heat own as a function of temperature of the VO2 sample studied in the present work

(see figure 6.6c). On increasing the temperature a gradual overall increase of $\sigma(\omega)$ occurs, and the metallic shape is completely achieved at 333 K, where $\sigma(\omega)$ is in good agreement with results reported above (see figure 6.5). These results have been interpreted in terms of phase separation, which can be responsible, at least in part, for the hysteresis in the resistivity. The same statement was already reported in Ref. [87].

6.2 Synthesis and characterization of VO_2 samples

Pure VO_2 synthesis was carried out in collaboration with Dr. L. Malavasi of the Physical Chemistry Department of the University of Pavia (Italy). VO_2 was prepared starting from proper amounts of V_2O_3 and V_2O_5 (Aldrich >99.9%) pressed in form of pellet and reacted at 1050°C in an argon flux for 12 h. Small crystals were obtained. Phase purity was checked through single crystal x-ray diffraction on some crystals and also on a powdered sample from crushed crystals. The room temperature refined lattice parameters are in both cases in full agreement with the M1 monoclinic structure. The metal to insulator transition in synthesized samples has been probed by means of Differential Scanning Calorimetry (DSC) which revealed a clear endothermic peak at about 340 K in perfect agreement with the literature T_{IM} value (see figure 6.7).

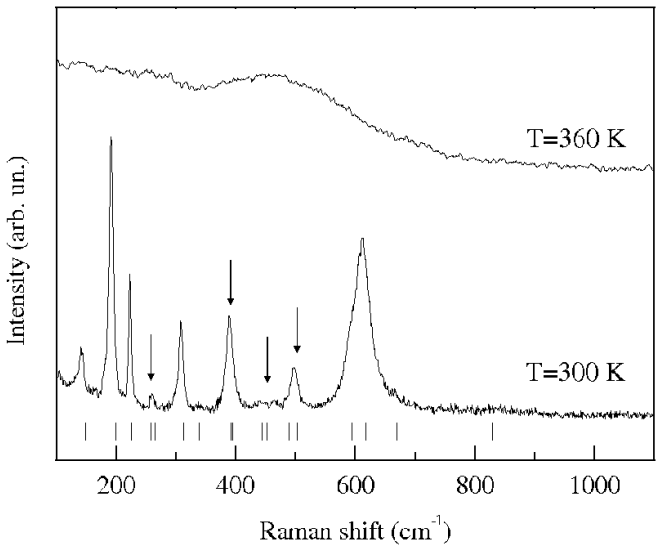

FIGURE 6.8: Raman spectra of a VO_2 crystal in the monoclinic (M1) and rutile (R) phase. Vertical bars mark the phonon frequencies from Ref. [158]. Arrows mark the not resolved structures.

VO_2 oxygen isotope substitution

Isotope oxygen substitution on VO_2 was carried out in collaboration with Dr. E. Pomjakushina and Dr. K. Conder of the Paul Sherer Institute (Swiss). Oxygen exchange has been performed on V_2O_5 (Puratronic 99.995%), then, by hydrogen reduction, stoichiometric V_2O_3 has been obtained. VO_2 has been syntered by mixing proper amounts of V_2O_5 and V_2O_3 and annealing at 775°C, for 50 h in closed quartz ampoules. The oxygen content and phase purity of the samples have been tested using hydrogen reduction on thermobalance and X-ray powder diffraction, respectively. In order to assure credibility of the oxygen isotope effect measurements, the synthesis procedure was parallel performed for ^{16}O- and ^{18}O- samples. As we will see in the following Raman spectra carried out on the two ^{16}O- and ^{18}O- samples demonstrate the complete substitution.

Raman spectra of $V^{16}O_2$ and $V^{18}O_2$ at ambient pressure

Ambient pressure Raman spectra of a pure VO_2 single crystal and powdered sample from crushed crystals have been collected as a function of temperature below and above the transition temperature T_{IM} = 340 K using the experimental setup described in 3.2 section. Results at ambient temperature (300 K) and at 360 K are shown in figure 6.8 as an example.

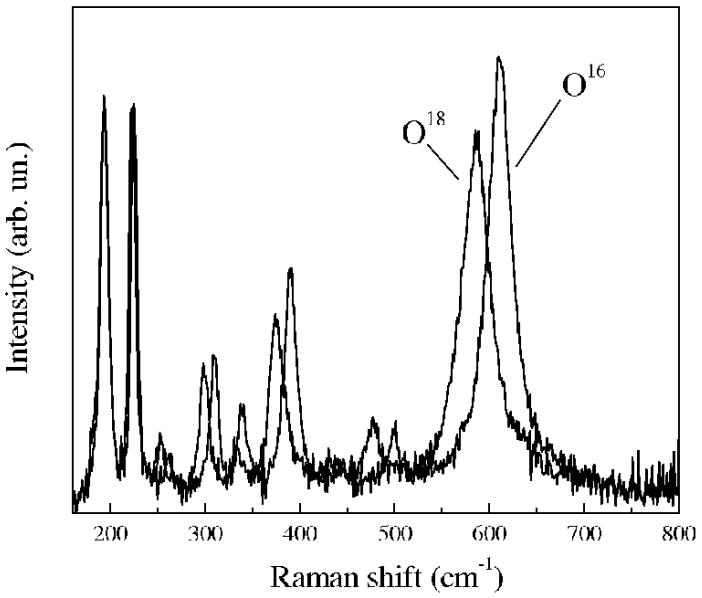

FIGURE 6.9: Comparison between room temperature Raman spectra of $V^{16}O_2$ (red dashed line) and $V^{18}O_2$ (full black line).

In agreement with previous data ([157,158]), in the rutile phase (T>340 K) only broad bands can be identified (at around 550 cm^{-1} and 250 cm^{-1}). The spectra in the monoclinic phase are in good agreement with previous data from Ref. [158] (see vertical markers in figure 6.8), although some doublets, marked with arrows in figure 6.8, are not resolved.

Since, as reported in previous section, polarization can modify the relative intensities of the peaks in monoclinic VO_2, preliminary Raman measurements of a single crystal have been collected on varying the direction of the laser polarization, in order to possibly resolve hidden peaks.

Measured spectra were fitted by using the standard model curve [132] discussed in chapter 4. Phonon frequencies obtained in the present work for monoclinic (M1) VO_2, listed in Table 6.1, are in good agreement with data from Ref. [158], also reported, collected at T=83 K.

Due to the large difference between the mass of V and O atoms, the lowest frequency peaks can be ascribed to the V-ions motion within the V-V chains whereas the high frequency modes at around 600 cm^{-1} can be ascribed to mixed V-O modes. A direct evidence of this assignment can be found by simply comparing the spectra of monoclinic VO_2 with ^{16}O and ^{18}O as shown in figure 6.9. It is well evident that the ^{18}O isotope substitution leads to a shift of all the phonon peaks, but the two at 191 cm^{-1} and 224

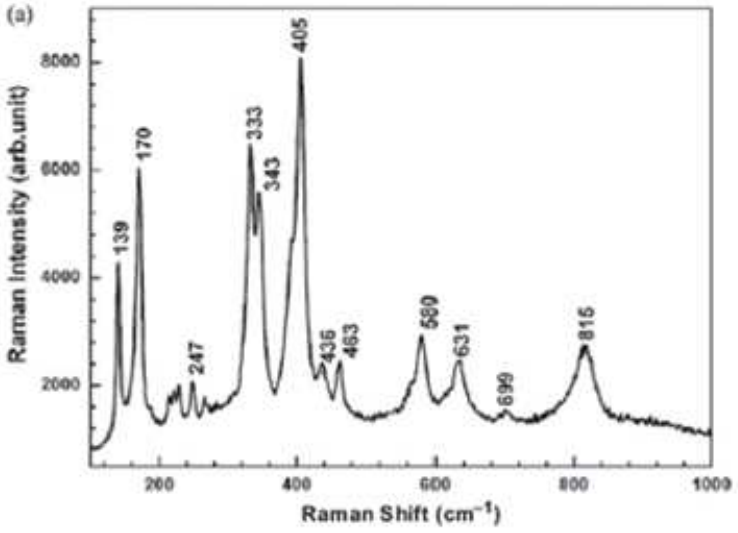

FIGURE 6.10: Raman spectrum of NbO_2, after ref. [164]

cm^{-1} (ω_{V1} and ω_{V2}), which can thus be assigned to V-V modes. The most affected structure is the mode at 613 cm^{-1} (ω_0), which shifts to 585 cm^{-1} in the ^{18}O substituted sample. Since the measured frequency scales well with the reduced mass between the oxygen and the vanadium, this mode can be assigned to a V-O mode. In addition, the same scaling laws are observed comparing the phonon frequencies of monoclinic VO_2 with those of NbO_2, which has the same crystal structure and exhibits a quite similar Raman spectrum [164] (see figure 6.10).

	Present work	Ref. [158]		Present work	Ref. [158]		Present work	Ref. [158]
1	142	149	8	391	392	14	596	595
2	191	199	9	-	395	15	613	618
3	224	225				16	670	670
			10	443	444	17	830	830
4	260	259	11	460	453			
5	-	265						
			12	497	489			
6	309	313	13	-	503			
7	339	339						

TABLE 6.1: Comparison of Raman phonon modes identified in monoclinic VO_2 in the present work, with data from Ref. [158].

6.3 VO_2 at high pressure

In order to shed more light on the subtle interplay between Peierls and MottHubbard mechanisms with respect to the MIT, Raman and infrared spectra of VO_2 has been collected, as a function of pressure at room temperature. Fully exploiting these two techniques, an interesting comparison of pressure-induced effects on both the electronic and the lattice dynamics has been made. Moreover, since the Raman spectrum of the rutile phase differs completely from that of the monoclinic phase, Raman spectroscopy allows to easily identify the lattice symmetry (monoclinic or rutile) of a VO_2 sample loaded in the diamond anvil cell.

6.3.1 High pressure Raman measurement on VO_2

Raman measurements of a small VO_2 ($\approx$ 10x10x10μm^3), loaded in the screw clamped DAC together with NaCl as hydrostatic medium, have been carried out as a function of pressure up to 19 GPa, using the experimental apparatus described in 3.2 section. The strong elastic contribution introduced by the employment of the DAC prevents data reliability below 150 cm^{-1}. Raman spectra of room temperature VO_2, collected within the 150-800 cm^{-1} frequency range, are shown in figure 6.11 at selected pressures. A moderate diamond fluorescence background is evident in collected spectra, which however does not affect the data quality. The spectrum at the lowest pressure shows a good agreement with the data collected on VO_2 at ambient conditions. On increasing the pressure a clear hardening of the phonon frequencies occurs, which, however, does not significantly changes neither the peak pattern nor the overall spectral shape over the pressure range explored. It is worth to notice that on increasing the pressure the peak at 391 cm^{-1} at P=0 splits in two components showing different pressure rates. This result is in agreement with data from Ref. [158], indicating two almost degenerate modes at P=0 at 392 cm^{-1} and 395 cm^{-1}. Variations of the relative intensities of phonon peaks must be ascribed to different polarization configurations due to different sample orientations at different pressures. Since the Raman spectrum of VO_2 in the R phase is characterized by only 4 broad bands it can be safely concluded that a transition to a R phase is not achieved by applying pressure up to 19 GPa.

At each pressure the diamond fluorescence background has been measured and was included in the fitting model. The intensity of the diamond background was treated as a free fitting parameter. Best fit of VO_2 Raman spectrum at P=0.2 GPa is shown in figure 6.12 as an example. The analysis shows an almost linear and regular increase of the frequencies of every

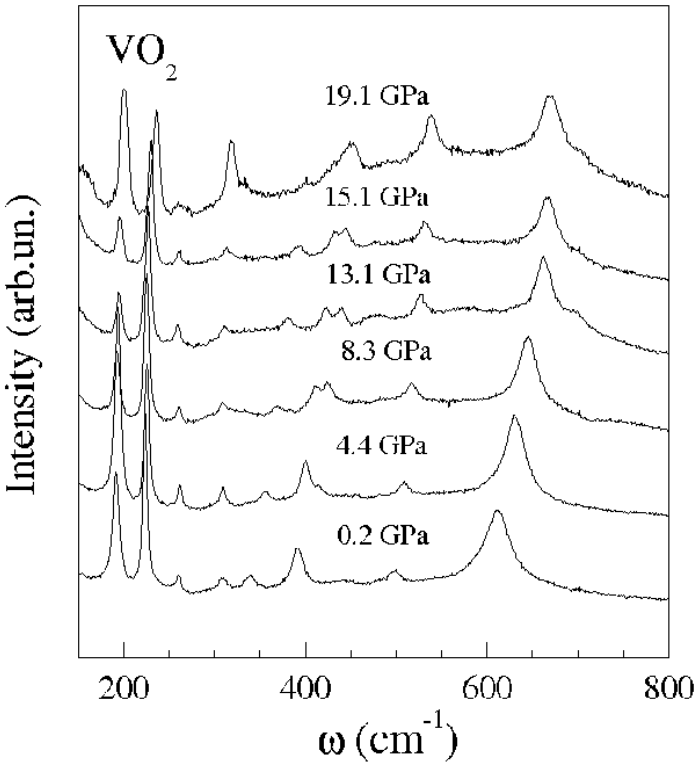

FIGURE 6.11: Room temperature Raman spectra of a small VO_2 crystall in a diamond anvil cell, at selected pressures.

phonon peak except for the two modes ω_{V1} and ω_{V2} at 192 cm^{-1} and 224 cm^{-1} at P=0 (see figure 6.11), which were previously assigned to V-V modes. In figure 6.13 the pressure dependence of the ω_{V1} and ω_{V2} modes (panel a) and of the ω_O intense peak at 613 cm^{-1}, ascribed to a V-O mode, (panel b) are shown. The two low frequency modes show a rather abrupt change of the pressure rate $d\omega/dP$ from a value close to zero to 1-1.5 cm^{-1}/GPa around 10 GPa. On the contrary the ω_O mode, as well as all the other modes, shows a regular hardening ($d\omega/dP \approx 4$ cm^{-1}). While the monoclinic phase retains up to 19 GPa, the present result suggests a subtle rearrangement of the V-V chains distortion occurring at 10 GPa.

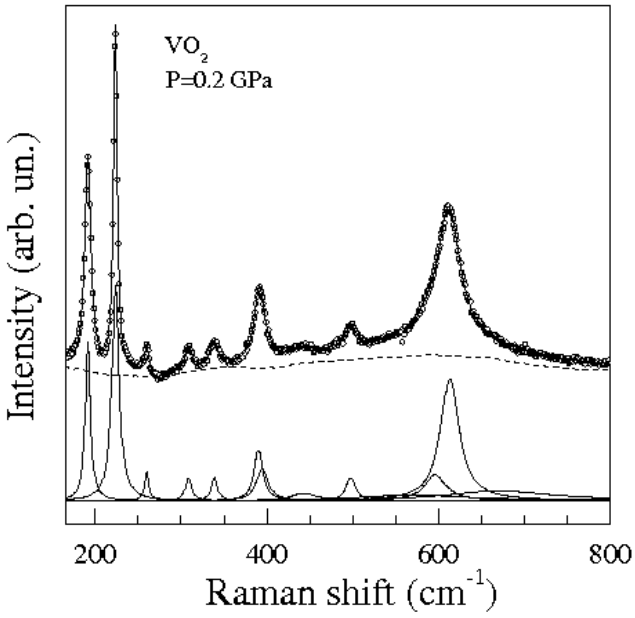

FIGURE 6.12: Room temperature Raman spectrum of VO_2 in the diamond anvill cell at 0.2 GPa (open circles) and best fit (full line). DHO phonon contributions (full lines) and diamond background (dashed line) have been reported.

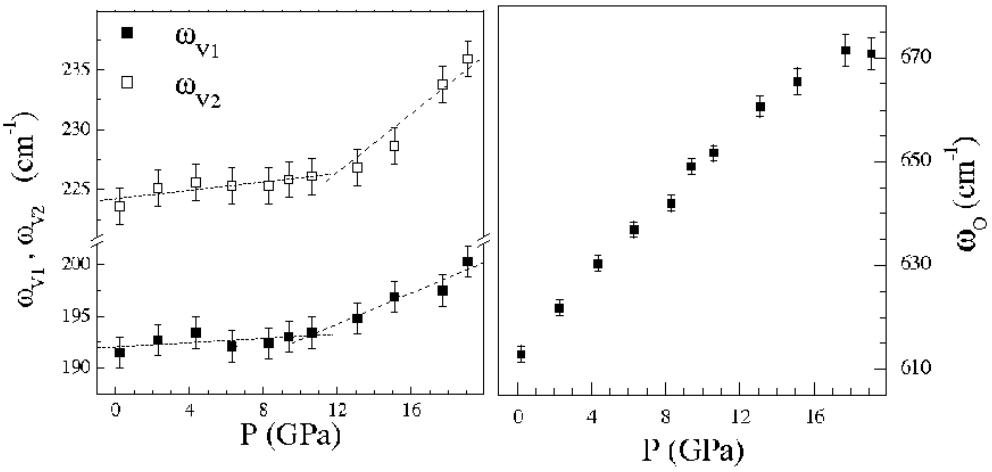

FIGURE 6.13: In (a), pressure dependence of the two low frequency modes ω_{V1} and ω_{V2} of VO_2; in (b), pressure dependence of the V-O mode ω_{VO} of VO_2 . Dashed lines are guides for the eyes.

6.3.2 High pressure infrared measurements on VO_2

High-pressure IR spectra of room temperature VO_2 have been collected exploiting the high brilliance infrared source of the SISSI beamline at Elettra, within the 750-6000 cm^{-1} frequency range, using the experimental setup described in 3.3 section. A VO_2 5μm thick slab, obtained by pressing finely milled sample powder between the diamond anvils, has been placed in the gasket hole, where a KBr pellet was previously sintered. The slits of the microscope were carefully adjusted to collect transmitted and reflected light from the sample only and kept fixed for all the experiment. The high brilliance of the infrared synchrotron source and the proper sample thickness allowed the simultaneous measurement of both reflectivity and transmittance at each pressure. Reflectivity $R(\omega)$ and transmittance $T(\omega)$ spectra at selected pressures are shown in figure 6.14. We notice that within the 1600-2600 cm^{-1} frequency range, strong diamond absorption prevents data reliability, that are replaced by dashed lines.

At P$\sim$0, the low-frequency reflectivity is characterized by a steep rise due to a phononic contribution, whereas, on the high frequency side, $R(\omega)$ is slowly varying between 0.05 and 0.08. These values are slightly higher than those expected for sample-diamond interface, on the basis of the known optical properties of diamond [163] and VO_2 [87]. The extra reflectivity is due to the multiple reflections within the sample-KBr bilayer which also originate the interference fringes well evident in both $R(\omega)$ and $T(\omega)$ (see Appendix B). For clarity, fringes have been averaged out in high pressure reflectivity spectra reported in figure 6.14. The low $T(\omega)$ values at high-frequency are due to the absorption of the low-frequency tail of the lowest energy electronic band [87, 109].

Within the 0-10 GPa pressure range, $R(\omega)$ does not change remarkably whereas $T(\omega)$ gradually decreases. On increasing pressure above 10 GPa $R(\omega)$ starts to increase and $T(\omega)$ abruptly decreases to very small values owing to the shift of the electronic band toward lower frequencies. The optical density $O_d(\omega) = -\ln T(\omega)$ shown in the inset of figure 6.14, makes evident this process: above 10 GPa the electronic contribution fills the optical gap and the phonon peak is remarkably screened, thus showing the onset of a pressure induced charge delocalization process.

The simultaneous measurements of $R(\omega)$ and $T(\omega)$ enable to extract the real, $n(\omega)$, and the imaginary part, $k(\omega)$, of the complex refractive index of VO_2. To this purpose, thanks to the present loading procedure, a multilayer scheme diamond-sample-KBr-diamond has been adopted, where multiple reflections within the sample and the KBr layers have been accounted for by adding incoherently the intensities of the reflected beams [147]. Using

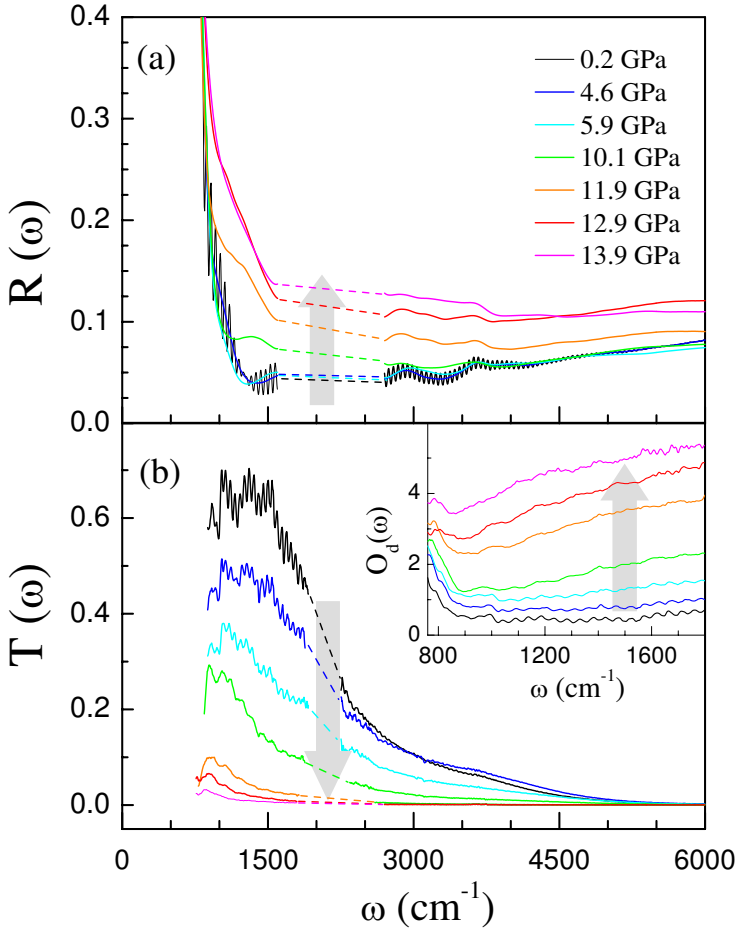

FIGURE 6.14: (a) MIR reflectivity $R(\omega)$ and (b) transmittance $T(\omega)$ of VO_2 at selected pressures. Fringes have been averaged out in the reflectivity spectra, except at the lowest pressure. Arrows indicate increasing pressure. Dashed lines replace the data at the frequencies where the diamond absorption is very high. Inset: correspondingly low-frequency optical density $O_d(\omega)$.

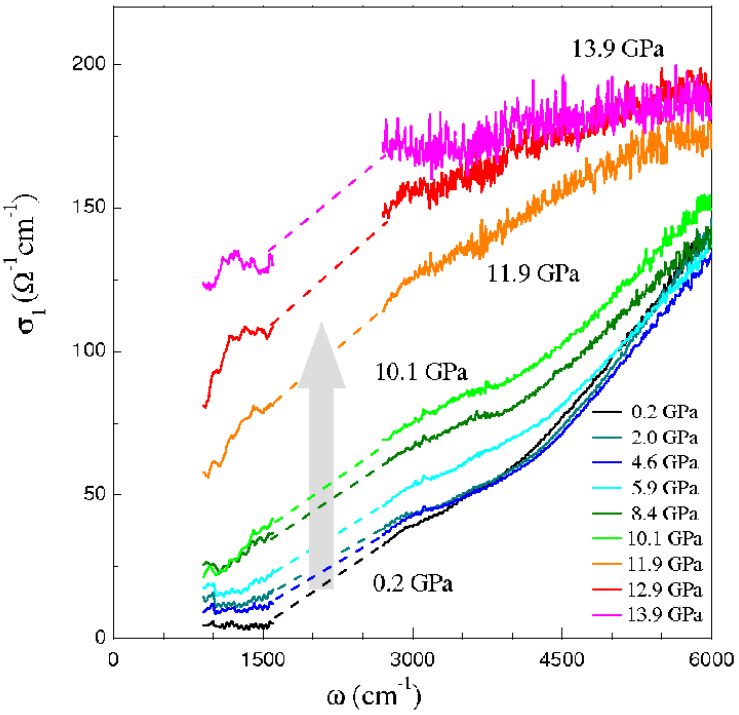

FIGURE 6.15: Optical conductivity $\sigma(\omega)$ of VO_2 at different pressures. Dashed lines are guides to the eyes. Arrow indicates increasing pressure.

the experimental layer thicknesses and the known optical properties of diamond [163] and KBr [165], $R(\omega)$ and $T(\omega)$ can be expressed as a function of $n(\omega)$ and $k(\omega)$ only. The analytical derivation is reported in Appendix B, where the numerical iterative procedure adopted for solving the non-analytical two equations system to obtain $n(\omega)$ and $k(\omega)$ is also reported. The results obtained at the lowest pressure have been found to be in good agreement with literature data at P=0 [87, 109]. The independence of the results from the guess function have been checked and a complete agreement is found when the different calculation technique from Ref. [88] is adopted.

The optical conductivity $\sigma(\omega) = 2\omega/4\pi \cdot n(\omega)k(\omega)$ at different pressures is shown in figure 6.15.

The low frequency region of the spectra has not been reported because the strong variations of the optical constants around the phonon contribution could affect the reliability of the iterative procedure. The data shown in figure 6.15 allow to follow the pressure behavior of the low frequency tail of the electronic band, which, bearing in mind the transfer of spectral weight from the metallic to the insulating phase [109], is the spectral region mostly affected by the MIT.

At P∼0, $\sigma(\omega)$ is in good agreement with recent ambient pressure data [109] and it is weakly pressure dependent up to 4 GPa. On further increasing the pressure, $\sigma(\omega)$ progressively increases, mainly within the 1500-4500 cm^{-1} frequency range. Above 10 GPa an abrupt increase of the overall $\sigma(\omega)$ occurs and a remarkable pressure-induced band gap filling is observed. The data at the highest pressure clearly show that the energy gap, if still open, is well below 900 cm^{-1}. We want to notice that a rough linear extrapolation of the data collected at P>10 GPa gives positive, although small, $\sigma(\omega \rightarrow 0)$ values compatible with a bad metal behavior.

The effect of pressure can be better visualized if the pressure dependence of the spectral weight SW(P) is analyzed. At each pressure we calculated the integral of $\sigma(\omega)$ over the 900-1600 cm^{-1} [SW_L(P)] and 2600-5000 cm^{-1} [SW_H(P)] frequency ranges:

$$SW_L(P) = \int_{900cm^{-1}}^{1600cm^{-1}} \sigma(\omega, P)d\omega \qquad SW_H(P) = \int_{2600cm^{-1}}^{5000cm^{-1}} \sigma(\omega, P)d\omega.$$

The integration has not been extended to the frequency region above 5000 cm^{-1}, owing to the onset of saturation effects in the spectra collected at the highest pressures (see in figure 6.15 the high noise level at high frequencies). The spectral weights normalized to the lowest pressure values, SW^*_L(P)=SW_L(P)/SW_L(P_{min}) and SW^*_H(P)=SW_H(P)/SW_H(P_{min}) are shown in figure 6.16.

Both the spectral weights show the same pressure dependence, with a clear and abrupt change of slope at 10 GPa. We notice that the absolute pressure-induced variation of SW^*_L(P) is much larger than that observed for SW^*_H(P), as expected if charge delocalization occurs [109]. Such a large and abrupt increase of the spectral weight in the gap region is certainly compatible with the occurrence of a pressure induced MIT, although the spectral range of the present measurements does not allow to claim undoubtedly the complete optical gap closure above 10 GPa.

6.4 Synthesis and characterization of Cr-doped VO_2 samples

The synthesis of Cr-doped VO_2 samples have been carried out in collaboration with Dr. L. Malavasi of the Physical Chemistry Department of the University of Pavia (Italy). $V_{0.975}Cr_{0.025}O_2$ and $V_{0.993}Cr_{0.007}O_2$ powder samples, in the M2 and M3 monoclinic insulating phase, respectively, at ambient conditions (see phase diagram in figure 6.17), have been synthesized starting

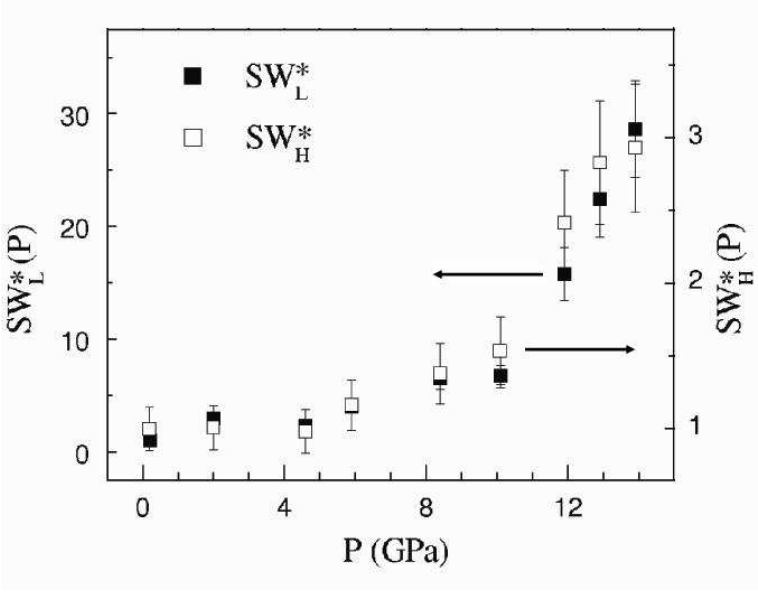

FIGURE 6.16: Normalized spectral weights in the low frequency, $SW_L^*(P)$, and high frequency region, $SW_H^*(P)$. Notice the two y-axis!

from equimolar amounts of V_2O_3 and V_2O_5 and adding proper stoichiometric amounts of Cr_2O_3. The mixture have been fired at 1000°C under an argon atmosphere. Phase purity was checked through x-ray powder diffraction. Transition temperatures obtained from DSC measurements are in good agreement with literature data [98].

Raman spectra of $V_{1-x}Cr_xO_2$ at P=0

Room temperature Raman spectra of 2.5% and 0.7% Cr-doped VO_2 samples, in the M2 and M3 monoclinic phase respectively, are shown in figure 6.18, compared with the undoped sample, in the M1 phase.

Cr-doped samples show peaks patterns very similar to that of the pure compound, but with different phonon frequencies, in agreement with group theory, which predicts the same number of Raman-active modes (10 Ag + 8 Bg) for both the M2 and the M3 phase. Great care have been used in order to avoid the heating of powdered samples during measurement. In particular the laser power have been reduced of two order of magnitude to collect Raman spectrum of the 0.7% Cr-doped sample in the M3 phase. As a matter of fact on increasing the laser power (i.e. on increasing the temperature) a reversible transition into the M2 phase occurs, due to the closeness of the M3 to M2 phase transition (see figure 6.17). Under these conditions this sample shows the same spectrum of the 2.5% Cr-doped sample. No sensible difference has

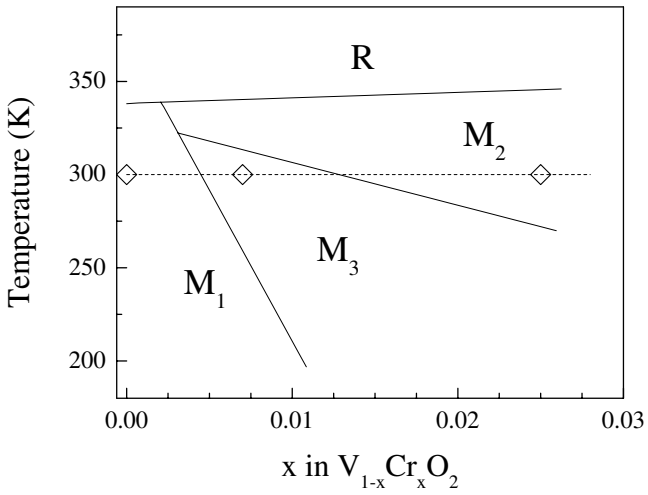

FIGURE 6.17: $V_{1-x}Cr_xO_2$ phase diagram as a function of temperature and Cr concentration x from Ref. [98]. Open symbols indicate the pure compound and the two Cr-doped samples studied in the present work.

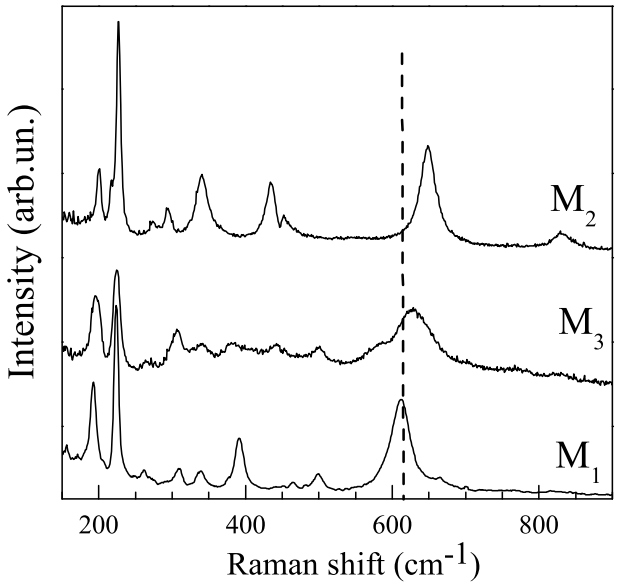

FIGURE 6.18: Comparison among $V_{0.975}Cr_{0.025}O_2$ (in the M2 phase), $V_{0.993}Cr_{0.007}O_2$ (in the M3 phase) and pure VO_2 (in the M1 phase) room temperature Raman spectra.

been observed in the high temperature rutile Raman spectrum of all the three samples. Looking at figure 6.18 it is quite evident that the V chains

modification in the M2 and M3 phase with respect to the M1 configuration leads to a general shift of all the phonon modes. Focusing our attention to the two low frequency mode ω_{V1} and ω_{V2}, ascribed to the V motion only, a moderate hardening of the ω_{V1} mode in the M3 and M2 phases is apparent and a low frequency extra peak due to the splitting of the peak at about 225 cm^{-1} appears in the M2 phase (see inset of figure 6.18). The ω_O mode shows a well pronounced hardening, its frequency moving from 613 cm^{-1} in the M1 phase to 629 cm^{-1} and 644cm $^{-1}$ in the M3 and M2 phase respectively. It is a worth to notice that the same shift of the ω_O and ω_{V1} peaks shown in the 2.5% doped sample has been previously observed in nonstoichiometric VO_2 samples, as reported in reference [167]. This finding suggests that the V^{3+} or V^{5+} presence in nonstoichiometric VO_2 stabilizes the M2 phase, as well as the Cr impurities.

6.5 High pressure Cr-doped VO_2

6.5.1 High pressure Raman measurements on Cr-doped VO_2

Room temperature Raman spectra of 2.5% and 0.7% Cr-doped VO_2 powder samples have been collected as a function of pressure up 14 GPa in the same experimental setup of high pressure undoped sample measurements, described in section 3.2. Results are reported in figure 6.19 at selected pressures. Since the signal of powder samples is lower with respect to crystal samples, the diamond fluorescence contribution to the collected spectra is more pronunced. For clarity, diamond background contribution obtained by the best fit of the data has been subtracted in the spectra reported in figure 6.19.

High pressure does not significantly change the peak pattern and the general spectral shape over the whole pressure range explored on both the samples. Small variation on the relative intensities of phonon peaks must be ascribed to polarization effects. While on applying pressure on the pure (M1) VO_2 a clear and regular hardening of the phonon frequencies occurs, the effect of pressure on M2 and M3 samples is more complex. Indeed, on increasing the pressure the Raman spectra of both the Cr-doped samples gradually evolve toward that of the undoped sample. Above 3 GPa the 0.7% Cr-doped sample shows the same Raman spectrum of the undoped sample at the same pressure, and, at 9 GPa, the Raman active phonon spectra of all the three samples coincide at P≈9 GPa (see figure 6.20), and evolve together on further increasing the pressure.

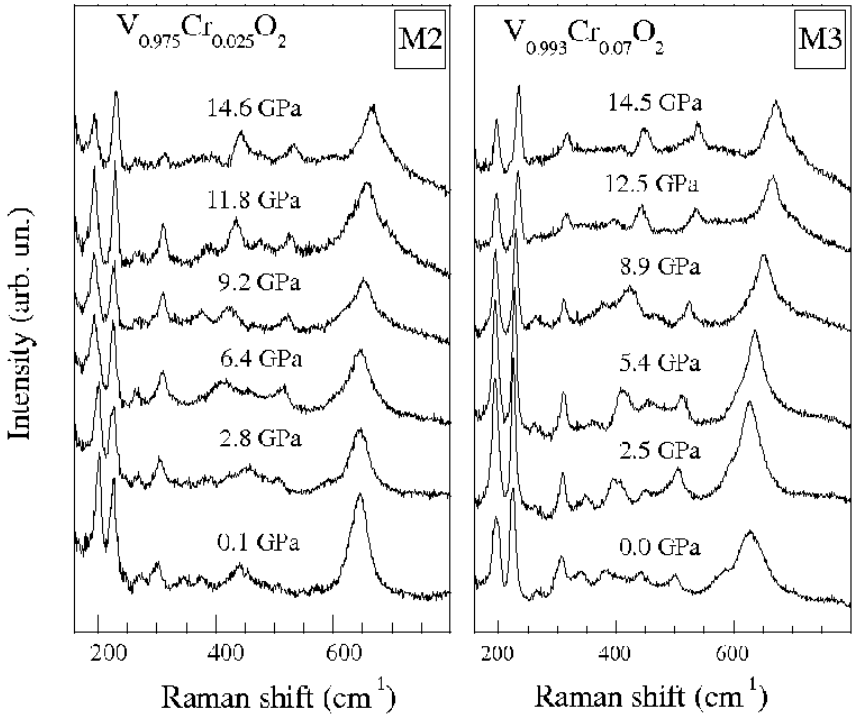

FIGURE 6.19: $V_{0.975}Cr_{0.025}O_2$ and $V_{0.993}Cr_{0.007}O_2$ room temperature Raman spectra at selected pressures. Diamond background have been subtracted for clarity.

In the following the analysis of Raman spectra is restricted to the ω_{V1}, ω_{V2} and ω_O phonon modes, since they give clear information about the V-V and V-O modes, as discussed in the previous section. Best fit phonon frequencies of the two Cr-doped samples are shown in figure 6.21, compared with results for the undoped sample. In Cr-doped sample V-V and V-O modes show a remarkable anomalous pressure dependence. The high frequency mode ω_O shows a flat pressure dependence in both M2 and M3 samples, till it reaches the frequency of the pure VO_2, at around 3 GPa and 9 GPa in M3 and M2 sample, respectively. On further increasing pressure almost the same pressure dependence is observed in all the three samples. The pressure behavior of the low frequency mode ω_{V1} is also interesting, showing a clear softening in both the Cr-doped samples. In the 2.5% Cr-doped sample, for example, ω_{V1} changes from 200 cm^{-1} at P=0 to 190 cm^{-1} at P=9.3 GPa, where, as well as the ω_O mode, it coincides with the pure VO_2 value (figure 6.21 b). The ω_{V2} peak instead is almost constant up to 10 GPa in all the three samples.

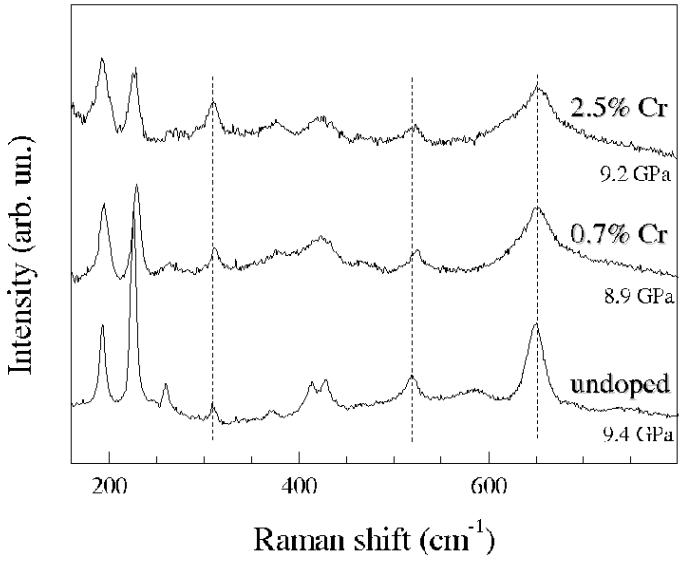

FIGURE 6.20: Comparison among the Raman spectra of 2.5% Cr-doped, 0.7% Cr-doped and pure VO_2 at about 9 GPa. Vertical lines are guides for the eyes.

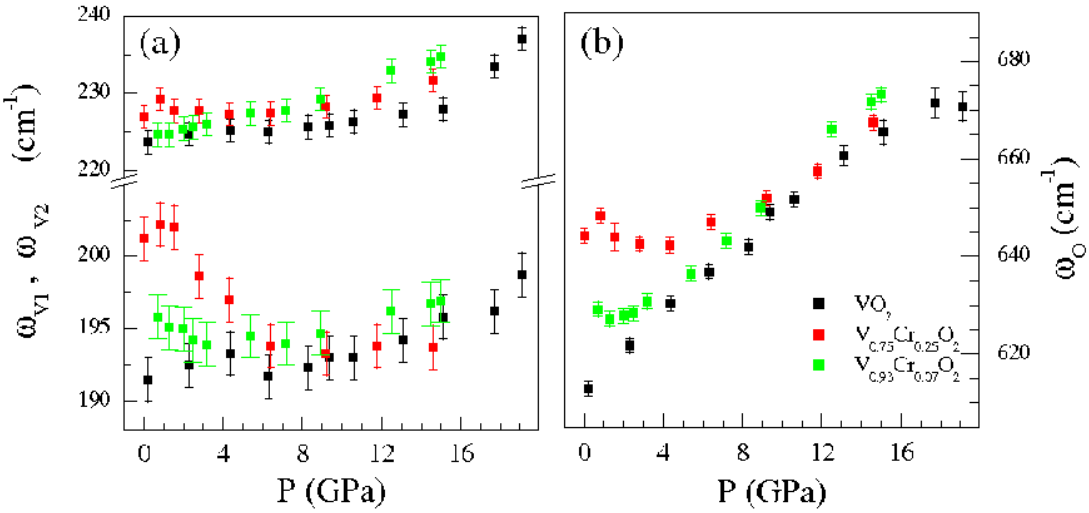

FIGURE 6.21: Comparison among phonon frequency of 2.5% Cr-doped, 0.7% Cr-doped and pure VO_2 as a function of pressure. In (a), pressure dependence of the two low frequency modes ω_{V1} and ω_{V2} of VO_2; in (b), pressure dependence of the V-O mode ω_{VO} of VO_2 .

On increasing the pressure above 10 GPa, a moderate hardening of ω_{V1} and ω_{V2} is apparent, in agreement with results obtained on pure VO_2.

These findings allow to identify three regimes for Cr-doped VO_2. In the low pressure regime, P< 3 GPa (P<9 GPa), the M3 (M2) structure of the 0.7 % (2.5 %) Cr doped sample gradually evolves towards the M1 monoclinic structure. The M1 phase common to the 3 samples retains up to about 10 GPa and, on further increasing the pressure, the hardening of ω_{V1} and ω_{V2} shows the occurrence of a subtle rearrangements of the V-V chains, still within the monoclinic framework. The last finding suggest the 3 samples enter a new monoclinic phase (Mx), slightly different from M1 phase.

6.5.2 High pressure IR measuremets on Cr-doped VO_2

Mid-infrared reflectivity $R(\omega)$ and transmittance $T(\omega)$ spectra of the 2.5% Cr-doped VO_2 (M2) as a function of pressure have been collected in the 750-6000 cm^{-1} frequency range, in the same experimental setup of the previous experiment on the pure compound, described in 3.3 section. A thin sample slab (3 μm) was loaded in the DAC with KBr hydrostatic medium. Results are shown in figure 6.22 at selected pressures.

The sample shows both reflectance and transmittance spectra rather similar to those of the undoped sample. We notice that the hump at about 3500 cm^{-1} is not related to the sample response, but is due to a bad compensation of the diamond absorption in this region. On increasing the pressure a gradual decrease of the transmittance occurs, while reflectivity is almost constant up to 10 GPa. On increasing the pressure above 10 GPa transmittance drops to very low values, while reflectance level starts to increase. As pointed out in discussing results for the undoped sample (Section 6.3.2), this is an evidence of charge delocalization, that can be better visualized by the optical density $O_d(\omega) = -\ln T(\omega)$, plotted in the inset of figure 6.22, which shows the electronic contribution filling the optical gap and screening the phonon peak.

The real and the imaginary part of the complex refractive index $\tilde{n}(\omega)$ of $V_{0.975}Cr_{0.025}O_2$ as a function of pressure have been achieved following the same analysis adopted for the pure compound. The optical conductivity $\sigma(\omega)$ at the different working pressure has been eventually achieved, and is shown in figure 6.23.

Looking at figure 6.23, the low frequency tail of the lowest energy electronic band is well evident in the lower pressure $\sigma(\omega)$ spectrum. Since the $\sigma(\omega)$ of $V_{0.975}Cr_{0.025}O_2$ is also rather similar to that obtained for the pure sample, we can argue that the lattice differences between M1 and M2 lattice structures due to the Cr-doping do not affect the low frequency elec-

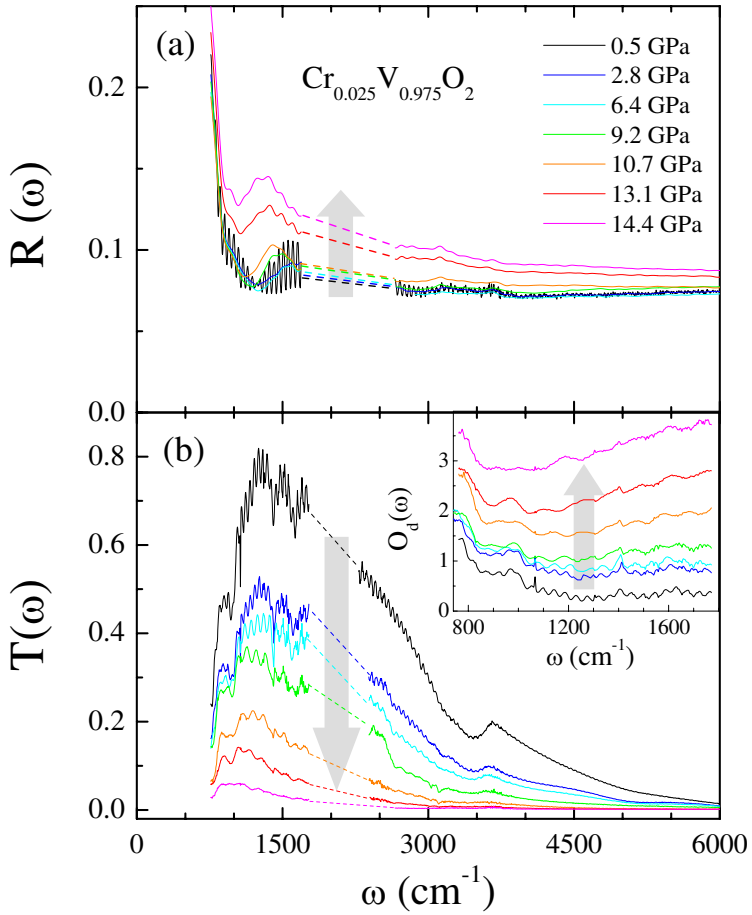

FIGURE 6.22: MIR reflectivity $R(\omega)$ (a) and transmittance $T(\omega)$ (b) of $V_{0.975}Cr_{0.025}O_2$ at selected pressures. Fringes have been averaged out in the reflectivity spectra, except at the lowest pressure. Arrows indicate increasing pressure. Dashed lines replace the data at the frequencies where the diamond absorption is very high. Inset: correspondingly low-frequency optical density $O_d(\omega)$.

tronic properties of VO_2 at ambient conditions. On increasing the pressure the gap filling process is quite evident and it can be quantitatively evaluated if the pressure dependence of the spectral weight is analyzed. At each pressure the $SW_L(P)$ and $SW_H(P)$ spectral weights have been obtained by integrating $\sigma(\omega)$ over the 1050-1700 cm^{-1} and 2700-5000 cm^{-1} frequency ranges, respectively. As well as for pure VO_2, the integration has not been extended to the frequency region above 5000 cm^{-1}, owing to the onset of saturation effects in the spectra (see 6.3.2 section). The spectral weights normalized to the lowest pressure values, $SW_L^*(P)=SW_L(P)/SW_L(0)$ and

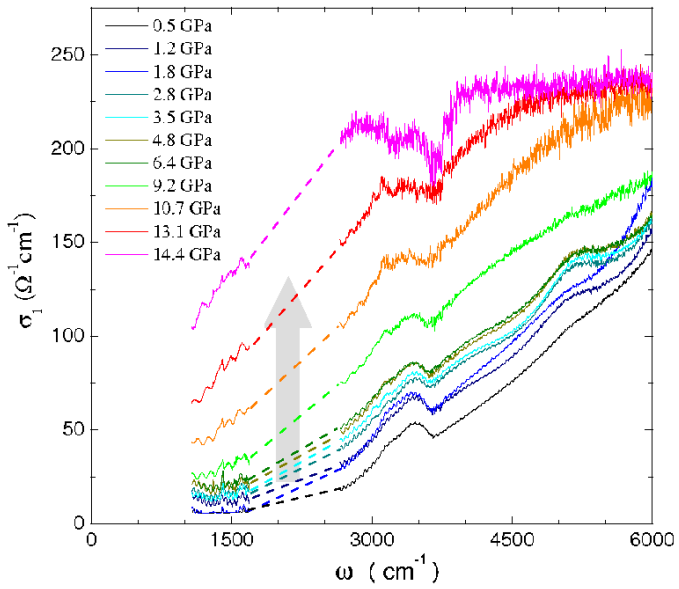

FIGURE 6.23: Optical conductivity $\sigma(\omega)$ of $V_{0.975}Cr_{0.025}O_2$ at different pressures. Dashed lines are guides to the eyes. Arrow indicates increasing pressure.

$SW_H^*(P)=SW_H(P)/SW_H(0)$ have been calculated. Results are shown in figure 6.24 (a) and (b) respectively, compared with the results on the undoped sample.

Low and high frequency spectral weights show the same pressure dependence, with a clear and abrupt change of slope at 10 GPa. It is worth to notice that, although a slight increase of the normalized spectral weight of the Cr-doped sample is already observed at low pressure, however the sharp and discontinuous increase of SW_L^* and SW_H^* occurs at the same pressure in both the samples. Moreover the quantitative effect of pressure on the normalized spectral weights is almost the same for both the samples. The absolute pressure-induced variation of $SW_L(P)$ is much larger than that observed for $SW_H(P)$ as expected if charge delocalization occurs. [109]

These results clearly pointed out that both the pure and the 2.5% Cr doped samples undergo a pressure induced metallization process at around 10 GPa.

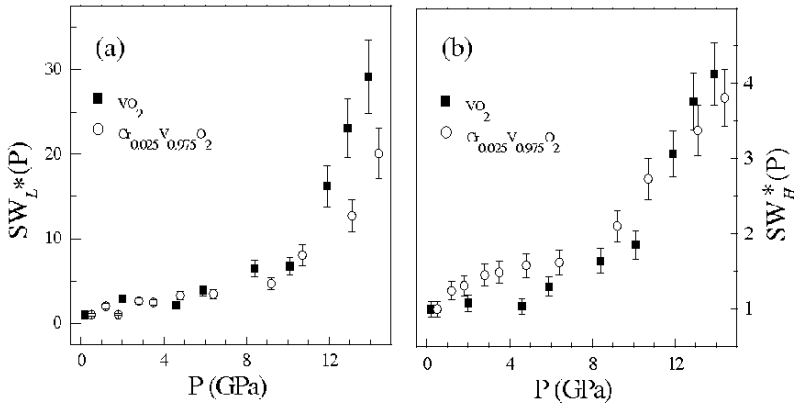

FIGURE 6.24: Comparison between the $V_{0.975}Cr_{0.025}O_2$ and undoped VO_2 normalized spectral weights in the low (a) and high frequency region (b) as a function of pressure. Notice the one order of magnitude difference in the y-scale.

6.6 Discussion

From the above results we can conclude that both the Cr-doped samples (M2 and M3 at ambient condition) undergo a pressure induced transition toward the high pressure M1 phase of VO_2. This transition is continuous and extends over a wide pressure range, starting at low pressure and being completed at P∼4 GPa and at P∼9 GPa for the 0.7% Cr-doped (M3) and 2.5% Cr-doped (M2) sample, respectively. On further increasing the pressure it appears that all the systems regardless the Cr-doping undergo a new monoclinic phase Mx, which shows a metallic behavior.

Since the Raman spectra of the 2.5% and 0.7 % Cr-doped samples (in the M2 and M3 phase respectively) show quite different phonon frequencies up to 9 GPa, our data do not support the claimed M2 to M3 transition [98] at low pressure (∼ 1.5 GPa). However, a weak anomaly can be envisaged in the low pressure behaviour of the phonon modes of the 2.5% Cr-doped sample (see figure 6.21).

The V ions pairing and their off-axis displacement causes an off-center displacement of the V ions within the rather stable oxygen octahedral cage. This affects the $p-d$-like V-O bonding and leads to two short and two long equatorial V-O bond lengths. A measure of the octahedral distortion can be for provided by the V-O bond lengths standard deviation from the average, which results to be smaller in the M3 than in the M2 phase [98]. Since the M2 and M3 phases have two types of V-V chains, while M1 has one type only, a direct comparison of the bond lengths is not possible. However in

the M1 phase the longest V-O distance (2.060 Å) is shorter than in M2 and M3 (2.127 Å and 2.105 Å, respectively), and the shortest (1.860 Å for M1) is longer (1.854 Å for M2 and 1.849 Å for M3) [86, 98]. This shows a reduction of the off-center displacement in going from M2 to M3 and to M1. Bearing in mind this point, our Raman results can be interpreted in terms of pressure induced octahedra symmetrization. Applying pressure M3 goes to M1 at 4 GPa and M2, which shows the largest octahedra distortion, goes to M1 at 9 GPa. On increasing the pressure above 10 GPa the anomaly in the pressure dependence of the ω_{V1} and ω_{V2} modes suggests a slight rearrangement of the V-V chains, leading to a common monoclinic phase Mx, in which the extent of the Peierls distortion requires to be further investigated.

The comparison between the infrared data of pure and 2.5% Cr-doped VO_2 shows that the partial removal of the V-V dimerization, characteristic of the M2 phase, does not sensibly affects the low frequency electrodynamics, since the two samples show rather similar low frequency optical conductivity $\sigma(\omega)$. Also the $\sigma(\omega)$ pressure behaviors are quite similar, except for slight differences in the spectral weights at low pressure (see figure 6.24). Two regimes below and above a threshold pressure P*$\sim$10 GPa can be clearly identified in both the samples. While for P<P* a weak pressure dependence in optical conductivity is observed (see figure 6.15 and figure 6.23), for P>P* a clear charge delocalization process occurs, quite remarkable at the highest pressures. The spectral shape and the $\sigma(\omega)$ values at low frequency at highest pressure show the achieving of a bad metallic behavior.

Bearing in mind the Raman data, the whole of these results indicate that, on increasing pressure, Cr-doped VO_2 enters the same lattice structure of the high pressure pure VO_2, in which the pressure enables a metallization process.

Combining high pressure Raman and infrared results we can outline a completely novel regime for room temperature VO_2 at high pressure, where the monoclinic to rutile and the insulator to metal transitions are decoupled. Indeed the observed pressure-induced metallization process occurs within the monoclinic lattice symmetry, which retains up to 19 GPa. Recent preliminary high-pressure x-ray diffraction data carried out by our group [166], which extend the stability of the monoclinic symmetry up to 42 GPa, further support the above statement. Furthermore an abrupt reduction of the volume of the unit cell has been observed on increasing pressure above 10 GPa, indicating the occurrence of a lattice instability within the monoclinic symmetry (Mx ?) [see panel a) of figure 6.25]. The availability of the pressure dependence of the phonon spectrum and of the unit cell volume enables us to calculate (according to equation 5.6) the Grüneisen parameters, γ_i, of the $i-th$ Raman active mode, ω_i. Providing a direct and quantitative measure of phonon

anharmonicity, an accurate determination of γ_i is very appealing at addressing the role of electron-phonon coupling in driving the physical properties of VO_2. The parameters are calculated using the finite differences method after extrapolating the $V(P)$ at each working pressure of the Raman experiment. On increasing pressure an overall reduction of γ_i values (typically from 2.5 to 1) is observed, except for the γ_1 and γ_2 values (see the inset of Figure 6.25) whose pressure behaviors appear discontinuous. The Grüneisen parameters associated to the ω_{V1} and ω_{V2} vibrations are indeed almost constant and close to zero (harmonic limit) within 0-10 GPa. On further increasing the pressure they start to linearly increase up to about 2.5 at 19 GPa. This scenario is consistent with the rearrangement of V atoms along the chains, which increases the anharmonic character of the V-V vibrations through the activation of some kind of phonon interactions.

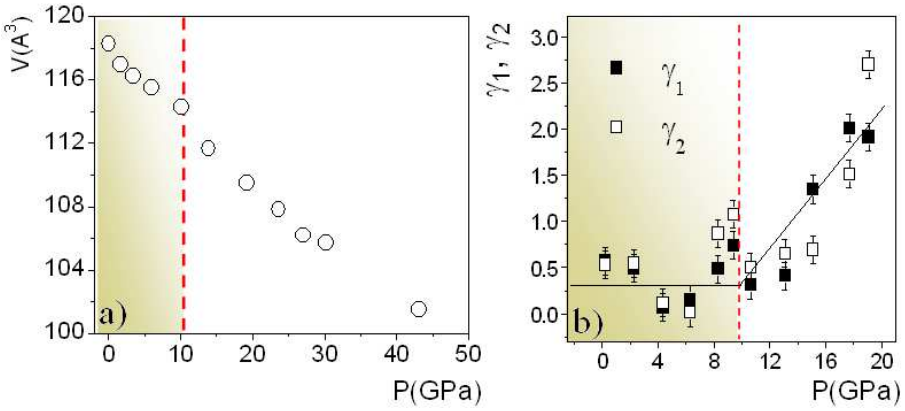

FIGURE 6.25: Unit cell volume [panel a)] and Grüneisen parameters for both ω_{V1} and ω_{V2} phonon peaks [panel b)] as function of the pressure.

Conclusions

In this last chapter, by comparing the results previously presented, we will try to further discuss them and to draw some general conclusions. The use of two different high pressure experimental techniques, Raman and Infrared spectroscopy, employed in all cases, with the help of high-pressure x-ray diffraction and ab initio calculation, exploited for Vanadium dioxide and Tellurium respectively has been sufficient to obtain a quite general picture of the pressure effects on lattice and electronic properties and to investigate the nature of the metal insulator transition of the three compounds under investigation, (Te, $NiS_{2-x}Se_x$, and VO_2) which are considered as paradigms of different types of metal insulator transition. The studies led to a number of results, following listed:

Solid Tellurium

A study of the pressure dependence of lattice dynamics and transport properties of solid Te has been carried out by monitoring Raman and Infrared response of the system up to 15 GPa and 10 GPa respectively. As matter of fact Raman spectroscopy demonstrated to be very effective in addressing the real sequence of structural phases followed by the system on increasing the pressure. The persistence of the Raman spectrum above 11 GPa is consistent with the presence of an incommensurate phase as proposed by Hejny and McMahon. Moreover two threshold pressures have been identified at 4 GPa and 8 GPa which have been interpreted as the occurrence of Te-II $\rightarrow$ Te-III phase transition and the complete removal of the Te-II phase respectively, according to the new high pressure scenario. A comparison between Raman results and the proposed structural phase transition sequence is shown in figure 6.26

As to the metallization process, Raman, Infrared and ab-initio calculation consistently provide a common scenario. The pressure dependence of the Raman-active modes, the removal of the band edge asymmetry approaching the transition and the modification of the electron density under lattice compression indicate that the charge delocalization is indeed obtained

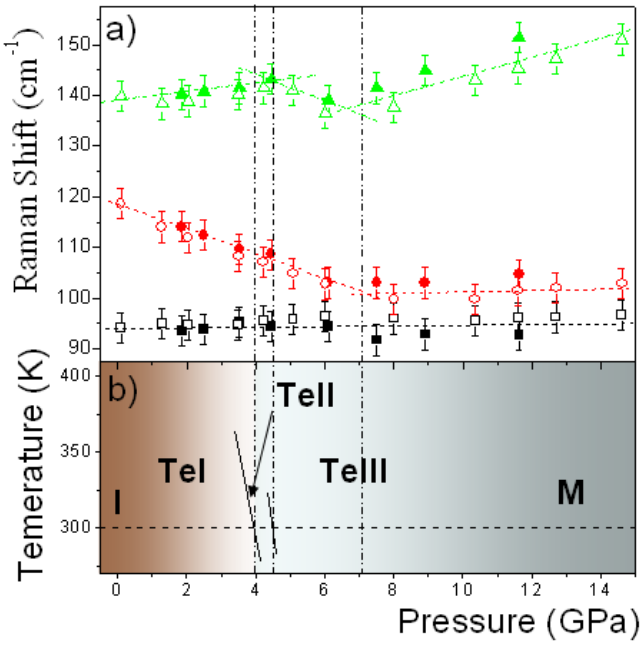

FIGURE 6.26: Comparison between phonon frequencies pressure dependence (panel a) and the new phase transition sequence (panel b) proposed by Hejny and McMahon [39].

from a structural symmetrization driven by inter-chain charge transfer which remove the Peierls distortion of the Te-chains.

Nichel pyrite

The Se alloying- and the Pressure- induced MITs in the charge-transfer $NiS_{2-x}Se_x$ compound has been investigated through Raman and Infrared spectroscopy. Whereas chemical substitution inevitably introduces impurities changing many of the physical parameters in an incontrollable way, Pressure offer a more systematic way of tuning the properties. The Raman and the Infrared response of NiS_2 to lattice compression is strongly correlated to the metallization process, occurring at $\sim$ 4GPa, pointing out a strong interaction between lattice and electronic degrees of freedom. In particular Infrared measurements carried out on applying pressure on pure NiS_2 (lattice contraction) and on Se alloying (lattice expansion) reveal that in both cases a metallic state is obtained. Thus optical spectroscopy results are not compatible with the idea of a simple scaling factor between Se-alloying and pressure previously claimed exploiting the results of transport measurements, but, on the contrary, point out the substantially different microscopic origin

of the two transitions, as also well evident from ab-initio calculations.

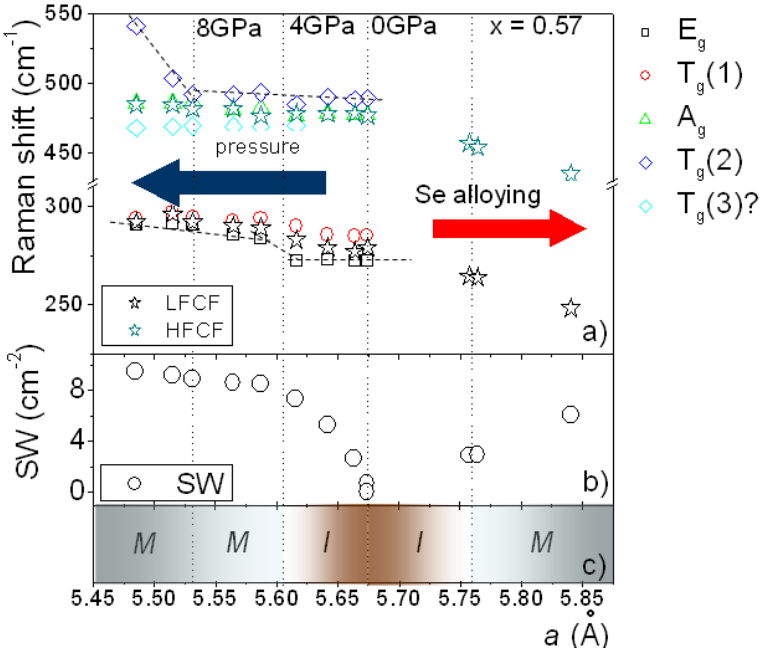

FIGURE 6.27: Phonon frequency (panel a) and Spectral Weight (SW) of NiS_2 as function of the lattice constant. Panel c) tentative phase diagram for NiS_2. Solid lines mark different electronic regimes, whereas dashed lines are guide for eyes.

Bearing in mind the volume (i.e. lattice constant) dependence of phonon frequencies and spectral weight ,SW, [see panel a) and b) of figure 6.27] a tentative phase diagram of NiS_2 [panel c of figure 6.27] can be drawn. Four different regimes within the same cubic structural phase can be identified in room temperature NiS_2 on varying the lattice constant. From 5.45 Åto 5.53 ÅNiS_2 is a *stable* metal and no more depend on volume as indicated by the saturation of the SW. . For a $>$ 5.57 Åand up to 5.60 Å(NiS2 at 4 GPa) where the MIT takes place(NiS2 at 4 GPa), the decrease of the SW indicate the onset of the insulating phase. On further increasing the lattice constant up to 5.68 ÅÅ, correlation effects get larger and the SW drops rapidly to the minimum value as a consequence of the Mott transition. In the same a range a phonon anomaly occurs in $T_g(2)$ modes. Finally increasing a above 5.68 Ådue to the Se alloying, the SW restarts to increase, owing to the onset of the Se-induced MIT, accompanied by a general phonon frequency softening of all the Raman active modes.

Vanadium dioxide

Room temperature Raman and Infrared measurements as a function of pressure on pure and Cr-doped VO_2 have been carried out. On increasing pressure the Raman spectrum of the two Cr-doped samples (in the M2 and M3 monoclinic phase at ambient conditions) gradually evolves toward that of VO_2 (in the M1 monoclinic phase) and at high pressure all the three samples show the same Raman spectrum, suggesting the onset of a common monoclinic phase Mx, which has a metallic behaviour as indicated by the strong enhancement of the spectral weight in the optical conductivity spectra. Bearing in mind the volume reduction at 10 GPa and under the assumption that entropy increases on entering the metallic phase, the scenario arising from the Clausius-Clapeyron equation is shown in the tentative phase diagram in Fig. 6.28. This hypothesis seems reasonable, taking into account that the M1 and the Mx structures should differ very slightly.

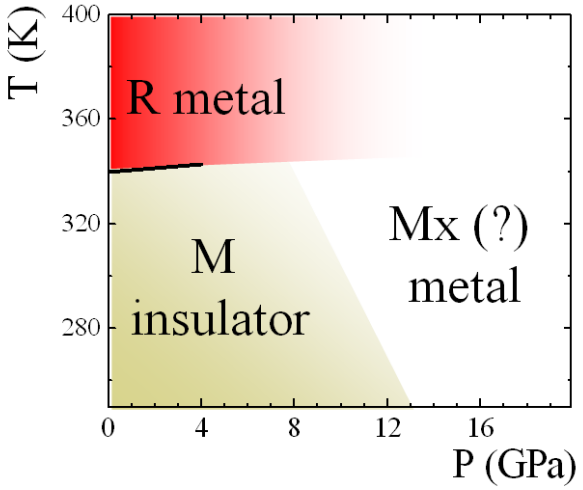

FIGURE 6.28: Tentative T vs. P phase diagram of VO_2. Full lines: high pressure data from Ref. [83]. Dashed line: tentative insulator to metal transition temperature. The slope referred to the hypothesis of an entropy increase on entering the metallic phase.

Since the monoclinic symmetry is, in principle, the signature of active Peierls distortions, the present results support a major role of the electron correlations against charge-lattice coupling in leading the MIT. However the role of the Peierls distortion in localizing free charges can not be completely ruled out. At this stage, it can not be estabilished if the transition to the Mx phase drives the insulator to metal transition or vise versa.

Conclusions

High pressure demonstrated to be a suitable tool for studying metallization processes in strongly correlated electron systems. The results obtained on the three investigated classes of material, charaterized by Peierls distortion and charge transfer gap and strong electron correlations are obviously different, depending on the details of each system, and common general conclusions are hard to be drawn. However in all the three cases pressure drive the systems toward a new regimes, characterized by different physical properties and possibly emphasizing of a specific interaction with respect the other simultaneously at work. On applying pressure the role of the different interactions in determining the physical properties of these complex systems have been disentangled and highlighted.

Appendix A

Optical properties of solids

Propagation of light in matter can be derived, in the limit where the wavelenght λ is larger than the atomic distances, by following the Maxwell equations behind the linear response approximation [147]. Indroducing the polarization of the medium and the Ohm's law, the wave equation for the electric field reads:

$$\nabla^2 \overrightarrow{E} = \frac{\epsilon}{c} \frac{\partial^2 \overrightarrow{E}}{\partial t^2} + \frac{4\pi\sigma}{c^2} \frac{\partial \overrightarrow{E}}{\partial t} \tag{A.1}$$

where σ is the frequency dependent conductivity of the medium which, in the limit $\omega \to 0$, gives the DC conductivity value. Writing the solution in the form:

$$\overrightarrow{E} = \overrightarrow{E_0} e^{i(\tilde{q} \cdot r - \omega t)} \tag{A.2}$$

the wave vector $\tilde{q}$ has to be a complex quantity, in order to include a propagation as well as as an attenuation part:

$$\tilde{q} = \frac{\omega^2}{c^2}(\epsilon + i\frac{4\pi\sigma(\omega)}{\omega}) \tag{A.3}$$

The optical properties of the medium can be described in terms of the frequency dependent complex dielectric function $\tilde{\epsilon}$:

$$\begin{aligned} Re(\tilde{\epsilon}) &= \epsilon_1 = \epsilon \\ Im(\tilde{\epsilon}) &= \epsilon_2 = \frac{4\pi\sigma}{\omega} \end{aligned} \tag{A.4}$$

The complex dielectric function describes the response of the medium to applied electromagnetic radiation. Due to the causality principle, real and imaginary part of the complex response function are related by the Kramers-Kroenig (KK) equations:

$$\epsilon_1(\omega) - 1 = \frac{2}{\pi} \int_0^\infty \frac{\omega' \epsilon_2(\omega') d\omega'}{\omega'^2 - \omega^2} \tag{A.5}$$

$$\epsilon_2(\omega) = -\frac{2}{\pi\omega}\int_0^\infty \frac{\omega'^2[\epsilon_1(\omega')-1]d\omega'}{\omega'^2-\omega^2} \tag{A.6}$$

The dispersion relation between $\tilde{q}$ and ω reads:

$$\tilde{q}^2 = \frac{\omega^2}{c^2}\tilde{\epsilon} \tag{A.7}$$

It is useful to define a complex refractive index $\tilde{n}$ as a new response function:

$$\tilde{n} = \tilde{\epsilon}^{1/2} = n + ik \tag{A.8}$$

so the dispersion relation A.7 becomes:

$$\tilde{q} = \frac{\omega}{c}\tilde{n} = \frac{n\omega}{c} + i\frac{k\omega}{c} \tag{A.9}$$

The real (n) and imaginary part (k) of the refractive index are related to the real and imaginary part of the dielectric function by the relations:

$$n^2 - k^2 = \epsilon_1 \tag{A.10}$$

$$2nk = \epsilon_2 = \frac{4\pi\sigma}{\omega} \tag{A.11}$$

The intensity I of the electromagnetic wave propagating in a medium is exponentially attenuated:

$$I(r) = I_0 e^{-\alpha r} \tag{A.12}$$

and the absorption coefficient α is directly related to the imaginary part of the refractive index:

$$\alpha = \frac{2k\omega}{c} \tag{A.13}$$

When the radiation arrives at the interface between two medium of different refractive index $\tilde{n_1}$ and $\tilde{n_2}$, part of the radiation is reflected. In condition of normal incidence the fraction of intensity reflected R is given by:

$$R = |\tilde{r}|^2 = \left|\frac{\tilde{n_1}-\tilde{n_2}}{\tilde{n_1}+\tilde{n_2}}\right|^2 \tag{A.14}$$

At the medium-vacuum interface the reflectivity R becomes:

$$R = |\tilde{r}|^2 = \left|\frac{1-\tilde{n}}{1+\tilde{n}}\right|^2 = \frac{(1-n)^2+k^2}{(1+n)^2+k^2} \tag{A.15}$$

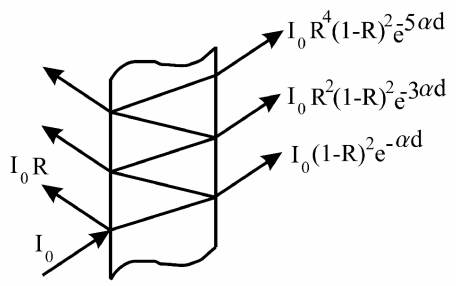

FIGURE A.1: Multiple reflections within a sample layer of thickness d.

By a reflectivity measurement on an infinitely thick sample it is possible to extract both the real and the imaginary part of its refractive index exploiting the KK relations:

$$\tilde{r} = \frac{\tilde{n_1} - \tilde{n_2}}{\tilde{n_1} + \tilde{n_2}} = \sqrt{R(\omega)}e^{i\Theta(\omega)} \Rightarrow \ln(\tilde{r}) = \ln(\sqrt{R(\omega)}) + i\Theta(\omega) \tag{A.16}$$

$$\Theta(\omega) = -\frac{\omega}{\pi}\int_0^\infty \frac{\ln(R(\omega'))}{\omega'^2 - \omega^2}d\omega' \tag{A.17}$$

By calculating $\Theta(\omega)$ from Eq.A.17, Eq.A.16 allows to obtain n and k, from which the optical conductivity $\sigma(\omega)$ is eventually achieved from Eq.A.11. However this procedure requires reflectivity data over a frequency range as much as possible wide, and reasonable extrapolation at low and high frequency are necessary.

Let's now consider a sample layer of thickness d. In order to obtain the transmitted intensity I_t, the multiple reflections within the sample must to be taken into account (see Fig. A.1). Multiple refections give rise to interference fringes spaced by $\Delta\omega = 1/2nd$ in the reflected and transmitted spectra. Moreover the transmittance is reduced. In the incoherent approximation I_t is given by:

$$I_t = I_0(1-R)^2e^{-\alpha d} + I_0R^2(1-R)^2e^{-3\alpha d} + \cdots \tag{A.18}$$

$$= I_0(1-R)^2e^{-\alpha d}\sum_{n=0}^{\infty}(R^2e^{-2\alpha d})^n \tag{A.19}$$

$$= I_0\frac{(1-R^2)e^{-\alpha d}}{1-R^2e^{-2\alpha d}} \tag{A.20}$$

where I_0 is the incident radiation. The *optical density* can be defined:

$$O_d = -\ln\left(\frac{I_t}{I_0}\right) = \ln\frac{1-R^2e^{-2\alpha d}}{(1-R^2)e^{-\alpha d}} \tag{A.21}$$

Optical density qualitatively reflect optical conductivity behavior. However both reflectance and transmittance measurements are required for a quantitative analysis.

Appendix B

Effective reflectance and transmittance of a sample in a diamond anvil cell

The analysis of infrared measurements of sample loaded in a diamond anvil cell (DAC) is made complicated by the presence of diamond-sample and sample-hydrostatic medium interfaces. Transmittance measurements on thin samples are typically affected by multiple reflections which increase reflectivity, reduce transmittance and generate interference fringes. On the other hand the presence of a sample-diamond interface prevents the employment of a standard analysis and the KK relation between reflectivity and phase need to be corrected, including *a priori* unknown parameters [168].

In this work optical conductivity σ has been achieved in an alternative way, exploiting the simultaneous measurements of reflectance R and transmittance T of the sample. In this chapter the modeling of R and T and the extraction of σ is discussed in detail. In section B.1 and B.2 the analytical derivation of the effective reflectance and transmittance of a sample loaded in the diamond anvil cell (DAC) obtained behind the incoherent approximation is reported. The derivation referred to a loading geometry in which a sample slab (V) of thickness d is placed on top of a salt pellet (S) between the two diamonds (D), thus forming a four-layer as is sketched in Fig.B.1. In section B.3 numerical technique for extracting σ from the experimental data is discussed.

Behind the incoherent approximation, reflectivity and transmission of the quadrilayer can be obtained by evaluating the sum of the intensities of the infinity of multiple reflected beams within the quadrilayer.

At the first diamond-sample interface the fraction R_{VD} of the intensity of the incident radiation of frequency ω is reflected and gives the first term to the

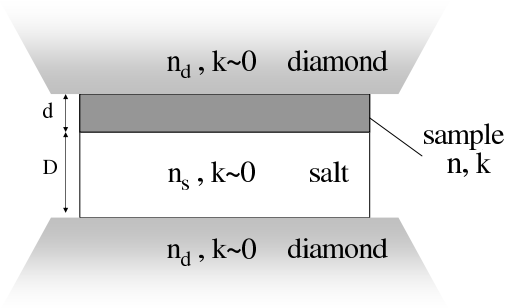

FIGURE B.1: Four layer scheme applied for modeling the optical properties of the diamond anvil cell loaded with the a sample slab of thickness d.

effective reflectivity. The fraction $(1 - R_{VD})$ is transmitted and attenuated.

At the sample-salt interface the fraction R_{VS} is reflected back to the sample and the fraction $(1 - R_{VS})$ is transmitted towards the salt. Both the beams generate multiple reflections within the salt and the sample layers. The sum may be analytically evaluated, you just need to remember that at each crossing of the sample each beam is attenuated and that at each interface each beam splits into two parts which, in turn, lead to other multiple reflections... Albeit the analytical calculation is rather lengthy, the sum may be evaluated by means of a resumation scheme described below, in order to obtain the effective reflectivity and transmittance.

B.1 Effective reflectivity

The effective reflectance calculus requires to take into account the different terms arising from the multiple reflections generating within the sample and within the salt. The first term is given by the fraction of intensity directly reflected by the diamond-sample interface R_{VD}. The fraction $1 - R_{VD}$ is transmitted by the sample, attenuated by the factor $e^{-\alpha d}$, and splits into two parts, one reflected by the sample-salt interface (R_{VS}) and one transmitted $(1 - R_{VS})$. The latter generates multiple interference within the salt, which gives the contribution S_S to the effective reflectivity of the sample salt interface:

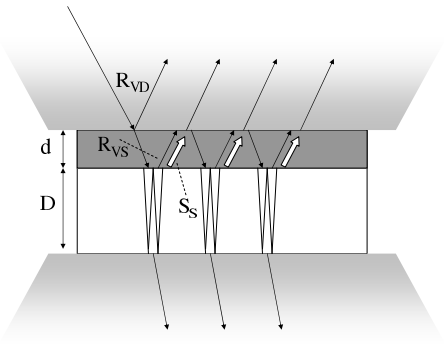

FIGURE B.2: Contribution to effective reflectance of the four-layer.

$$S_S = (1-R_{VS})R_{SD}(1-R_{VS}) + (1-R_{VS})R_{SD}R_{VS}R_{SD}(1-R_{VS}) \\ +(1-R_{VS})R_{SD}R_{VS}^2R_{SD}^2(1-R_{VS}) + \cdots = \quad \text{(B.1)}$$

$$(1-R_{VS})R_{SD}(1-R_{VS})\sum_{n=0}^{\infty}(R_{VS}R_{SD})^n = \frac{R_{SD}(1-R_{VS})^2}{1-R_{VS}R_{SD}} = S_S \quad \text{(B.2)}$$

The intensity reflected by sample-salt interface:

$$(1-R_{VD})e^{-\alpha d}(R_{VS}+S_S) \quad \text{(B.3)}$$

is transmitted back trough the sample and attenuated. At the sample-diamond interface the fraction $1-R_{VD}$ is transmitted and yields the second contribution to the effective reflectance:

$$(1-R_{VD})e^{-\alpha d}(R_{VS}+S_S)e^{-\alpha d}(1-R_{VD}) \quad \text{(B.4)}$$

The fraction R_{VD} of B.3 is reflected back trough the sample, reaches the sample-salt interface, generates multiple reflection and a fraction of this intensity comes back to the sample-diamond interface, at which it splits once again and gives this contribution to the effective reflectance:

$$(1-R_{VD})\underbrace{e^{-\alpha d}(R_{VS}+S_S)e^{-\alpha d}R_{VD}}\underbrace{e^{-\alpha d}(R_{VS}+S_S)e^{-\alpha d}}(1-R_{VD}) \quad \text{(B.5)}$$

The effective reflectance given by the sum of these infinite terms reads:

$$= R_{VD} + (1 - R_{VD})^2 (R_{VS} + S_S) e^{2\alpha d} \sum_{n=0}^{\infty} ((R_{VS} + S_S) R_{VD} e^{-2\alpha d})^n \quad \text{(B.6)}$$

By evaluating the sum and by means of suitable simplifications the effective reflectance is achieved:

$$R_{eff} = R_{VD} + \frac{(1 - R_{VD})^2 e^{-2\alpha d} (R_{VS}(1 - R_{SD}) + R_{SD})}{1 - R_{VS} R_{SD} - (R_{VS}(1 - 2R_{SD}) + R_{SD}) R_{VD} e^{-2\alpha d}} \quad \text{(B.7)}$$

B.2 Effective transmittance

As for the effective reflectance evaluation, the effective transmittance calculus requires to combine the multiple reflections generating within the sample with that generating within the salt. The intensity fraction $(1 - R_{VD})$ which enters into the sample is attenuated and divided into two parts at the sample-salt interface. The fraction T' which is transmitted across the sample-salt interface is given by the not-reflected part $(1 - R_{VS})$ plus the transmitted part of the multiple reflections within the sample:

$$T' = (1 - R_{VD}) e^{-\alpha d} [(1 - R_{VS}) + R_{VS} e^{-\alpha d} R_{VD} e^{-\alpha d} (1 - R_{VS}) + R_{VS} e^{-\alpha d} R_{VD} e^{-\alpha d} R_{VS} e^{-\alpha d} R_{VD} e^{-\alpha d} (1 - R_{VS}) + \cdots] \quad \text{(B.8)}$$

$$T' = (1 - R_{VD}) e^{-\alpha d} (1 - R_{VS}) \sum_{n=0}^{\infty} (R_{VS} e^{-2\alpha d} R_{VD})^n \quad \text{(B.9)}$$

$$T' = \frac{(1 - R_{VD}) e^{-\alpha d} (1 - R_{VS})}{1 - (1 - R_{VD}) e^{-\alpha d} (1 - R_{VS})} \quad \text{(B.10)}$$

The fraction T' of intensity is transmitted by the salt and arrives at the salt-diamond interface: the fraction $(1 - R_{SD})$ is transmitted while the fraction R_{SD} is reflected and leads to multiple reflections within the salt. At each salt-diamond interface a new term has to be added to the R_{VS} fraction. R' is the sum of these contribution:

$$R' = R_{VS} + (1 - R_{VS}) e^{-\alpha d} R_{VD} e^{-\alpha d} (1 - R_{VS}) + \quad \text{(B.11)}$$

$$(1 - R_{VS}) e^{-\alpha d} R_{VD} e^{-\alpha d} R_{VS} e^{-\alpha d} R_{VD} (1 - R_{VS}) + \cdots \quad \text{(B.12)}$$

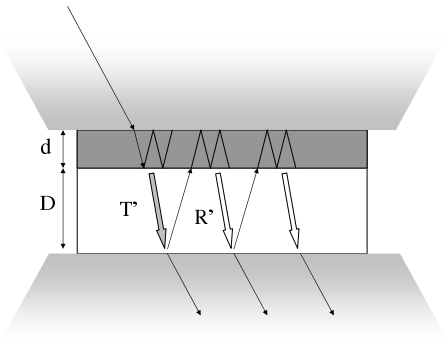

FIGURE B.3: Contribution to effective transmittance of the four-layer.

$$R' = R_{VS} + (1 - R_{VS})^2 e^{-2\alpha d} R_{VD} \sum_{n=0}^{\infty} (R_{VS} R_{VD} e^{-2\alpha d})^n = \tag{B.13}$$

$$R_{VS} + \frac{(1 - R_{VS})^2 e^{-2\alpha d} R_{VD}}{1 - R_{VS} R_{VD} e^{-2\alpha d}} \tag{B.14}$$

The first term in leading the effective transmission is given by the fraction of intensity transmitted by the sample (T') and not reflected by the salt-diamond interface:

$$T'(1 - R_{SD}) \tag{B.15}$$

The second term arises from the fraction of T' reflected by the sat-diamond interface (R_{SD}), reflected back by the sample (the effective reflectance is R') and eventually transmitted by the salt-diamond interface:

$$T' R_{SD} R' (1 - R_{SD}) \tag{B.16}$$

In the same manner the third term can be easily obtained:

$$T' R_{SD} R' R_{SD} R' (1 - R_{SD}) \tag{B.17}$$

By evaluating the serie the effective transmittance is achieved:

$$T_{eff} = \frac{T'(1 - R_{SD})}{1 - R_{SD} R'} \tag{B.18}$$

and remembering the definitions of T' and R' (Eq.B.10 and Eq.B.13):

$$T_{eff} = \frac{(1 - R_{VD})(1 - R_{VS})(1 - R_{SD})e^{-\alpha d}}{1 - R_{VS}R_{VD}e^{-2\alpha d} - R_{SD}(R_{VD}e^{-2\alpha d} - 2R_{VS}R_{VD}e^{-2\alpha d} + R_{VS})} \tag{B.19}$$

B.3 Optical conductivity from experimental data

Equations B.7 and B.19 can be used to analyze experimental reflectance R_{exp} and transmittance T_{exp} data. Knowing the optical properties of diamond and salt in the frequency range investigated and the slab thickness d, R_{eff} and T_{eff} are a function of the real and imaginary part of the complex refraction index of the sample, on which depend R_{VD}, R_{VS} and α. At each frequency a system of two equations has to be solved to obtain $n(\omega)$ and $k(\omega)$. Since the system is non-analytical a numerical iteration technique has been developed.

A guess function $n_0(\omega)$ can be put equal to the average refraction index of the sample, if known, or alternatively achieved by analytically solving the simplified systems of equations obtained by neglecting multiple reflections:

$$R_{spe} = R_{VD} \tag{B.20}$$

$$T_{spe} = (1 - RVD)e^{-\alpha d} \tag{B.21}$$

$k_0(\omega)$ is obtained inserting $n_0(\omega)$ into the $T(\omega)$ equation B.19. The successive iterate, $n_1(\omega)$, is obtained inserting $k_0(\omega)$ into $R(\omega)$ and in turn $n_1(\omega)$ into $T(\omega)$ to get $k_1(\omega)$. The procedure could be iterated and typically converges after few steps. The optical conductivity is eventually achieved by the relation A.11.

Appendix C

Measuring the reference in a Reflectivity measurement: the evaporation technique

To obtain the absolute value of the reflectivity R(ω) is necessary to measure a reference signal. Usually both the intensity reflected by the sample and that from a pre-aligned reference (a mirror) are measured. However, when measuring small samples, diffraction becomes important because may arise both from the sample irregular shape and imperfections, if the typical surface defect dimension r is comparable with $lambda_0$ (the average used wavelength). For commercial mirrors, the roughness is typically smaller than $lambda_0$. Therefore between the intensity reflected by the sample and that by the reference different diffraction effects could occur. Such diffraction effects can instead be accounted, and partially eliminated, with the evaporation overfilling technique: the sample surface itself is covered by a gold, or silver, or aluminum film to serve as a reference. The thickness of such film is smaller than surface defects dimension through in-vacuum metal evaporation. By using this technique, diffraction effects should become negligible, as showed by Homes et al. [169].

In Fig. C.1 we show the evaporation device. A short wire of the metal to be evaporated is threaded in a tungsten filament. The filament is connected to a wand that can be raised or lowered from outside the cryostat (or the heating system), so that it can be placed in front of the sample. When a current of about 3 A passes through the filament, the metal melts and a film is deposited on the sample surface. It is common experience that the best deposition occur when the sample is at room temperature. It is worth of noticing that no optical path is changed during the deposition and that the interferometer is kept evacuated and free of any mechanical stress.

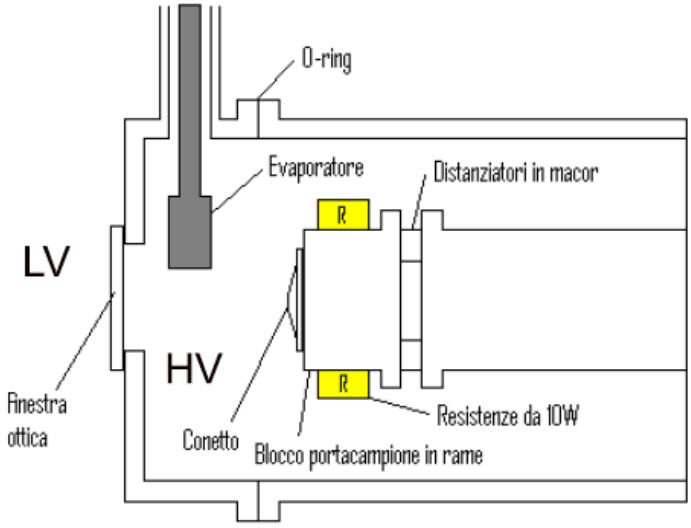

FIGURE C.1: Schematic representation of the heating system. As for the closedcycle cryogenerator two vacuum environments exist: (LV) low vacuum for the interferometer optics and (HV) high vacuum for the cryostat. An IR window separates the two environments.

Bibliography

[1] F. N. Mott, *"Metal Insulator transitions"*, Taylor and Francis, London, 1990.

[2] R. E. Peierls, *Quantum Theory of Solids*, Oxford University, New York/London (1955).

[3] J. C. Slater, *Phys. Rev.* **82**, 538 (1951).

[4] M. Imada, A. Fujimori and Y. Tokura, *Rev. Mod. Phys.* **70**, 1039 (1998).

[5] J. Zaanen, G. A. Sawatzky, and J. W. Allen,*Phys. Rev. Lett.* **55**, 418 (1985).

[6] J. Hubbard, *Proc. R. Soc. London, Ser. A* **276**, 238 (1963).

[7] S. Hufner, F. Hulliger, J. Osterwalder, and T. Riesterer, *Solid State Commun.*, **50**,83 (1984).

[8] P. W. Andersen, *Phys. Rev.* **124**, 41 (1961).

[9] D. Adler, *Rev. Mod. Phys.* **40**, 714 (1968).

[10] D. Adler and H. Brooks, *Phys. Rev* **155**, 826 (1967).

[11] N.P. Ong, *Physical Properties of High Temperature Superconductors*, D.M. Ginsberg Ed. (1990).

[12] H. Watanabe and S. Doniach, *Phys. Rev. B*, **57**, 3829 (1998).

[13] W.F. Brinkman and T.M. Rice, *Phys. Rev.* **2**, 4302 (1970).

[14] M.C. Gutzwiller, *Phys. Rev.* **137**, A1726 (1965).

[15] M. Lavagna, *Phys. Rev. B* **41**, 142 (1990).

[16] A. Georges, G. Kotliar, W. Krauth and M.J. Rozenberg, *Rev. Mod. Phys.* **68**,13 (1996).

[17] G. Kotliar and D. Volhardt, *Physics Today* **53** (2004)

[18] A. P. Sutton, *Electronic Structure of Materials*, Oxford Science Pubblication, London (1997).

[19] H. Fröhlich, *Adv. Phys.* **3**, 325 (1954).

[20] H. Fröhlich, *Proc. R. Soc. A* **223**, 296 (1954).

[21] G. Grüener, *Density waves in solids*, Addison Wesley, Reading, MA (1994).

[22] M. Hoesch, A. Bosak, D. Chernyshov, H. Berger, and M. Krisch, *Phys. Rev. Lett.* **102**, 086402 (2009).

[23] N. Ru and I. R. Fisher, *Phys. Rev. B* **73**, 033101 (2006).

[24] N. Ru, C. L. Condron, G. Y. Margulis, K. Y. Shin, J. Laverock, S. B. Dugdale, M. F. Toney, and I. R. Fisher, *Phys. Rev. B* **77**, 035114 (2008).

[25] J. Luttinger, *J. Math. Phys.* **4**, 1154 (1963).

[26] S. Tomonaga, *Prog. Theor. Phys.* **5**, 554 (1950).

[27] F. A. Blum and B. C. Deaton Phys Rev 137 A1410 (1965)

[28] Y. Sekine, H. Takahashi, N. Mori, T. Matsumot,T. Kosaka, *Physica B*, **237**, 148 (1997).

[29] F. J. Morin, *Phys. Rev. Lett* **3**, 34 (1959).

[30] Hejny, C. and McMahon, M. I.,*Phys. Rev. Lett.*, **91**, 215502 (2003).

[31] K. Takemura, K. Sato, H. Fujihisa,and M. Onoda,*Nature* **423**, 971 (2003).

[32] O. Degtyareva, E. Gregorianz, M. Somayazulu, P. Dera, H. K. Mao and R. J. Helmey, emphNature, **4**, 152 (2005).

[33] P.W. Bridgman, *Proc. Am. Acad. Arts Sci.*, **81**, 167 (1952).

[34] J. Donohue, *The Structures of the Elements*, New York: John Wiley and Sons (1974).

[35] G. Kresse, J. Furthmüller, and J. Hafner, *Phys. Rev. B* **50**, 13181 (1994).

[36] K. Aoki, O. Shimomura, S. Minomura, J. Phys. Sot. Jpn **48**, 551 (1980).

[37] C. Jamieson, D.B. McWhan, *J. Chem. Phys.* **43**, 1149 (1965).

[38] G. Parthasarathy, W.B. Holzapfel, *Phys. Rev. B* **37**, 8499 (1988).

[39] C. Hejny and M. I. McMahon, *Phys. Rev. B*, **70**, 184109 (2004).

[40] I. Loa, M. I. McMahon, and A. Bosak, *Phys. Rev. Lett.*, **102**, 035501 (2009).

[41] H. C. Hsueh, C. C. Lee, C. W. Wang, J. Crain, *Phys. Rev. B*, **61**, 3851 (1999).

[42] M. G. Garnier, R. Wahrenberg, and P. Oelhafen, *Phys. Rev. B*, **65**, 113204 (2002).

[43] T. Starkloff and J. D. loannopoulos, *Phys. Rev. B*, **19** 1077 (1979).

[44] lsomaki H, von Bwhm I, Krusius P and Stubb, *Phys. Rev. B* **22**, 2945 (1980).

[45] H M and von Bcehm J 1987 *Phys. Rev. B*, **35**, 8019 (1987).

[46] A. Nishikawa, *phys. stat. sol. (b)*, **244**, 321 (2007).

[47] Ibach H and Ruin R *Phys. Stat. Solidi* **41**, 719 (1970).

[48] G K White, *J. Phys. C Solid State Phys.* **6**, 1548 (1973).

[49] A J Leadbetter and A P Jeapes, *J. Phys. C: Solid State Phys.*, **6** (1973).

[50] K. Iwaya, Y. Kohsaka, S. Satow, T. Hanaguri, S. Miyasaka, and H. Takagi, *Phys. Rev. B* **70**, 161103(R) (2004).

[51] A. Fujimori, K. Mamiya, T. Mizokawa, T. Miyadai, T. Sekiguchi, H. Takahashi, N. Mori, and S. Suga, *Phys. Rev. B* **54**, 16329(1996).

[52] A. Ohsawa, H. Yamamoto, H. Watanabe, *J. Phys. Soc. Jpn.*, **37**, 568 (1974).

[53] D. D. Klemm, N. Jahr. *Miner. Monat.* **32** (1962).

[54] C. de las Heras and F. Agull Rueda, *J. Phys. Condens. Matter*

[55] X. Yao, J. M. Honig, T. Hogan, C. Kannewurf and J. Spalek, *Phys. Rev. B* **54**, 17469 (1996).

[56] S. A. Carter, J. Yang, T. F. Rosenbaum, J. Spalek, and J. M. Honig, *Phys. Rev. B* **43**, 607 (1991). **12**,5317 (2000).

[57] A. K. Mabatah, E. J. Yoffa, P. C. Ekulund, M. S. Dresselhaus and D. Adler, *Phys. Rev. B* **21**, 1676 (1980).

[58] J. B. Goodenough, *J. Solid State Chem.* **3**, 490 (1971).

[59] J. B. Goodenough, *J. Solid State Chem.*, **5**, 144 (1972).

[60] S. Ogawa, *J. Appl. Phys* **50**, 2308 (1979).

[61] G. Krill, M. F. Lapierre, F. Gautier, C. Robert, G. Czjzek, J. Fink, and H. S. Schmidt, *J. Phys. C. Solid State Phys.* **9**, 761 (1976).

[62] A. Y. Matsuura, Z.-X. Shen, D. S. Dessau, C.-H. Park, T. Thio, J. W. Bennett, O. Jepsen, *Phys. Rev. B* **53**, R7584 (1996).

[63] K. Mamiya, T. Mizokawa, A. Fujimori,T. Miyadai, N. Chandrasekharan, S. R. Krishnakumar, and D. D. Sarma, H. Takahashi, N. Mori and S. Suga, *Phys. Rev. B* **58**, 9611 (1998).

[64] S. Ogawa, *J. Phys. Soc. Jpn.* **41**, 462 (1976).

[65] N. Inoue, H. Yasuoka, S. Ogawa, *J. Phys. Soc. Jpn.* **48**, 850 (1980).

[66] S. Ogawa, *J. Appl. Phys.* **50**, 2308 (1979).

[67] X. Yao, Y. K. Kuo, D. K. Powell, J. W.Brill, J. M. Honig, *Phys. Rev. B* **56**, 7129 (1997).

[68] N. W. Ashcroft and N. D. Mermin, *"Solid State Physics"*, Cornell University (1976).

[69] S. Sudo, T. Nishioka, Y. Miyako, T. J. Miyadai, *Phys. Soc. Jpn.* **55**, 1806 (1986).

[70] T. Miyadai, Y. Tazuke, S. Kinouchi, T. Nishioka, S. Sudo, Y. Miyako, K. Watanabe, K. Inoue, *J. Phys. Coll.* **49**, C8-187 (1988).

[71] J. A. Wilson, G. D. Pitt, *Philos. Mag.* **23**, 1297 (1971).

[72] M. Kamada, N. Mori, T. Mitsui, *J. Phys. Soc. C: Solid State Phys.* **10**, L643 (1977).

[73] N. Mori, M. Kamada, H. Takahashi, G. Comi, S. Susaki, *Solid State Physics Pressure: Recent Adv. Anvil Devices*, 247 (1984).

[74] S. Miyasaka, H. Takagi, Y. Sekine, H. Takahashi, N. Mori and R. J. Cava, *J. Phys. Soc. Japan*, **69**, 3166 (2000).

[75] T. Fujii, K. Tanaka, F. Marumo, Y. Noda, *Miner. J.*, **13**, 448 (1987).

[76] S. Endo, T. Mitsui, T. Miyadai, *Phys. Lett.*, **46A**, 29 (1973).

[77] N. Mori, T. Mitsui, S. Yomo,*Solid State Commun.*, **13**, 1083 (1973).

[78] N. Mori, H. Takahashi, *J. Magn. Magn. Mater.*, **31-34**, 335 (1983).

[79] A. Magnèli, *Acta Chem. Scand.* **2**, 501 (1948).

[80] A Perucchi, L Baldassarre, P Postorino, and S Lupi, *J. Phys. Condens. Matter* **21** 323202 (2009).

[81] S. Shin, S. Suga, M. Taniguchi, M. Fujisawa, H. Kanzaki, A. Fujimori, H. Daimon, Y. Ueda, K. Kosuge, and S. Kachi, *Phys. Rev. B* **41**, 4993 (1990).

[82] L. A. Ladd, W. Paul, *Sol. State. Comm.* **7**, 425 (1968).

[83] C. N. Berglund, A. Jayaraman, *Phys. Rev.* **185**, 1034 (1969).

[84] C. N. Derglund, H. J. Guggenheim, *Phys. Rev.* **185**, 1022 (1069).

[85] D. B. McWhan, M. Marezio, J. P. Remeika, P. D. Dernier, *Phys. Rev. B* **10**, 490 (1974).

[86] J. M. Longo, P. Kierkegaard, *Acta Chem. Scand.* **24**, 420 (1970).

[87] H. W. Verleur, A. S. Barker, C. N. Berglund, *Phys. Rev.* **172**, 788 (1968).

[88] H. S. Choi et al., *Phys. Rev. B* **54**, 4621 (1996).

[89] P. B. Allen, R. M. Wentzcovitch, W. W. Schulz, P. C. Canfield, *Phys. Rev. B* **48**,4359 (1993).

[90] J. Umeda, H. Kusumoto, K. Narita, E. Yamada, *J. Chem. Phys.* **42**, 1458 (1965).

[91] H.-T. Kim; B.-G. Chae; D.-Y. Youn; S.-L. Maeng; G. Kim; K.-Y. Kang, Y.-S. Lim., *New J. Phys.* **6**, 52 (2004).

[92] M. A. Richardson and J. A. Coath. *Opt. Las. Tech.*, **30**, 137 (1998).

[93] L. Jiang and W. N. Carr. *J. Micromech. Microeng.* **14**, 833 (2004).

[94] J. M. Reyes, M. Sayer, A.Mansingh, R. Chen, *Can. J. Phys.* **54**, 413 (1976).

[95] J.P. Pouget, H. Launois, J. P. D'Haenens, P. Merenda, T. M. Rice, *Phys. Rev. Lett* **35**, 873, (1975).

[96] T. M. Rice, H. Launois, J.P. Pouget, *Phys. Rev. Lett.* **73**, 3042 (1994).

[97] J. M. Reyes, M. Sayer, R. Chen, *Can. J. Phys.* **54**, 408 (1976); T. Horlin, T. Niklewski, M. Nygren, *Mat. Res. Bull.* **7**, 1515 (1972).

[98] M. Marezio, D. B. McWhan, J. P. Remeika, P. D. Dernier, *Phys. Rev. B* **5**, 2541 (1972).

[99] G. Villeneuve, M. Drillon, P. Hagenmuller, *Mat. Res. Bull.* **8**, 1111 (1973).

[100] J. P. D'Haenens, D. Kaplan, P. Merenda, *J. Phys. C* **8**, 2267 (1975).

[101] R. M. Wentzcovitch, W. W. Schulz, P. B. Allen, *Phys. Rev. Lett.* **72**, 3389 (1994).

[102] V. Eyert, *Ann. Phys. (Leipzig)* **11**, 650 (2002).

[103] M. Abbate, F. M. F. de Groot, J. C. Fuggle, Y. J. Ma, C. T. Chen, F. Sette, A. Fujimori, I. Ueda, K. Kosuge, *Phys. Rev. B* **43**, 7263 (1991).

[104] M.W. Haverkort, Z. Hu, A. Tanaka, W. Reichelt, S.V. Streltsov, M. A. Korotin, V. I. Anisimov, H. H. Hsieh, H.-J. Lin, C. T. Chen, D. I. Khomskii, and L. H. Tjeng, *Phys. Rev. Lett* **95**, 196404 (2005).

[105] T. C. Koethe, Z. Hu, M.W. Haverkort, C. Schüβler-Langeheine, F. Venturini, N. B. Brookes, O. Tjernberg, W. Reichelt, H. H. Hsieh, H.-J. Lin, C. T. Chen, and L. H. Tjeng, *Phys. Rev. Lett.* **97**, 116402 (2006).

[106] R. Eguchi, M. Taguchi, M. Matsunami, K. Horiba, K. Yamamoto, Y. Ishida, A. Chainani, Y. Takata, M.Yabashi, D. Miwa, Y. Nishino, K. Tamasaku, T. Ishikawa, Y. Senba, H. Ohashi, Y. Muraoka, Z. Hiroi, and S. Shin, *Phys. Rev. B* **78**, 075115 (2008)

[107] R. M. Wentzcovitch, W. W. Schulz, P. B. Allen, *Phys. Rev. Lett.* **73**, 3043 (1994).

[108] A. Bianconi, S. Stizza, R. Bernardini, *Phys. Rev. B* **24**, 4406 (1981).

[109] M. M. Qazilbash, K. S. Burch, D. Whisler, D. Shrekenhamer, B. G. Chae, H. T. Kim, D. N. Basov, *Phys. Rev. B.* **74**, 205118 (2006).

[110] J. Galy and G. Miehe, *Solid State Sci.* **1**, 433 (1999).

[111] J. B. Goodenough, *Phys. Rev. B* **8**, 1323 (1973).

[112] J. P. Pouget, H. Launois, T. M. Rice, P. Dernier, A. Gossard, G. Villeneuve, and P. Hagenmuller, *Phys. Rev. B* **10**, 1801 (1974).

[113] A. Zylbersztejn, N. F. Mott, *Phys. Rev. B* **11**, 4383 (1975).

[114] D. Paquet, P. Leroux-Hugon, *Phys. Rev. B* **22**, 5284 (1980).

[115] M. S. Laad, L. Craco, and E. Muller-Hartmann, *Europhys. Lett.* **69**, 984 (2005).

[116] S. Biermann, A. Poteryaev, A. I. Lichtenstein, A. Georges, *Phys. Rev. Lett.* **94**, 026404 (2005).

[117] A. Jayaraman, *Rev. Sci. Instrum.* **57**, 1013 (1986)

[118] A. Jayaraman, *Rev. Mod. Phys.* **55**, 65 (1983)

[119] P. Dore, A. Nucara, D. Cannav, G. De Marzi, P. Calvani, A. Marcelli, R.S. Sussmann, A.J. Whitehead, C.N. Dodge, A.J. Krehan, and H.J. Peters, *Appl. Optics* **37**, 5731 (1998).

[120] D. J. Dunstan, *Rev. Sci. Instrum.* **60**, 3789 (1989)

[121] I. Goncharenko, *High Pressure Research* **24**, 193 (2004)

[122] G.J. Piermarini and S. Block, *Rev. Sci. Instrum.* **46**, 973 (1975).

[123] H.K. Mao, J. Xu, and P.M. Bell, *J. Geophys. Res.* **91**, 4673 (1986).

[124] S. Lupi, A. Nucara, A. Perucchi, P. Calvani, M. Ortolani, L. Quaroni, M. Kiskinova, *JOSA B* **24**, 959 (2007).

[125] R.L. Kautz *et al.*, Phys. Rev. B **6**, 2078 (1972).

[126] G. Lucovsky, *"Physics of Selenium and Tellurium"*, ed W. C. Cooper, Pergam, Oxford, (1969).

[127] A. S. Pine and G. Dresselhaus, *Phys. Rev. B* **4**, 356 (1971).

[128] S. Tutihasi, G. G. Roberts, R. C. Keezer, and R. E. Drews *Phys. Rev.* **177**, 1143 (1969).

[129] I. Ymamoto, Y. Ohmasa, H. Ikeda and H. Endo *J. Phys. Condens. Mat.* **7**, 4299 (1995).

[130] T. Janssen, *J. Phys. C Solid Stat. Phys.* **12**, 5381 (1979).

[131] Th. Rasing, P. Wyder, A. Janner, and T. Janssen, *Phys. Rev. B* **25**, 7504 (1982).

[132] A. Congeduti, P. Postorino, E. Caramagno, M. Nardone, A. Kumar, D. D. Sarma, *Phys. Rev. Lett.* **86**, 1251 (2001).

[133] S. Baroni, A. Dal Corso, S. de Gironcoli, P. Giannozzi, C. Cavazzoni, G. Ballabio, S. Scandolo, G. Chiarotti, P. Focher, A. Pasquarello, K. Laasonen, A. Trave, R. Car, N. Marzari, A. Kokalj, *http://www.pwscf.org/*.

[134] M. Blanchard, M. Alfredsson, J. Brodholt, G. D. Price, K. Wright, and C. R. A. Catlow, *J. Phys. Chem. Solids* **109**, 22067 (2005).

[135] V. Lemos, G. M. Gualberto, J. B. Salzberg and F. Cerdeira, *Phys. Stat. Sol. b* **100**, 755 (1980).

[136] T. Suzuki, K. Uchinokura, T. Sekine and E. Matsuura *Solid State Commun.* **23**, 847 (1977).

[137] T. Stingl, B. Müller, H. D. Lutz, *J. Alloys Compounds* **184**, 275 (1992).

[138] H. Takahashi, *J. Magn. and Magn. Mat.* **54-57**, 1019 (1986).

[139] P. Postorino, A. Congeduti, E. Degiorgi, J.P. Iti, and P. Munsch, *Phys. Rev. B* **65**, 224102 (2002).

[140] T. A. Bither, R. J. Bouchard, W. H. Cloud, P. C. Dokohue, and W. J. Siemoks, *Inorg. Chem.* **7**, 2208 (1968).

[141] H. Takahashi, N. Mori, S. Yomo, Z.S. Jin, K. Tsuji and S. Minomura, *Proc. Intern. Syrup. on Solid State Phys. under Pressure*, Izu-Nagaoka, Japan (1984).

[142] D. D. Sarma, M. Pedio, M. Capozi, and A. Girycki, C. Ottaviani, C. Quaresima, and P. Perfetti, *Phys. Rev. B* **57**, 6984 (1998).

[143] H. Z. Zhuang, X. W. Zou, Z. Z. Jin, and D. C. Tian, *Phys. Rev. B.*, **55** R 6105 (1997)

[144] A. Debernardi and M. Cardona, *Nuovo Cimento Soc. Ital. Fis.*, **20D**, 923 (1998).

[145] S. Tamura *Phys. Rev. B* **27**, 858 (1983).

[146] F. Wooten, in *Optical Properties of Solids*, Academic Press, New York (1972).

[147] M. Dressel and G. Grüner, *Electrodynamics of Solids*, Cambridge University Press, Cambridge, England, (2002).

[148] M. J. Rozenberg, G. Kotliar, H. Kajueter, G. A. Thomas, D. H. Rapkine, J. M. Honig, and P. Metcalf, *Phys. Rev. Lett.* **75**, 105 (1995).

[149] L. Baldassarre, A. Perucchi, D. Nicoletti, A. Toschi, G. Sangiovanni, K. Held, M. Capone, M. Ortolani, L. Malavasi, M. Marsi, P. Metcalf, P. Postorino, and S. Lupi,, *Phys. Rev. B* **77**, 113107 (2008).

[150] A. K. Kleppe and A. P. Jephcoat, *Mineralogical Magazine* **68** 433 (2004).

[151] A. Sacchetti, E. Arcangeletti, A. Perucchi, L. Baldassarre, P. Postorino, S. Lupi, N. Ru, I. R. Fisher, and L. Degiorgi, *Phys. Rev. Lett.*, **98**, 026401 (2007).

[152] F.D. Murnaghan, *Proc. Natl. Acad. Sci. U.S.A.* **30**, 244 (1944).

[153] S. Jiuxun, W. Qiang, C. Lingcang, J. Fuqiang, *J. Phys. Chem. Solids* **66**, 773 (2005).

[154] O. K. Andersen and O. Jepsen, *Phys. Rev. Lett.* **53**, 2571 (1984).

[155] V. I. Anisimov, A. I. Poteryaev, M. A. Korotin, A. O. Anokhin, and G. Kotliar, *J. Phys. Condens. Matter* **9**, 7359 (1997).

[156] A. I. Lichtenstein and M. I. Katsnelson, *Phys. Rev. B* **57**, 6884 (1998).

[157] R. Srivastava, L. L. Chase, *Phys. Rev. Lett.* **27**, 727 (1971).

[158] P. Schilbe, *Phys. B* **316**, 600 (2002).

[159] A. G. Aronov, D. N. Mirlin, I. I. Reshina and F. A. Chudnovski, *Solid State Phys.* **19**, 110 (1977).

[160] A. S. Barker, Jr., H. W. Verleur, H. J. Guggenheim, *Phys. Rev. Lett.* **17**, 1286 (1966).

[161] K. Okazaki, S. Sugai, Y. Muraoka, Z. Hiroi, *Phys. Rev. Lett.* **73**, 165166 (2006).

[162] C. H. Koo, J. S. Lee, M. W. Kim, Y. J. Chang, T. W. Noh, J. H. Jung, B. G. Chae, H.-T. Kim, *cond-mat/0508212*.

[163] *Handbook of Optical Constants of Solids II*, edited by E. D. Palik (Academic, San Diego, 1991).

[164] Y. Zhao, Z. Zhang, Y. Lin, *J. Phys. D* **37**, 3392 (2004).

[165] P. G. Johannsen, G. ReiB, U. Bohle, J. Magiera, R. Mller, H. Spiekermann, W. B. Holzapfel, *Phys. Rev. B* **55**, 6865 (1997).

[166] L. Malavasi, M. Baldini, L. Dubrovinsky, private communication.

[167] Y. Hong-Tao, F. Ke-Cheng, W. Xue-Jin, L. Chao, H. Chen-Jauna, N. Yu-Xin, *Chin. Phys. Soc.* **13**, 82 (2004).

[168] A. Pashkin, M. Dressel, C. A. Kuntscher, *Phys. Rev. B* **74**, 165118 (2006).

[169] C.C. Homes, M. Reedik, D.A. Cradles, and T. Timusk, *Appl. Optics* **32**, 2976 (1993).

Acknowledgements

Over the long process of completing my Ph.D. many people have taught me, helped me, or have otherwise made my graduate student experience richer and fuller. First of all, I would like to thank my advisor, Paolo Postorino, for teaching, supporting, and supervising me during my Ph.D. and for critical revising of the thesis. Especially his ability to transfer his vast knowledge was invaluable for me during these three years. For the same reasons I thank Paolo Dore who was an equally important source of information for me due to his deep physical understanding. I also thank Giovanni Stefani for the interesting, useful and friendly discussions. Then, I would like to express my gratitude to Stefano Lupi, Andrea Perucchi, Leonetta Baldassare, and Matteo Valentini for fruitful measurements carried out together at the SISSI beamline, but also for nice time spent together in Trieste. I am indebted to Daniele di Castro and to Maria Baldini who provide me a friendly guidance at the first step of my work. I reserve a special thank to Emanuele Arcangeletti for the work done during my Laurea thesis, continuing during the first year of my Ph.D.. Thanks are due to the other young researchers of our group: Daniele Chermisi, Sara Mangialardo, and Ilaria Zardo for their precious collaboration. Thanks to Lorenzo Malavasi for provinding me many samples studied in this work. I want to thank people of the IRS group : Paolo Calvani, Alessandro Nucara, Daniele Nicoletti, Chiara Mirri for fruitful collaboration and helpful discussions. Mario Pallagrossi and all the technical equipe at Univ. La Sapienza for having built part of the experimental apparatus, without their job my work would have been more difficult. Finally, but not at least, I gratefully thank my family and in particular my mother, my father and my sister for supporting me all long these years.